2012

# STRUCTURAL BASIS OF SUBSTRATE RECOGNITION IN THIMET OLIGOPEPTIDASE AND DEVELOPMENT OF NANOPARTICLES FOR THERAPEUTIC ENZYME DELIVERY

Jonathan Mark Wagner
*University of Kentucky*, jonw7782@gmail.com

## Recommended Citation

Wagner, Jonathan Mark, "STRUCTURAL BASIS OF SUBSTRATE RECOGNITION IN THIMET OLIGOPEPTIDASE AND DEVELOPMENT OF NANOPARTICLES FOR THERAPEUTIC ENZYME DELIVERY" (2012). *Theses and Dissertations--Molecular and Cellular Biochemistry*. 6.
https://uknowledge.uky.edu/biochem_etds/6

STUDENT AGREEMENT:

I represent that my thesis or dissertation and abstract are my original work. Proper attribution has been given to all outside sources. I understand that I am solely responsible for obtaining any needed copyright permissions. I have obtained and attached hereto needed written permission statements(s) from the owner(s) of each third-party copyrighted matter to be included in my work, allowing electronic distribution (if such use is not permitted by the fair use doctrine).

I hereby grant to The University of Kentucky and its agents the non-exclusive license to archive and make accessible my work in whole or in part in all forms of media, now or hereafter known. I agree that the document mentioned above may be made available immediately for worldwide access unless a preapproved embargo applies.

I retain all other ownership rights to the copyright of my work. I also retain the right to use in future works (such as articles or books) all or part of my work. I understand that I am free to register the copyright to my work.

REVIEW, APPROVAL AND ACCEPTANCE

The document mentioned above has been reviewed and accepted by the student's advisor, on behalf of the advisory committee, and by the Director of Graduate Studies (DGS), on behalf of the program; we verify that this is the final, approved version of the student's dissertation including all changes required by the advisory committee. The undersigned agree to abide by the statements above.

Jonathan Mark Wagner, Student

Dr. David Rodgers, Major Professor

Dr. Michael Mendenhall, Director of Graduate Studies

# STRUCTURAL BASIS OF SUBSTRATE RECOGNITION IN THIMET OLIGOPEPTIDASE AND DEVELOPMENT OF NANOPARTICLES FOR THERAPEUTIC ENZYME DELIVERY

---

DISSERTATION

---

A dissertation submitted in partial fulfillment of the requirements for the degree of Doctor of Philosophy in the College of Medicine at the University of Kentucky

By

Jonathan Wagner

Lexington, Kentucky

Director: Dr. David W. Rodgers

Professor of Molecular and Cellular Biochemistry

Lexington, Kentucky

2012

# ABSTRACT OF DISSERTATION

Neuropeptidases are responsible for degradation of signaling peptides in the central nervous system and periphery. Some neuropeptidases have also been shown to play a role as part of the cell's hydrolytic machinery responsible for breaking down proteins and peptides into amino acids, and these enzymes therefore influence small peptide availability for antigen presentation. A better understanding of how neuropeptidases recognize their substrates could lead to therapeutics that modulate the activity of these important enzymes. Alternatively, re-engineering these enzymes to selectively hydrolyze undesirable peptides could make them attractive as therapeutics themselves. A key question in understanding the activity of these enzymes is how they are able to recognize a variety of seemingly unrelated amino acid sequences as cleavage sites. We are investigating the basis for this general substrate recognition in neuropeptidases using thimet oligopeptidase (TOP) as a model. Crystal structures of TOP in complex with a variety of substrates and inhibitors shed light on the mechanisms underlying substrate recognition and pave the way for re-targeting substrate recognition in these enzymes.

Nano test tube particles have been proposed as a means of delivering therapeutics such as enzymes. However, the template synthesis method for nano test tube production does not produce therapeutic quantities. In order to take full advantage of re-engineered neuropeptidases a new method for nano test tube synthesis has been developed. We show that a non-destructive template synthesis methodology can be applied to produce nano test tube particles in quantities useful for therapeutic enzyme immobilization.

Keywords: Neuropeptidase, substrate recognition, X-ray crystallography, template synthesis, nanofabrication

# STRUCTURAL BASIS OF SUBSTRATE RECOGNITION IN THIMET OLIGOPEPTIDASE AND DEVELOPMENT OF NANOPARTICLES FOR THERAPEUTIC ENZYME DELIVERY

By

Jonathan Wagner

David W. Rodgers

Director of Dissertation

Michael Mendenhall

Director of Graduate Studies

Date 11/13/2012

# Acknowledgements

The work presented here would not have been possible without the support of people around me who dedicated their time for my benefit. First of all, I would like to thank my mentor, Dr. David Rodgers, for teaching me the skills needed for quality research. The idea for this project was originally conceived of by him and I benefitted from excellent guidance from him at every turn along the way. His encouragement and optimism carried me through many disappointments. During my time in David's lab I had daily help from Dr. Jack Schmidt who taught me basic Biochemistry techniques and critical data analysis skills. His friendship went a long way towards making my stay a pleasant one. I have also benefitted from hands-on training and guidance from a number of researchers who were my neighbors in the lab. Dr. Craig Van der Kooi was particularly helpful while I was learning to use crystallography related software. Dr. Brian Wajdyk, Dr. Ji Wu, and others assisted me with the instruments necessary for nanoparticle characterization. Without their help, and without the help of many others this work would have taken much longer, or perhaps become impossible.

I would also like to thank my co-Advisor, Dr. Bruce Hinds, for his help. His ideas led to the discovery of a new method for making nano test tube particles. He was a persistent coach and great motivator who pushed me out of my comfort zone to learn techniques outside the realm of Biochemistry. Besides my advisors, I owe a debt of gratitude to my committee members Dr. Lou Hersh, Dr. Luke Bradley, and Dr. Brian Stevenson for their assistance. They accommodated me during organization of my

committee meetings and provided perspectives that kept me on the right track during the evolution of this project and during the writing of my dissertation.

Finally, I would like to thank my family and friends for their support during my graduate work. Certainly no one has sacrificed more for it than they have. There are too many people to mention them all, but the greatest contributors were my parents and my wife. My Mom and Dad valued education and always encouraged me to pursue excellence in my schoolwork. Their personal attention and financial support gave me the momentum needed to reach this point. Also my beautiful wife, Heidi, gave up her job and her personal ties in Tennessee to allow me to pursue my graduate studies. Without her continual support and sacrifice, this project would certainly have been cut short. She has been a steadfast source of encouragement for me during this work and I am very grateful.

## Table of Contents

# List of Tables

## List of Figures

# CHAPTER ONE: Introduction

## How neuropeptidases effect cell signaling

One of the most common signaling molecules used by cells to communicate are small peptides. In eukaryotes, these peptides are initially produced in a highly regulated fashion as preprohormones and subsequently processed by endolytic enzymes into their smaller, active forms [1]. The paracrine, autocrine, or endocrine peptide signal is communicated by release of the peptides into the extracellular region where it can be carried to specific cell surface receptors (Figure 1.1). Termination of the peptide signal is brought about by hydrolytic peptidases in the extracellular matrix or cytosol. The duration of a given peptide signal is therefore dependent, in part, on how quickly it is degraded after release. The peptidases responsible for biopeptide metabolism have been the target of extensive research in academia as well as the pharmaceuticals industry and there are a number of examples of peptidase targeted drugs [2, 3].

Bioactive peptides are often termed neuropeptides, and the hydrolytic enzymes that metabolize them are called neuropeptidases. One of the largest classes of neuropeptidases are the soluble metalloendopeptidases [1]. Of these angiotensin converting enzyme (ACE) is probably the most well known since its inhibition lowers blood pressure and prevents heart attack [4, 5]. Two other metalloendopeptidases closely related to ACE, thimet oligopeptidase (TOP) and neurolysin, have also been studied extensively for their roles in many physiological processes. These two enzymes have been implicated in nociception [6-9], blood pressure regulation [10-13], the immune system [14-16], reproduction[1, 17], tumorigenisis [18], and plaques associated with

Alzheimer’s disease [19]. In an effort to control these two enzymes, relatively selective competitive inhibitors have been developed [20-22], but they are not currently the targets of any disease therapy.

## Roles of thimet oligopeptidase and neurolysin.

TOP and neurolysin are 63% identical in primary sequence and share very similar folds [23]. These two similar enzymes were first isolated from brain tissue based on their ability to hydrolyze the important neurotransmitter neurotensin [8, 24]. Later they were differentiated by their differing neurotensin cleavage sites [25]. The difference in neurotensin cleavage site can be attributed to just two sequence changes at residues located in the large central channel that runs the length of the enzyme, which also contains the active site [23]. Specific TOP and neurolysin inhibitors were shown to prevent bradykinin hydrolysis resulting in lower blood pressure and increased vascular permeability [11, 13, 26]. Similarly, inhibitor studies showed a potentiation of opioid mediated anti-nociception indicating involvement of TOP and/or neurolysin in degradation of opioid peptides such as adrenorphin, dynorphin A, and dynorphin B [7]. Degradation of the important reproductive hormone luteinizing hormone releasing hormone (LHRH) by TOP coupled with prolyl oligopeptidase [17, 27-29] was also demonstrated *in vitro* and *in vivo* using inhibitors. Degradation of signaling peptides by TOP and neurolysin often have the effect of inactivating them, however, many products of degradation have physiological effects of their own. Liberation of enkephalins from dynorphin A(1-8) and adrenorphin [30] and LHRH 1-5 from LHRH [27], for example. The important roles played by TOP and neurolysin in controlling the levels of bioactive peptides has made inhibitor development targeting these enzymes an area of active research [31-33].

## Roles for TOP and neurolysin in the immune system

The proteasome constantly recycles proteins in the cytosol of the cell by hydrolyzing them into peptide fragments. This population of fragments containing largely oligopeptides 4-24 residues long with basic, hydrophobic, and acidic amino acids at their C-termini [34] is the pool from which, ultimately, TAP and MHC I are loaded with antigenic epitopes for presentation to scanning immune cells at the cell surface [35]. MHC I epitopes taken from proteasomal products are trimmed at the N-termini by cytosolic peptidases, but usually retain their original C-termini residues up to the point where they are presented by MHC I (Figure 1.2).

One of the best studied examples of broad peptide recognition comes from the MHC class I and class II proteins of the immune system, which present processed peptides to T cell receptors on the surfaces of lymphocytes to activate immune responses [36]. Interestingly, some aspects of the broad recognition mechanism found in TOP are also used by the MHC molecules. In both types of MHC molecules, peptides bind in narrow clefts defined by two parallel but somewhat separated helices. MHC class I molecules achieve broad peptide binding by interacting primarily with the N and C termini of bound ligands as they associate with the binding groove [37, 38]. As noted, TOP makes extensive interactions with the C-termini of bound peptides, and like MHC I, basic and aromatic residues are involved in the interactions. The binding sites of both types of MHC molecules are rich in aromatic residues, like the TOP binding surface. Like peptides on the TOP binding surface, peptides bound to MHC I follow variable paths in interacting with the surfaces of the groove walls [39], although the degree of contact between the peptides and either wall surface are not as extensive as the interaction with the binding surface in TOP. MHC II molecules interact with a broad range of peptides by making a number of hydrogen bonds to groups on the peptide backbone, again reminiscent of the backbone hydrogen bonds made to the TOP binding surface [36, 40]. In contrast to TOP, though, peptides binding to MHC II uniformly adopt a polyproline II type helical backbone conformation, having the effect of precisely placing backbone groups in position for hydrogen bond interactions with the protein [40]. The relatively flat surface in TOP allows considerably more variability in the backbone conformations of bound peptides. The interaction with the binding groove of MHC does bury more of the accessible peptide surface than binding to the flat surface of TOP [41]. Furthermore, groove closure appears to reduce the off rate of the peptide from MHC by physically entrapping it [42]. Overall, these led to more extensive interactions with the peptides, consistent with the much higher affinity shown by the MHC molecules. This high affinity would not be desirable in TOP, which must release product peptides to turn over catalytically.

## Broad substrate selection by TOP and neurolysin

TOP and neurolysin are active only on relatively short peptide substrates. The longest reported substrate is 17 residues in length [43]. They generally hydrolyze bioactive peptides preferentially at only one or two peptide bonds, and they cleave at sites with significant sequence variations (Figure 1.3). The only generalization that can be made is that TOP substrates tend to be somewhat enriched in hydrophobic, aromatic, and basic residues, but these can occur at different positions relative to the cleaved bond.

This trend also reflects a bias in the residue composition of bioactive peptides, and may therefore not be of particular significance in TOP substrate recognition. Some studies have characterized TOP specificity through degradation kinetics of various sequences [43-45], however, no definitive structural evidence is available to show the extent of the TOP binding surface or the type of interactions that produce its fuzzy specificity. TOP's ability to hydrolyze specific bonds inside substrates with no apparent sequence similarity – an attribute which is shared by most other neuropeptidases allows it to be used to metabolize different bioactive peptides in different cell types and different subcellular locations. The structural basis for this "fuzzy" substrate recognition is an important question in molecular recognition and is of fundamental importance to predicting or manipulating TOP specificity.

## Previous insights from thimet oligopeptidase structures

TOP and neurolysin are members of the thermolysin-like zinc metallopeptidase family that contain the active site amino acid sequence motif HEXXH [46]. The sequence forms part of a helical element, and the two histidines can coordinate a zinc ion cofactor with the help of a downstream glutamate. The glutamate in the sequence motif orients and activates a water molecule for nucleophilic attack on the carbon of peptide main chain carbonyl groups to affect hydrolysis of the peptide bond. The zinc ion cofactor promotes deprotonation of the attacking water group and stabilizes charge development on the carbonyl oxygen in the transition state. Studies using inhibitors to model substrate binding indicate that polypeptide substrates interact with the edge strand of a beta sheet located at the active site, forming main chain hydrogen bonds to effectively extend the sheet by an additional, anti-parallel strand [47]. The HEXXH motif was first characterized structurally in the bacterial protease thermolysin [48], where the helix is located near the center of a slightly concave surface of the enzyme. Initial X-ray structures of much larger TOP and neurolysin [49, 50] revealed that these enzymes have a much deeper channel running the length of the molecule, with the active site located near the base of one channel wall. The overall fold then is clam-shell shaped (Figure 1.5). With this architecture, only peptides in an extended conformation can diffuse into the central channel and gain access to the active site machinery, explaining the lack of activity on larger peptides and proteins.

Other metalloendopeptidases including dipeptidyl carboxypeptidase (DCP) [51] and angiotensin converting enzyme 2 (ACE2) [52] have been solved in the closed ligand-bound form as well as the open, unliganded form (Figure 1.6). The structure of DCP provides a particularly close analogy to what closed, substrate-bound, TOP might look like. This structure was solved in complex with two dipeptide fragments interacting with DCP near the active site. One fragment binds forming anti parallel beta sheet-like interactions next to the active site with additional interactions being donated from the opposite side of the cleft. Another fragment binds at a different angle that carries it away from the active site to interact with the second domain. Based on DCP we would expect TOP to undergo a similar hinge-like bending motion that narrows the central channel. This conformational change would likely be stabilized by the presence of a bound peptide interacting with both channel walls.

In the closed form of DCP, the central channel is too narrow to allow peptide diffusion into the active site, and the initial interaction of substrate peptides must be with the open form of the enzyme. It is not clear how these initial interactions occur. Work presented in this dissertation describes and characterizes an initial substrate binding surface present in TOP. The results also define a mechanistic basis for the broad substrate recognition shown by TOP and a number of other neuropeptidases. Ultimately, this work should allow for rational alteration of the substrate binding specificity of TOP, neurolysin, and similar oligopeptidases. And put together with thermodynamic and biochemical experiments these structures contribute to our understanding of protein-peptide interactions as a whole.

## Neuropeptidases as therapeutics

Most current therapeutics are small molecules that target macromolecules in the body. A promising, but considerably less developed, alternative is to use macromolecules themselves as therapeutics. Macromolecules have the potential for complex effects that can never be mimicked by small molecule drugs [53, 54]. Indeed, one of the fastest growing category of FDA approved drugs are biological polymers [55]. Enzymes in particular have a bright future since they can catalyze desired biological reactions over an extended period. Moreover, modern molecular biology provides the means for large scale recombinant enzyme production and even control over enzyme specificity using mutagenesis.

Especially notable success using enzymes has already been achieved for diseases caused by the complete lack of an enzyme, such as lysosomal storage diseases, where enzyme replacement therapy is the standard of care [53, 56-58]. However, these enzyme therapies are expensive, require frequent dosing, and suffer from immune reactions [59, 60]. New strategies for delivering enzymes are needed in order for these therapies to reach their full potential.

Oligoendopeptidases such as TOP are attractive enzyme therapeutics because they can degrade numerous undesirable bioactive peptides such as beta amyloid and angiotensins. Also, since they do not hydrolyze proteins, oligoendopeptidases are safer to use in the body relative to proteases. Therefore, recombinant TOP with re-engineered specificity for only undesirable peptides instead of its natural, broad, specificity could be used as a therapeutic. The principle of neuropeptidases as therapeutics has been demonstrated by expressing another neuropeptidase, neprilysin, peripherally in mouse models of Alzheimer's disease [61, 62]. These treatments proved the concept of using neuropeptidases as therapeutics, however, they required the use of gene therapy - an approach with many disadvantages [63]. If similar levels of sustained peptidase activity could be achieved in vivo by simply injecting recombinant protein it would provide an attractive alternative.

## Nanoparticles for enzyme delivery.

Using molecular biology to retarget enzyme therapeutics is only one technique for improving efficacy. Yet another major factor preventing the realization of enzyme therapy's full potential is that the harsh environment of the body quickly inactivates most recombinant enzyme therapeutics [53, 64]. Consequently there has been great interest in vehicles for enzyme delivery that might allow therapeutic enzymes to function in a better environment. Many groups have demonstrated the benefits of enzyme immobilization in or on nanoparticles [65-72]. Not only do nanoparticles allow stabilization of immobilized enzymes, but they also allow targeting of enzyme therapeutics to specific organs or tissues [73-76]. Enzyme immobilization on nanoparticles is a promising route to improve efficacy of current enzyme replacement therapies [64, 68, 77] or to extend the range of diseases that could feasibly be treated by enzyme therapy to include diseases such as cancer [78, 79], and Mitochondrial Neurogastrointestinal Encephalomyopathy (MNGIE) [64].

Most enzyme immobilization in nanoparticles has been done by attaching enzymes to the outside surface of solid, spherical, particles composed of a metal or polymer. This is because spherical particles are the simplest to synthesize, however, elongated or tube shaped particles provide distinct advantages such as longer circulation time and larger payloads [80-82]. Furthermore, hollow particles that encapsulate enzymes within to create a "bioreactor" provide more protection from proteolytic degradation and immune system recognition [64, 68]. We envisioned a hollow, tube shaped, bioreactor that would safeguard enzymes inside while allowing free diffusion of substrates and products. In addition to enzyme immobilization on the inside surface these tubes could be decorated with passivating or targeting functionalities on the outside.

Many different core-shell compositions are possible for template synthesized tubes including a wide variety of metals and biodegradable polymers [83-85]. Although template synthesis allows considerable control over nano tube parameters, current methods are limited in scale up for high volume manufacturing. Porous alumina templates of suitably uniform pore size and appropriate length are not commercially available. Synthesizing the templates is laborious and includes depositing thick layers of metal followed by long anodization in acid [86]. Once the desired materials are infiltrated, the alumina template is dissolved with strong etchants [84, 87], which are incompatible with many desired tube materials. Destroying the template means re-making a new template for every round of production. The template synthesis method is essentially a 2-dimensional synthesis, requiring large amounts of surface area (~20 $m^2$) to produce commercial quantities. Therefore, the resources and labor that would be required to manufacture therapeutic quantities of nano test tubes is prohibitive.

## Studies presented in this thesis.

In this work we set out to use structural and biophysical techniques to define the mechanism of fuzzy substrate recognition in thimet oligopeptidase (TOP). This ability to recognize many different peptide sequences while retaining a degree of specificity is central to the function of this important class of enzymes. It is also a fundamental question in molecular recognition between biological molecules and bears upon the general problems of ligand and protein-protein recognition. In a more practical sense, we anticipate that understanding substrate recognition in these enzymes will enable the re-engineering of TOP and similar neuropeptidases to modulate their degree of specificity, making them more suitable as therapeutics. Similarly, understanding TOP substrate recognition may aid in the design of competitive TOP inhibitors. Using X-ray crystallography we have succeeded in characterizing the interactions formed by a diverse set of peptide substrates upon initial binding to TOP. These structures, coupled with biochemical and biophysical experiments, shed new light on the set of interactions available to TOP and reveal the extent of the TOP binding site.

Studies are also presented aimed at developing an approach for nanoparticle fabrication and enzyme immobilization that may allow TOP and other enzymes to be used in the clinic. This work will advance the current field of enzyme therapeutics and provide the underpinnings for a new class of nanoparticle therapeutics. By introducing a new technique for non-destructive template replication [88, 89] to quickly and easily synthesize test tube shaped nanoparticles, we show that it is possible to scale up production to the level needed for industrial or therapeutic enzyme delivery. In this new approach, the pores of a hard template are used to produce pillar like structures in a polymer material, which can subsequently be coated to make the nano tubes without alteration of the original template.

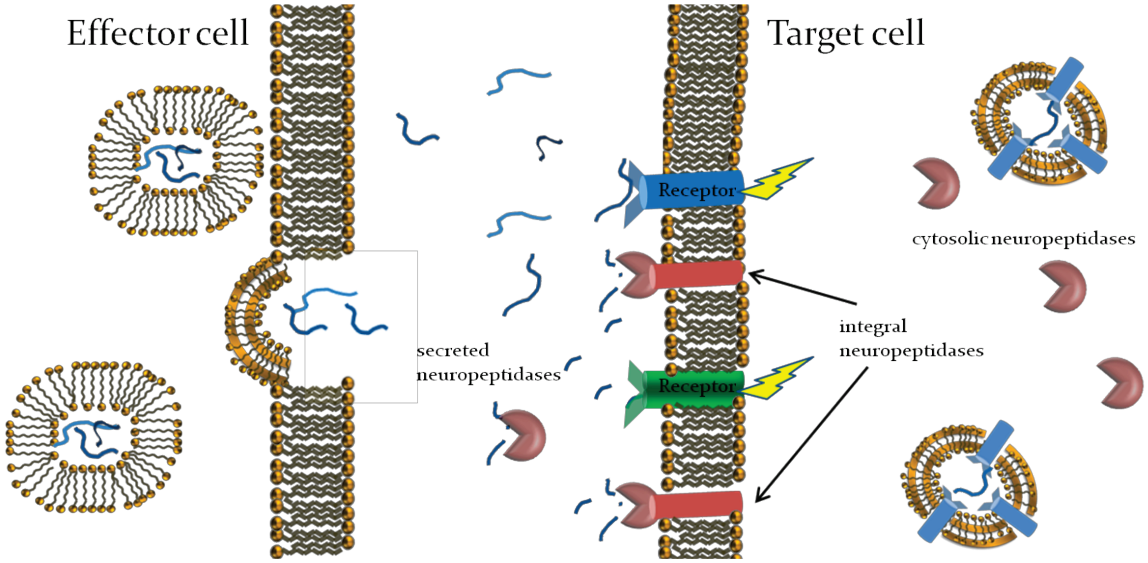

**Figure 1.1 Neuropeptide signaling.** Neuropeptidases hydrolyze signaling peptides at the cell membrane or within the cell. In this way they can reduce the duration of a signal or trim peptides into smaller pieces with new signaling effects.

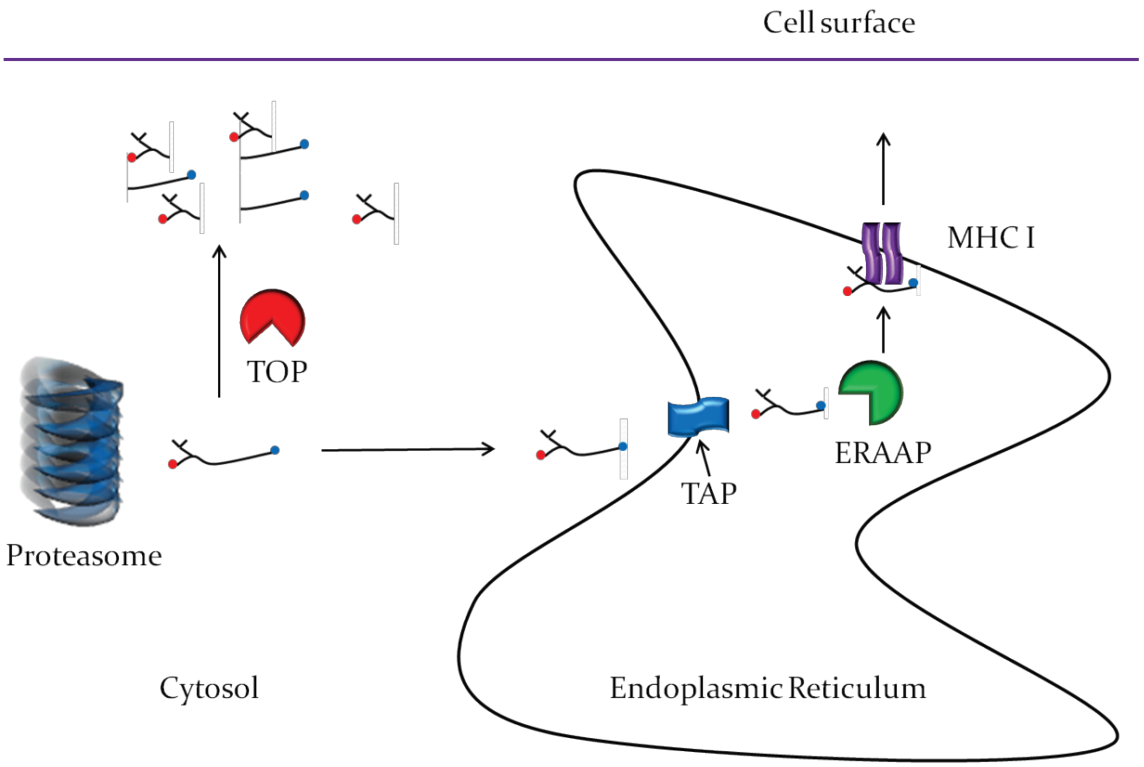

**Figure 1.2 Antigen processing.** TOP degrades small cytosolic peptides that otherwise might be selected for presentation on major histocompatibility complex I (MHC I).

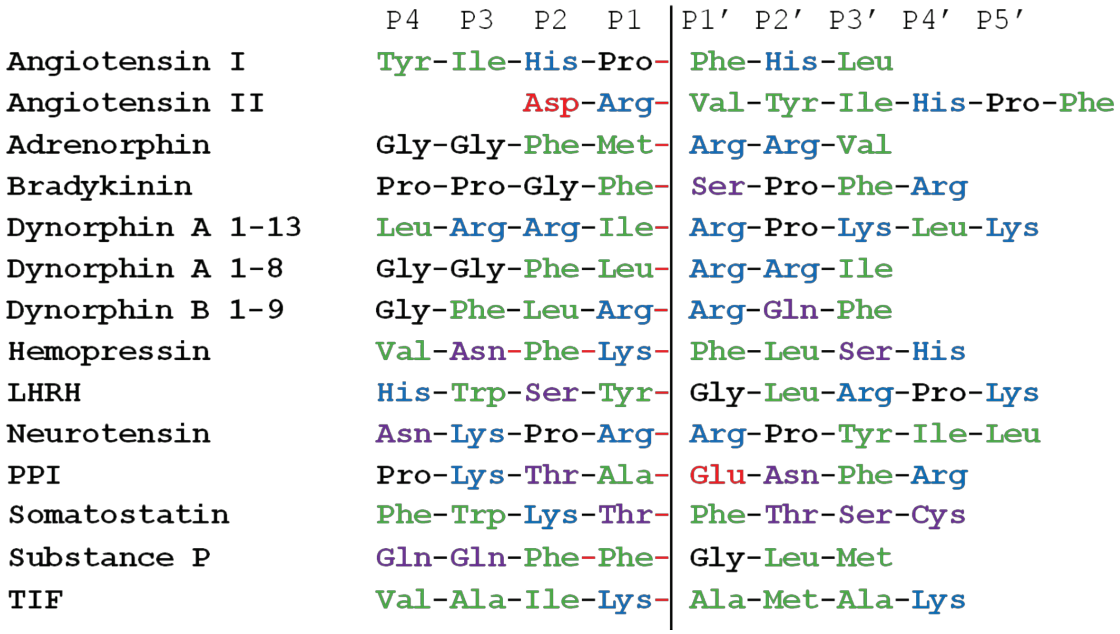

| | P4 P3 P2 P1 | P1′ P2′ P3′ P4′ P5′ |
|---|---|---|
| Angiotensin I | Tyr-Ile-His-Pro- | Phe-His-Leu |
| Angiotensin II | Asp-Arg- | Val-Tyr-Ile-His-Pro-Phe |
| Adrenorphin | Gly-Gly-Phe-Met- | Arg-Arg-Val |
| Bradykinin | Pro-Pro-Gly-Phe- | Ser-Pro-Phe-Arg |
| Dynorphin A 1-13 | Leu-Arg-Arg-Ile- | Arg-Pro-Lys-Leu-Lys |
| Dynorphin A 1-8 | Gly-Gly-Phe-Leu- | Arg-Arg-Ile |
| Dynorphin B 1-9 | Gly-Phe-Leu-Arg- | Arg-Gln-Phe |
| Hemopressin | Val-Asn-Phe-Lys- | Phe-Leu-Ser-His |
| LHRH | His-Trp-Ser-Tyr- | Gly-Leu-Arg-Pro-Lys |
| Neurotensin | Asn-Lys-Pro-Arg- | Arg-Pro-Tyr-Ile-Leu |
| PPI | Pro-Lys-Thr-Ala- | Glu-Asn-Phe-Arg |
| Somatostatin | Phe-Trp-Lys-Thr- | Phe-Thr-Ser-Cys |
| Substance P | Gln-Gln-Phe-Phe- | Gly-Leu-Met |
| TIF | Val-Ala-Ile-Lys- | Ala-Met-Ala-Lys |

**Figure 1.3 Preferred TOP cleavage sites.** TOP hydrolyzes substrates with a wide variety of amino acids near the cleaved bond.

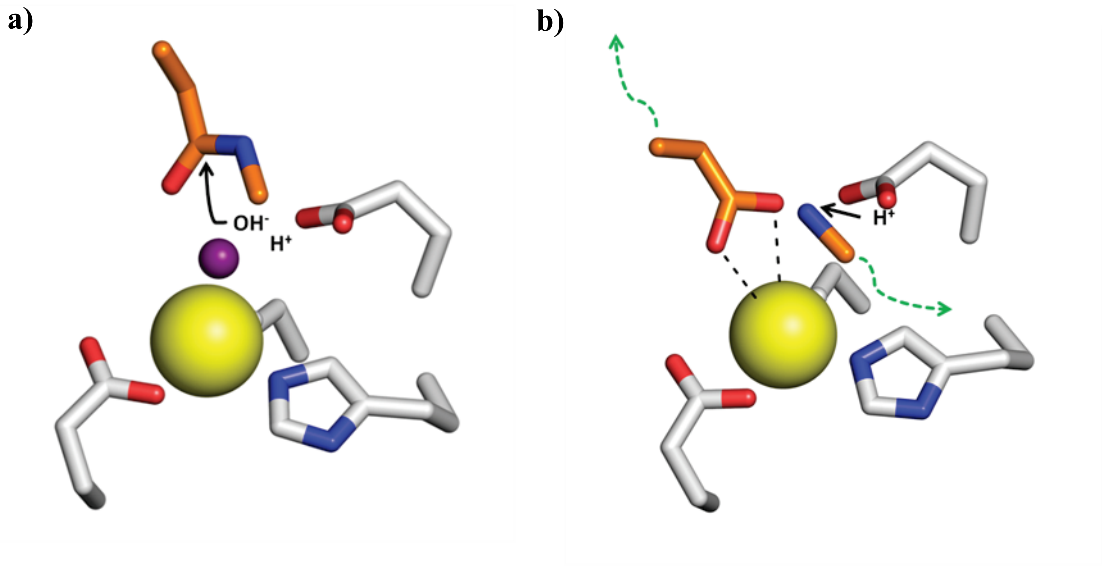

**Figure 1.4 Mechanism of hydrolysis.** Relevant TOP residues are shown as white sticks. A generic peptide bond is shown in orange sticks. **a)** The catalytic water molecule (purple sphere) coordinates zinc (yellow sphere) and is oriented / activated for nucleophilic attack by a nearby glutamate (E474). E474 accepts a proton from the water during formation of the transition state. **b)** The newly formed C-terminus coordinates zinc and E474 now donates a proton to the newly formed N-terminus. Green arrows indicate that fragments are now free to diffuse away.

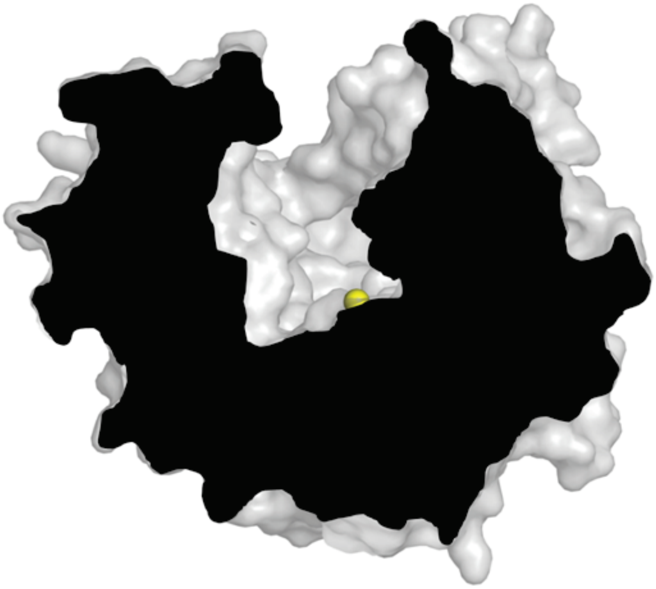

**Figure 1.5 Clam shell shape of TOP.** Unliganded TOP structure cutaway at the level of the active site. The active site coordinates a zinc ion (yellow sphere) near the bottom of a large interdomain cleft that limits substrate access. TOP and neurolysin both share this fold.

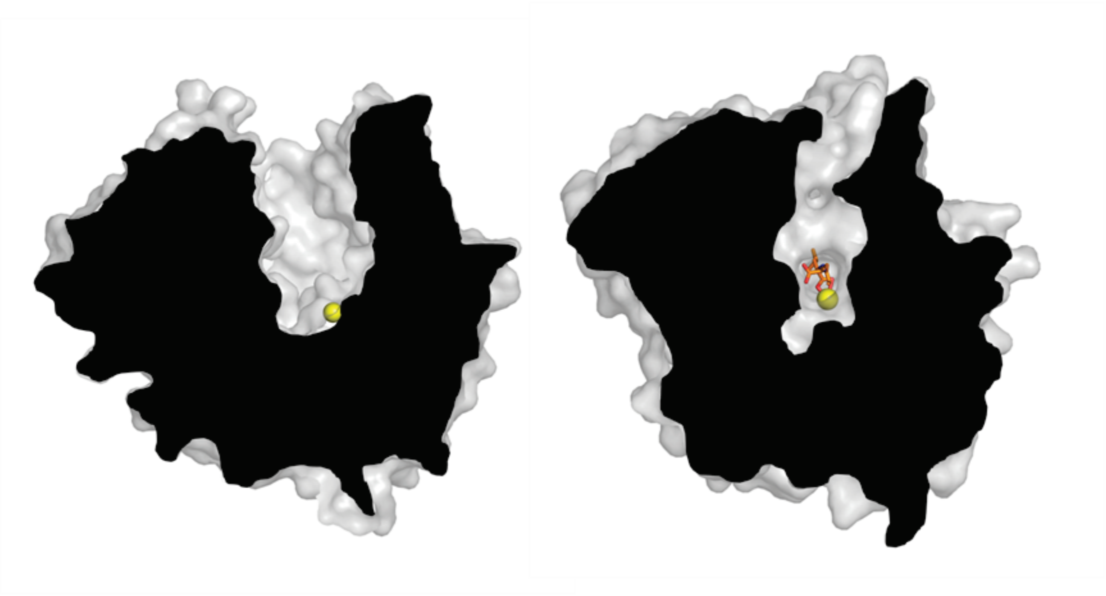

**Figure 1.6 Substrate induced closure of ACE2. a)** ACE2 unliganded structure cutaway at the level of the active site. Zinc ion is shown as a yellow sphere **b)** ACE2 after binding ligand (lisinopril) undergoes a significant closing motion.

# CHAPTER TWO: Materials and Methods

## Thimet oligopeptidase

### Expression / purification of N truncated TOP

A TOP overexpession construct (residues 16-689) in the pET32a vector previously made in the lab [49] was used to produce the enzyme in *E. coli*. In this construct, three cysteine residues are mutated to serine (C253S, C246S, C427S) to prevent covalent aggregation, and the catalytic glutamate residue is mutated (E474A) to greatly reduce activity. Overexpression was carried out as previously described [49], with the exceptions that TB media was substituted for LB media and cultures were grown to an $OD_{600}$ of 2.5 prior to being induced with 1 mM IPTG. *E. Coli* were harvested four hours after induction, resuspended in 50 mM $NaH_2PO_4$ pH 8.0 with 1 mM BME and 20% glycerol, then frozen for later use.

TOP was purified by Ni affinity chromatography making use of the N-terminal polyhistidine fusion sequence in the expressed construct as previously described [49]. Removal of the polyhistidine sequence by enterokinase cleavage was used to elute the enzyme from the affinity resin. TOP preparations typically yielded 25 mg protein per liter. This protein was further purified by anion exchange chromatography using HQ Poros (Pharmacia) or Hyper D (Acrosep) strong anion exchange resins in an Akta FPLC system. Conditions during anion exchange were 20 mM Tris pH 8.5, 10 mM NaCl, 2 mM BME (binding) or with 1 M NaCl added (elution). TOP was eluted from the columns using a gradient of 15 column volumes going to a final 15% elution buffer concentration. This produced two closely associated protein peaks, mass spectrometry revealed that the first peak was slightly lighter than the expected 77,906.5 Da molecular weight and the second was slightly heavier (peak 1 = 77,900 Da and peak 2 = 77,924 Da). Both peaks were similarly active in quenched fluorescent peptide degradation assays, but excluding peak two fractions allowed crystals to be produced more consistently. The second peak was therefore usually discarded. After elimination of peak 2 final yields were typically 15 mg of TOP per liter.

### Mutation and expression/purification of dual truncated TOP

N- and C-terminally truncated TOP constructs were made by using Quikchange mutagenesis to change either Gly680 or Glu684 of N-terminally truncated TOP to a stop codon. The same primers were used to add stop codons at the same position to the Glu474A inactive as well as the Glu474 active version of TOP (Figure 2.1). The four resulting sequences were confirmed by DNA sequencing.

Dual-truncated TOP was successfully expressed and purified using the same protocol as with purification of N truncated TOP. Tryptic digest mass spectrometry was used to sequence dual truncated TOP and confirmed the expected serine 16 through valine 679 TOP sequence plus a cloning artifact comprising six additional amino acids (MADIGS) left on the N terminal after enterokinase digestion. The total molecular weight of N15_C10_E474A _C246S_C253S_C427S TOP was 76,906.4 Da according to trypsin digest mass spectrometry (Figure 2.2), and this agreed perfectly with the calculated mass.

## Activity of dual truncated TOP

The activity of dual truncated TOP ending with Val679 was compared to that of N-truncated TOP ending in Cys689. Reaction buffer was 50 mM HEPES pH 7.2, 100 mM NaCl, and 1 mM BME in a final reaction volume of 3 ml. Quenched fluorescent neurotensin (Abz-NT-edd) [90] was added to a final concentration of 30 μM. Then TOP was added to a final concentration of 10 nM and fluorescent readings taken starting immediately. Activity was measured in a 1 cm disposable cuvette using a Perkin Elmer LS 55 Luminescence Spectrometer with the following settings: stir = on, photomultiplier = std @ setting 775, 2.5 nm slits, excitation = 319 nm, emission = 419 nm, temperature = 37 $^{o}$C.

## Crystallization of N truncated TOP

N truncated TOP was crystallized as reported before [49]. Briefly, 1 μl of TOP concentrated to 8-15 mg/ml in 20 mM Tris buffer pH 8.5, 10 mM NaCl, 2 mM BME, was mixed with 1 μl well solution and crystallized by hanging drop vapor diffusion at room temperature. Well conditions were 0.1 M sodium cocadylate pH 6.5, 55 mM magnesium acetate, 11-13% PEG 6000. Crystals grew to maturity in less than a day, sometimes even becoming visible within 30 minutes (Figure 2.3). N-truncated TOP crystals were stable in solution even without precipitates, however, some crystals were unstable if harvested less than a day after crystallization.

## Crystallization of dual truncated TOP

Dual-truncated TOP altered either at Gly680 or Glu684 no longer crystallized in the conditions used for N-truncated TOP. So, for crystallization the truncated TOP construct ending at Val679 was transferred to a new buffer made up of 10 mM Tris pH 8.5, 10 mM NaCl, and 2 mM BME. Final concentration for crystallization was 3.0 - 5.0 mg/ml TOP. JCSG (Qiagen) suite crystallization screens (core suites I, II, III, IV) and subsequent condition optimization screens were set up in 96-well plates using a Mosquito automated crystallization robot (TTP Lab Tech) and the hanging drop vapor diffusion method. Final optimized conditions were set up by hand in Greiner 24 well hanging drop plates. Optimal well conditions were 100 mM CHES pH 8.3, 400 mM $MgCl_2$, 12-15% PEG 6000 and drops contained 3 uL protein solution to 1 uL well solution ratio. Plates were incubated at 12$^o$C and long, board-like, crystals formed over 1-2 days (Figure 2.3b).

A second condition also yielded dual-truncated TOP crystals that diffracted to below 2 Angstroms. These crystals were grown from protein concentrated to ~6 mg/ml in the same 10 mM Tris pH 8.5, 10 mM NaCl, 2 mM BME buffer, but the well solution was 100 mM Tris pH 9.8, 450 mM $MgCl_2$, 14-19% PEG 6000. Drops contained 1 uL protein and 1 uL well solution. These crystals were of a similar morphology and space group and yielded identical structures as in 100 mM CHES based conditions. However, crystals grown from CHES conditions were preferred because of the more physiological pH and because CHES does not react with glutaraldehyde thus allowing crystals to be crosslinked in their mother liquor.

## Crystal soaking for complex formation

N-truncated TOP crystals were transferred to ligand solutions without any pre-treatment. Dual-truncated TOP crystals dissolved in dilute solutions. Therefore they were stabilized using glutaraldehyde prior to ligand soaking. Glutaraldehyde (25% from

Sigma) was diluted to 0.1% in crystallization well solution. Crystals were removed from their mother liquor and held under the surface of a droplet of the 0.1% glutaraldehyde solution for 5-10 seconds. (Glutaraldehyde in various polymeric sizes reacts with lysines by forming a Schiff base [91] and has been used before for stabilization of fragile crystals for cryocrystallography [92].) Our aim was to crosslink crystals as lightly as possible to prevent protein diffusion out of the crystal when precipitates were removed from the surrounding solution.

After crosslinking crystals were rinsed by looping them and moving them sequentially through 3, 3 μL, drops of buffer. Buffer conditions were 50 mM HEPES pH 7.5 with 100 mM NaCl. After washing, the crystals were transferred to a 3 uL drop of buffer containing 1-10 mM ligand for 1-10 minutes. It proved important to check the pH of ligand solutions by dropping 0.5 μL onto pH paper. In many cases pH had to be adjusted due to acidity of the ligand associated material overwhelming the buffer. After soaking in the peptide solution, the crystals were briefly dunked in buffer containing 25% glycerol then cryogenically frozen in liquid nitrogen [93].

### TOP activity control

As a control for residual TOP activity acting on bound peptide ligands, N-truncated TOP crystals were subjected to ≥12 hour soaks in peptide soak buffer with 1 mM EDTA. This was followed by normal soaking in ligand solutions, which also had 1 mM EDTA added.

## Data collection and processing

Datasets were collected remotely at Argonne National Lab's Advanced Photon Source (APS) SER-CAT beamlines 22 ID or 22 BM. Data were reduced using the software suite HKL2000 [94]. Phases for dual-truncated TOP were found by molecular replacement with N-truncated TOP using the program Phaser [95, 96]. Subsequent rounds of refinement were carried out using PHENIX [97]. Ligand densities were initially modeled in COOT [98] using the Fo-Fc maps generated by PHENIX after one round of rigid body replacement with the structure of unliganded TOP. Figures were made using Pymol (Delano Scientific).

## Isothermal titration calorimetry

Isothermal titration calorimetry was done using a VP-ITC (Microcal LLC.) instrument. Protein concentration was adjusted such that $10 < c < 100$ where $c = \frac{\text{[thimet oligopeptidase]}}{\text{expected association constant}}$ according to the recommendations of [99, 100] for experiments in which K, H, and S are determined. An exception was made for neurotensin because it would have required more than 15 mg/ml concentration to satisfy this, and in this case c = ~7. The concentration of peptide ligand was adjusted so that the final mole ratio of substrate to enzyme was in the range of 1.2 – 2.0. Thimet oligopeptidase stock was concentrated by ultrafiltration immediately prior to ITC runs, with the concentration estimated from the absorbance at 280 nm (Nanodrop VD 1000 spectrometer; Thermo Scientific). Ligand concentration was also determined using the Nanodrop when ligands contained a tyrosine. All extinction coefficients were calculated using the online ProtParam tool [101]. Ligand solutions for injection were diluted from ~100 fold concentrated stocks with the flowthrough from protein concentration by ultrafiltration. Using the flowthrough from ultrafiltration minimized extraneous signal in the ITC resulting from any differences in buffer composition between the ligand and protein solutions.

Data analysis was carried out using Origin 7.0 software (Microcal). Peaks were initially integrated then all curves were fit using the one site non-linear least squares regression function. Control runs titrating ligand into buffer without enzyme were subtracted from the calculated heats of binding prior to curve fitting. Even after subtracting heats of dilution most runs approached 0.1 - 0.5 kcal/mol in their final injections rather than zero, so a constant was subtracted from all injections such that the final 6-7 heats of injection approached zero.

## Identification of cleavage sites for angiotensin II and dynorphin B(1-9)

Angiotensin II (American Peptide Inc.) or dynorphin B(1-9) (Anaspec Inc.) were dissolved to a final concentration of 150 μM in reaction buffer of 50 mM HEPES pH 7.5, 100 mM NaCl. Purified N15_C2S_TOP also in reaction buffer at a final concentration of 0.075 μM was incubated with angiotensin II or dynorphin B(1-9) at 37°C for one hour. At the end of incubation the reaction was stopped by adding formic acid to a final concentration of 0.25%. Reaction mixtures were then subjected to HPLC analysis (C18 column) and MALDI-TOF analysis at the University of Kentucky, Center for Structural Biology Protein Core Facility (Figure 3.4).

## Nano test tubes

### Porous aluminum oxide template

*50 and 100 nm diameter pore size templates*

To avoid the fragility of commercial templates manufactured using a standard two-step anodization method [102], anodic aluminum oxide template (AAO) was prepared in-house by treating Al film with a one-step anodization procedure. The depth of the pores and thus the length of the nano test tubes produced using the template was controlled by the thickness of aluminum deposition prior to anodization. Aluminum for 50 nm pore size AAO was deposited to the desired depth (0.125, 0.25, 0.5 or 1 μM) on a silicon wafer about 2 $cm^2$ using electron beam evaporation (Torr International, Inc. model EB-4P-6kW). The silicon wafer with aluminum was subsequently anodized at 40 V in 0.3 M oxalic acid at $20^{o}C$ for 2 min. Finally, the pores were allowed to widen in 5% phosphoric acid for 40 min.

100 nm AAO template was made in a similar fashion to 50 nm template. Briefly, 1 μm aluminum on a 6 $cm^2$ silicon wafer was anodized at 120 V in 5% phosphoric acid at $4^{o}C$, for 90 min. Template pores were then widened by soaking templates for 40 min in 5% phosphoric acid.

*200 nm pore size templates*

Porous aluminum oxide with 200 nm pore diameters was also used as a template to make nano test tubes, but in this case commercially available AAO templates, or Anodiscs, (Whatman part #6809-6022) were used. The Anodiscs were placed on a 1 mm thick glass support and mounted on a spin coater (Chemat Technology model KW-4A).

Then epoxy was mixed (Buehler Epoxicure heat curing epoxy) using 1 g epoxy, 0.2 g hardener, and 0.2 g acetone (to thin the mixture). The epoxy was applied over the surface of the aluminum filter and allowed to soak in for 1 min before starting the spin coater. The samples were spun for 1 min at 3000 rpm to spin off excess epoxy. Epoxy was allowed to cure overnight then excess epoxy was removed further using a Buehler Eco-met polisher with 1 µM alumina polishing grit applied. The aluminum filters were transparent after soaking up epoxy and reflective after final polishing. The epoxy was then oxidatively etched to the desired depth of 0.25 - 1 µm using plasma generated in a Plasma Enhanced Chemical Vapor Deposition system (Tek Vac Industries model PE-CVD 60-R). The etch rate was approximately 250 nm/min. with settings $R_f = 150$ W, pressure = 0.7 Torr, air flow rate = 20.0. Etching time was 1, 2, and 4 min. to produce 250 nm, 500 nm and 1 µm pillars, respectively.

## Non-destructive replication

Replication was carried out following the manufacturer's (Ted Pella) replicating tape protocol, briefly: The surface of the AAO was wetted with acetone using a cotton swab (Figure 2.4). Then replicating tape (0.22 µm thick, Ted Pella catalog #44840), a cellulose acetate film, was allowed to contact the wet surface with minimal pressure. The acetone was allowed to dry for 30 sec after which time the sample was completely dry. Then the replicating tape was peeled off the hard template (Figure 2.5). Cellulose acetate shrinks slightly upon solvent evaporation allowing easy release of the polymer from AAO template. Templates could be recycled more than 100 times without any significant effect on nano test tube size or quality. Polymer pillars with heights ranging from 125 nm - 1 μm were replicated successfully from AAO with pore diameters of 200 nm, 100 nm, and 50 nm.

## Metal deposition

Once imprinted with a carpet of pillars complementary to the pores of the AAO template, nano test tubes were fabricated by sputter coating the replication tape with one or more thin layers of metal (silicon, aluminum, titanium, and/or gold). Wetting of the polymer during replication caused the cellulose acetate replication tape to curl. Therefore, it was necessary to affix the tape corners to a solid support with double sided carbon tape during metal deposition (Figure 2.5). The pillars were spun at least 10 rotations total during the deposition in order to insure an even coating. Metal thickness was measured using quartz thickness monitors as it was deposited. In cases of multiple metal layers each layer was 2.5 - 5.0 nm thick amounting to no more than 8 nm total. After metal coating, replication tapes were cut off the solid support taking care to ensure that no carbon tape was included in the excised samples.

## Test tube release and polymer removal

Metal coated nanopillars were released from the surface of the replicating tape by sonication in a standard bath sonicator (Sonicor model SC-50TH) for 15 min. Successful pillar breakage could be visually assessed in gold coated samples as areas of slightly lighter blue tinted replicating tape after sonication. Also, gold coated nano test tubes could be seen as a blue coloring in suspension (Figure 2.6). In order to estimate test tube yield absorbances of test tubes per mg of gold were compared to that of standard gold colloid. 100 μL of suspensions made by sonicating 36 $cm^2$ replicated pillars in 5 ml of water were added to a 96-well plate. Absorbances were measured in a microplate reader (Bio Tek) and adjusted for a path length of 0.29 cm [103]. Absorbances were compared using the peak wavelength of 530 nm for colloidal gold and 650 nm for nano test tubes. The expected mg of gold in the nano test tube sample was calculated assuming a typical 76% yield and tubes with the measured deposited gold thickness (3 nm) on the tips, but only 1 nm gold on their side walls.

In order to track the settling of nano test tubes a similar 36 $cm^2$ sample of 100 nm x 1 μm tubes was used. Settling was followed by adding 2 ml of suspension to a 1 cm plastic cuvette and monitoring the OD600 over time in a spectrophotometer (Eppendorf Biophotometer). The cuvette was capped with parafilm and left undisturbed for the duration of the experiment.

## Test tube particle characterization

Electron microscopy was carried out at the University of Kentucky College of Engineering's Electron Microscopy Center. For scanning electron microscopy (SEM) nano tubes suspended in water were collected by filtering the samples through 20 nm or 200 nm pore size Whatman Anodisc filters. Then the filters were broken into portions and secured on aluminum SEM specimen mounts (Ted Pella #16221) using colloidal graphite (Ted Pella # 16053). Replicating tape and AAO template samples were also cut or broken and mounted for SEM imaging using colloidal graphite. All SEM samples were sputter coated with ~15 nm of gold/palladium for conductivity during SEM imaging. Micrographs were taken in a Hitachi S_4300 scanning electron microscope using the following settings: accelerating voltage = 3.0 kV, aperture = #4, working distance = 15.0 mm, condenser lens setting = 8.0.

In order to check if nano test tubes broke off the replicating tape cleanly or carried a polymer core with them, 200 nm diameter tubes were filtered and exposed to oxidative plasma etching in a plasma cleaner (Harrick) for 40 minutes. Plasma generation settings were $R_f$ = High, $O_2$ flow rate = .8 sccm.

For transmission electron microscopy (TEM) nano test tubes were mounted on Lacey™ carbon grids (Ted Pella #01881). The nano test tubes were mounted by placing the grid onto parafilm and pipetting 5 μL of water onto the TEM grid. Replication tape with metal coated pillars was gently rubbed against the TEM grid / parafilm in this small volume of water. The physical turbulence in a small volume of water acted as a substitute for sonication to release a suitable number of test tubes for TEM imaging. Transmission electron micrographs were obtained using a JEOL 2010 FX microscope operated at 100 kV.

## Nano test tube biotinylation

Multiple approaches were taken in an effort to remove the polymer core from nano test tubes. 36 $cm^2$ of 100 nm x 1 μm imprinted pillars were prepared (~100 $cm^2$ total surface area) and coated with their respective metal(s) then subjected to 1 hr of oxidative plasma etching. The etched tapes were then immersed in water and sonicated for 15 min to break apart tubes. Nano test tubes were filtered from water using a 13 mm diameter Whatman anodisc filter with pore size of 20 nm. Then the tubes / filter were washed three times with acetone and dimethylformamide. The tubes / filter were burned in air in a furnace at $500^oC$ for one hour. Finally, they were washed again with acetone and dimethylformamide.

These “hollowed” tubes were equilibrated for functionalization by rinsing with DMSO, then resuspended by sonication in DMSO with 1 mM biotin-PEG-SH added (monothiolalkane(C11)PEG6-biotin, Sensopath Technologies Inc. part number SPT-0011P6-BIOTIN, MW = 694) (Figure 2.7). After 3 hrs in 1 mM biotin-PEG-SH at room temperature the particles were collected onto a new filter and washed: washes consisted of six 0.5 ml washes of DMSO followed by six 0.5 ml washes with isopropyl alcohol followed by three 0.5 ml washes with water. After washing, the filter was broken and the pieces were immersed in a microfuge tube with 150 μL of a biotin detection kit (Quant Tag, Vector Labs, Inc. part number BDK2000) working solution. 150 μL of Quant Tag working solution was simultaneously added to biotin standard solutions. Metal oxides catalyze the same color change in the Quant Tag working solution as does biotin, however, biotin changes color in minutes while oxides require >30 min, allowing a short window of time to assess the biotin labeling. Samples were sonicated for 5 min in working solution then centrifuged for 30 sec at 13,000 rpm to pellet particles. 100 μL of each standard and sample were transferred to a 96-well plate and absorbances for all wavelengths from 500 nm - 650 nm (535 nm is the wavelength of interest, but assessing spectrums around that value assure that no particles are interfering) were collected immediately using a microplate reader (Bio Tek). Biotin was quantified by comparing the absorbance of samples at 535 nm to a standard curve.

sense 5'-ggggctgcaggtctagggctgcgagccc-3'

antisense 5'-gggctcgcagccctagacctgcagcccc-3'

**Figure 2.1 Dual truncated TOP primers.** The above DNA sequences were used to replace Gly680 of N truncated TOP constructs with a stop codon.

MADIGS then:

16 SSPCSVVNDLRWDLSAQQIEERTRELIEQTKRVYDQVGTQEFEDVSYESTLKALADVEVTY 75

76 TVQRNILDFPQHVSPSKDIRTASTEADKKLSEFDVEMSMREDVYQRIVWLQEKVQKDSLR 135

136 PEAARYLERLIKLGRRNGLHLPRETQENIKRIKKKLSLLCIDFNKNLNEDTTFLPFTLQE 195

196 LGGLPEDFLNSLEKMEDGKLKVTLKYPHYFPLLKKCHVPETRRKVEEAFNSRCKEENSAI 255

256 LKELVTLRAQKSRLLGFHTHADYVLEMNMAKTSQTVATFLDELAQKLKPLGEQERAVILE 315

316 LKRAECERRGLPFDGRIRAWDMRYYMNQVEETRYCVDQNLLKEYFPVQVVTHGLLGIYQE 375

376 LLGLAFHHEEGASAWHEDVRLYTARDAASGEVVGKFYLDLYPREGKYGHAASFGLQPGCL 435

436 RQDGSRQIAIAAMVANFTKPTADAPSLLQHDEVETYFHAFGHVMHQLCSQAEFAMFSGTH 495

496 VERDFVEAPSQMLENWVWEQEPLLRMSRHYRTGSAVPRELLEKLIESRQANTGLFNLRQI 555

556 VLAKVDQALHTQTDADPAEEYARLCQEILGVPATPGTNMPATFGHLAGGYDAQYYGYLWS 615

616 EVYSMDMFHTRFKQEGVLNSKVGMDYRSCILRPGGSEDASAMLRRFLGRDPKQDAFLLSK 675

676 GLQV 679

**Figure 2.2 Amino acid sequence of purified dual truncated TOP.** The above TOP sequence was deduced by trypsin digest followed by MS/MS. The observed total mass was 76,906 kDa, and C-terminal fragment weights agreed with a truncation after Val 679. Fragmentation of the N-terminal fragment revealed an extra 645 Da corresponding to a cloning artifact from the pET32a vector (MADIGS sequence). Mutations other than truncation are highlighted. Numbering scheme is based on the native sequence.

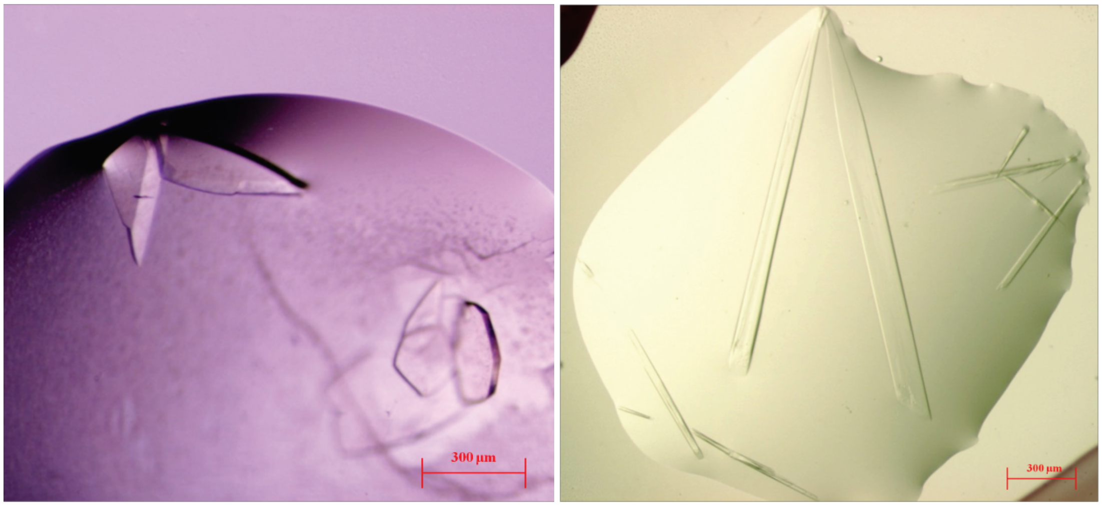

**Figure 2.3 Crystallized TOP. a)** N-truncated TOP crystals **b)** Dual truncated TOP crystals.

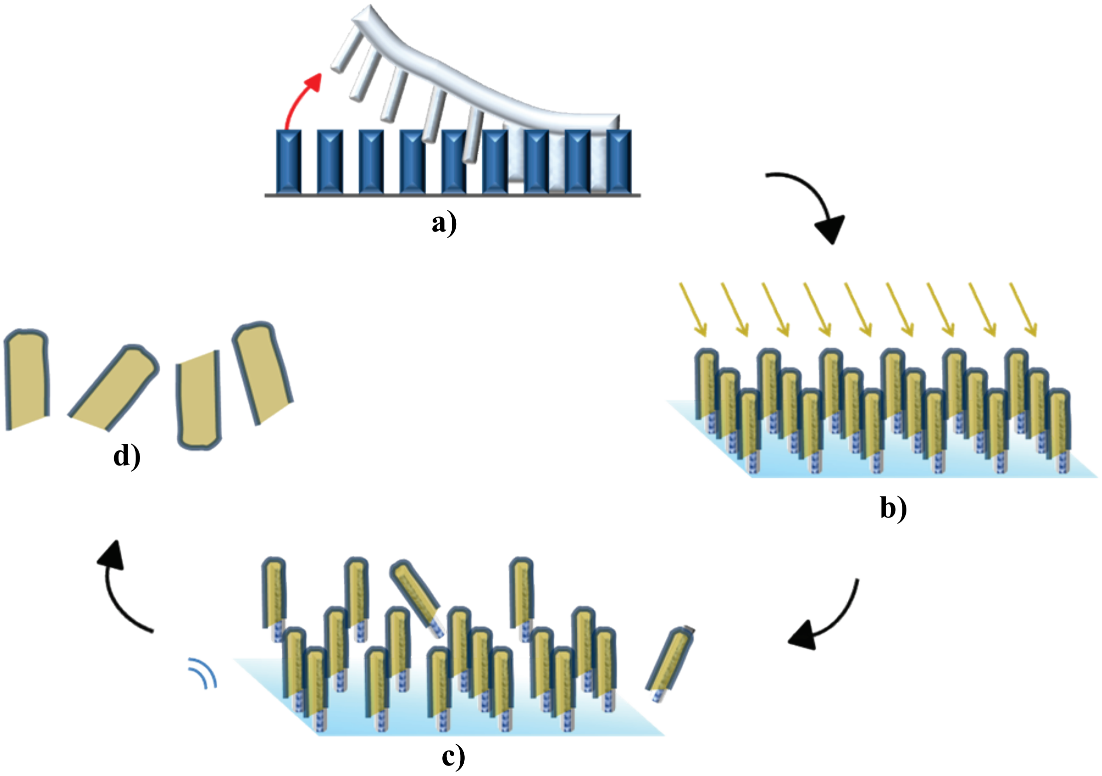

**Figure 2.4 Schematic of non-destructive replication method.** Therapeutic quantities of nano test tubes were synthesized in four stages **a)** Porous alumina formed on a silicon wafer is used to imprint softened polymer multiple times. **b)** Pillared replicas are coated with desired metal(s). **c)** Nano test tubes are freed by sonication in aqueous solution and finally suspended particles are collected **d)**.

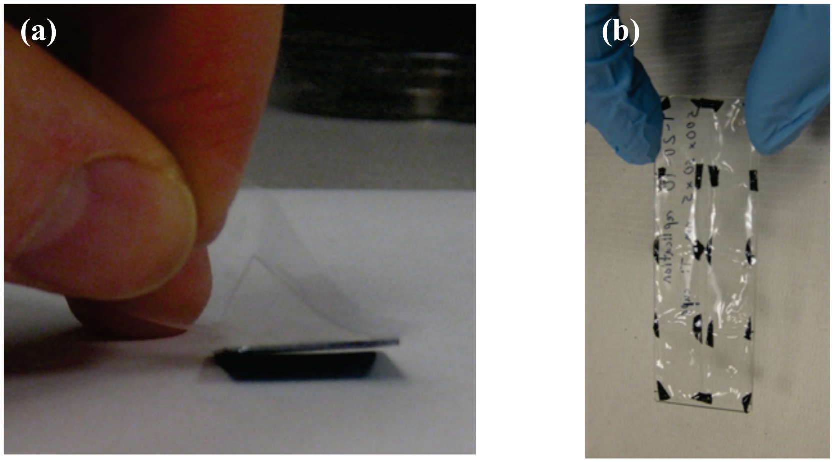

**Figure 2.5  Non-destructive template replication. a)** Imprinting replicating tape from a porous template.  **b)** Preparation for coating.  Double sided carbon tape was used to hold replicated pillars flat against a microscope slide during metal deposition.

**Figure 2.6 Suspended nano test tubes a)** gold/titanium hybrid test tubes (50 nm x 1 μm dimensions) at a concentration of ~7 $cm^2$ pillared replicas per milliliter **b)** pure titanium test tubes of the same size and concentration.

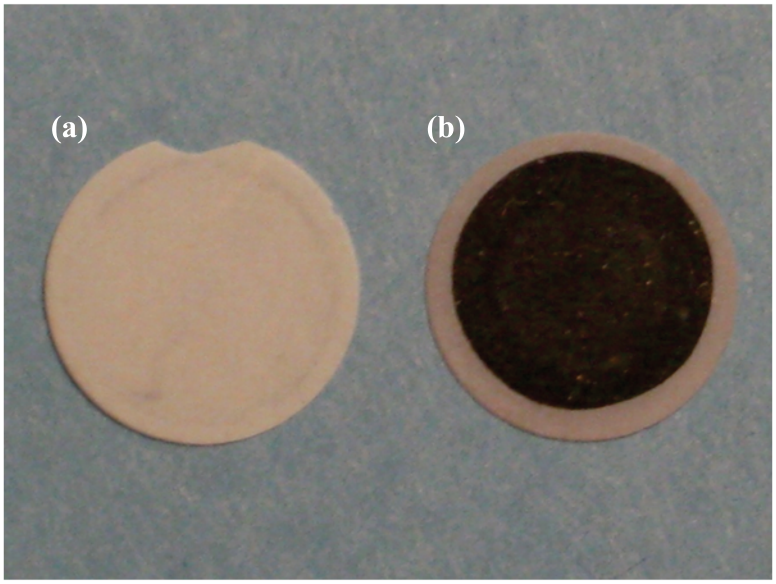

**Figure 2.7 Resuspension of nano test tubes after filtration a)** 20nm AAO filter used for filtering titanium coated gold nano test tubes. Tubes were resuspended from filter by sonication. **b)** A film of tubes remains on filter after parallel experiment using solid gold nano test tubes.

# CHAPTER THREE: Thimet oligopeptidase substrate recognition

Our goal was to understand the molecular mechanism behind the broad substrate recognition of neuropeptidases by mapping the binding surface and determining the number and types of interactions found at the peptidase - peptide interface. We chose TOP as a model neuropeptidase and determined its structure in complex with a variety of substrates by crystal soaking experiments followed by X-ray structure determination. These structures show the extent of the interface that mediates initial substrate interactions and define a new class of peptide binding surface unique to neuropeptidases.

This study is a continuation of work begun previously in the lab by Nick Noinaj. Nick was the first to discover that soaking TOP crystals in dilute substrate solutions allowed substrate complex formation. His subsequent structures allowed modeling of angiotensin II and dynorphin A(1-13) TOP complexes and identified the TOP binding site on domain II across from the active site. These structures explained, in part, TOP's broad sequence recognition and preference for hydrolyzing near the C-termini of substrates. However, angiotensin II and dynorphin A(1-13) are not efficiently hydrolyzed by TOP, and Nick's models of efficiently hydrolyzed substrates suffered from poor occupancy preventing accurate model building. Consequently, he concluded that residual hydrolytic activity was preventing determination of complete TOP / substrate complexes [104]. My structures add eight full-length substrate complexes to the first two including seven substrates that are not considered resistant to TOP hydrolysis. In addition, my improved substrate models and controls for TOP activity clearly indicate that all ten complexes are likely to contain the full-length substrate. Finally, the recapitulation of complex structures using a truncated version of TOP allowed identification of a previously obscured substrate - induced rearrangement of the binding surface.

## TOP constructs used in structural studies

For some of the TOP-peptide crystal structures determined, a TOP construct (residues 16-689) previously reported [49], was used. The C-terminus of this construct is disordered beginning at Leu677 [49]. In the course of the structural studies reported here, additional C-terminal residues appeared in some structures collected from crystals that had formed more than two weeks before being harvested. These structures showed an intermolecular disulfide bond formed between Cys175 and Cys682, and in some cases, I was able to model the remainder of the C-terminal residues. In those cases, the ordered C-terminus reached all the way to the active site zinc ion where the C-terminal carboxylate was seen to participate in coordination of the metal ion (Figure 3.1). Modeling suggested that it was even possible that the C-terminus may interact with the substrate binding site identified in this work, raising concerns about artifacts (Figure 3.2).

To prevent interference with substrate binding in the crystals we designed a truncated construct by changing Gly680 into a stop codon (see Chapter 2). To determine if removing the C-terminus of TOP affected TOP function, we subjected inactive, truncated, TOP to isothermal titration calorimetry (ITC) and found that binding isotherms were identical to untruncated enzyme for representative substrates (see Chapter 4). Similarly, activity assays using quenched fluorescent neurotensin (Abz-NT-edd) showed comparable activity for dual truncated TOP (Figure 3.3). This indicates that removing the C-terminal residues does not significantly alter TOP function.

Dual truncated TOP required new conditions for crystal growth. Final crystallization conditions (100 mM CHES pH 8.3, 400 mM $MgCl_2$, 12-15% PEG 6000) yielded crystals with high resolution diffraction and very similar unit cell parameters as N-truncated TOP (Table 3.1). Phases were found using the N-truncated TOP structure (PDB code 1S4B) for molecular replacement with Phaser [95, 96]. The resulting maps revealed a structure very similar to N-truncated TOP and refined models were superimposible with a rmsd of 0.57Å.

## Choice of substrates for structural study

TOP cleaves a large number of bioactive peptides *in vitro*, and alignment of known cleavage sites reveals no distinguishing features that specify a preferred amino acid sequence. In order to understand how TOP recognizes so many different sequences, substrates were chosen for structural studies to contain as wide a variety of lengths and sequences as possible. Tables 3.2-3.4 summarize substrates and inhibitors used in attempts to determine crystal structures based on the literature reports of cleavage by TOP [16, 24, 25, 105-111]. Only a relatively small number of trials yielded interpretable electron density for ligands (see Tables 3.5, 3.6), and the set of TOP-ligand structures reported here is biased toward enkephalin-like sequences 8-13 residues in length.

For two of the peptides that yielded good complex structures, angiotensin II and dynorphin B(1-9), cleavage by TOP has not been well characterized. Our mass spectrometry analyses of digestion products indicated that angiotensin II is cleaved at Arg2-Val3 (Figure 3.4). In addition, the hydrolysis rate (<5% that of adrenorphin) was found to be particularly slow in one study [110]. Dynorphin B(1-9) is a leu-enkephalin containing opioid peptide fragment reputedly produced in vivo by degradation of dynorphin B(1-13) [112, 113]. It has never been reported as a TOP substrate in the literature.

## Overview of complex structures

In our structures TOP always adopts a fold shaped much like an open clam shell with two large domains divided by a deep cleft. A narrow hinge connects the two domains at the bottom and allows for a large hinge-closing motion like that seen in related enzymes [51, 114]. Domain II coordinates the active site zinc ion located near the bottom of the cleft equidistant from either cleft end. Across the cleft from the active site is a mobile loop predicted to be involved in substrate binding and recognition [115, 116]. Analysis of related peptidase/inhibitor complexes shows that after closure substrates typically orient themselves just above the active site and antiparallel to the innermost strand of the beta sheet located on domain II [51, 52]. Because substrates bridge the interdomain cleft and form interactions with both domains in these closed structures a major goal of this work was to discover which domain(s) interact with substrates in the open conformation during initial substrate recognition.

A major finding of this work is that bound peptides most frequently interact with a surface on the side of the central channel (domain I) opposite the active site rather than directly at the active site as expected. Out of the total of 18 refined crystal structures, ten yielded identifiable ligand density at the domain I substrate-binding site (Figure 3.5). In the case of efficiently processed TOP substrates (adrenorphin, dynorphin A(1-8), dynorphin B(1-9), bradykinin, and neurotensin) only partial density was observed corresponding to the C-termini plus 3-6 residues interacting solely with domain I. This is an indication that initial binding determinants are concentrated near the C-termini of peptide substrates, and a single domain - domain I - is initially responsible for binding substrates. These structures generally became disordered between the P1' and P2 residues where the peptide backbone juts out across the interdomain cleft.

For example, neurotensin (1-13) binds to domain I through residues 7-13 with sequence PRRPYIL. Like all substrates, the neurotensin residues closest to the N-terminus become gradually more disordered so the full shape of proline 7 cannot be distinguished. Therefore, our model includes the sequence ARRPYIL, substituting an alanine for proline 7 (Figure 3.5). The substrate-binding surface is made up of primarily helical elements from domain I. Helices 19 and 21, along with ten loop residues just prior to helix 21, contribute most of the binding surface. Helices 7 and 12 contribute several residues that interact with the C-termini of substrates. Helices 7 and 8 partially close off one end of the surface. The surface is relatively flat, and it is rich in aromatic and hydrophobic residues, making it carbon rich relative to the rest of the enzyme surface. Specifically, the side chains of aromatic residues Tyr221, Phe225, Phe550, Phe598, Tyr605, Tyr609, Tyr612, and hydrophobic residues Leu557, Met594, and Leu613 contribute to the surface. Charged and uncharged polar side chains also contribute including Arg338, Arg553, Gln554, His600, and Glu616. The total surface area interacting with substrates varies between 400-600$A^2$.

## Recognition based on C-terminal residues

The majority of TOP/substrate complexes reveal only partial electron density for ligands (Figure 3.6-3.10), with residues C-terminal to the scissile bond primarily visible. Generally, density for residues N-terminal to the cleavage site is limited to one or a small number of residues, and side chain density is usually not present. More specifically, residues located at positions 4-6 from the C-terminus, corresponding to P2-P1' positions relative to the cleaved bonds are typically less ordered and were modeled as mainchain only. His600, and Tyr612, provide hydrogen bonds to the mainchain carbonyls of those residues 4th and 5th from the C-termini while Tyr605 hydrogen bonds to the amide of the 6th residue suggesting it plays the same role as Tyr486 of PZ Peptidase A [117] and Tyr607 of DCP [51]. The 7th residue from the C-termini invariably becomes too disordered to model in the narrowest part of the cleft between Tyr605 and the active site.

It is possible that the reduced N-terminal residue electron density is due to hydrolysis or partial hydrolysis by the residual activity of the enzyme [104]. An alternative explanation is that the N-termini of the substrates are disordered and so do not result in detectable electron density as they extend out of the identified binding site. In order to resolve these two possibilities, the active site Zn ion was removed by introducing EDTA prior to substrate soaks in order to completely inactivate the enzyme. The resulting complex structures clearly had the Zn removed, but little or no additional density was seen extending out of the domain I binding site (Figure 3.11). (Interestingly, one of the substrates that never yielded identifiable density - LHRH - was found to accelerate removal of the active site Zn by EDTA (Figure 3.12). It might be helpful in the future to include LHRH in EDTA soaks of sensitive crystals in order to lower the soak time.) The only change to ligand density due to Zn ion removal occurred in the case of adrenorphin where a second adrenorphin molecule was found to bind to domain II (Figure 3.13) in the EDTA treated crystals, but density for adrenorphin bound to the original binding site on domain I remains unchanged. Since these carefully inactivated enzyme structures show exactly the same ordered and disordered residues as their Zn containing counterparts it is likely the residues N-terminal to the scissile bond in our TOP complex structure are not well ordered.

The well ordered state of substrate C-terminal residues is consistent with studies showing that TOP recognizes dynorphin A(1-13), neurotensin, and bradykinin via interactions with C-terminal residues and subsequently can become inhibited by C-terminal product fragments [44, 104]. It is also consistent with studies showing that seemingly minor sequence changes near the C-terminus can result in cleavage site shifts [110]. The disordered state of substrate residues adjacent to the cleaved bonds and near the N-terminal suggests that these residues are not involved in initial substrate binding. Each structure showed C-terminal residues interacting with the main binding site on domain I indicating that the TOP binding site selects for C-termini. Thus, a consistent picture emerges where TOP initially recognizes substrates based on residues C-terminal to the cleaved bond, and the orientation of the peptides inside the channel is strictly enforced.

### Binding determinants overview

Aspects of the substrate-binding surface and the observed peptide binding interactions suggest a basis for the broad substrate recognition shown in TOP. The binding interactions are summarized in Table 3.7. There are few polar interactions to side chains that would provide specificity for amino acid type. Instead side chains deploy in shallow grooves that typically can accommodate multiple amino acid classes (Figure 3.14a, Figure 3.15). In contrast, there are often a substantial number of hydrogen bonds to the main chain of the bound peptide, enhancing affinity in a manner largely independent of sequence. These hydrogen bonds are not strongly directional, and the relatively flat binding surface, rich in carbon, allows the peptides to adjust their path to optimize contact and accommodate sequence dependent variations in backbone conformation and side chain placement (Figure 3.14a). Shifts in main chain path across different bound peptides of up to 1 Å occur. In all cases, over 50% of the accessible surface area of the peptide segment is buried in the binding interaction.

Surprisingly, the registration of the scissile bond varies in our structures. In particular, the scissile bond varies by plus or minus one subsite position relative to features of the binding surface (Figure 3.14b), and this registration variability may have implications for the mechanism of substrate binding and cleavage. Given these shifts in registration, we will not use the normal subsite nomenclature for peptidases [118] but simply refer to subsites 1-3, with subsite 1 being closest to directly opposite the active site (Figure 3.16).

Small conformational shifts can be observed when the binding sites of the different peptide complexes are aligned. There are some variations at the C-termini of substrates caused by small concerted movements in the bottom half of domain I (Figure 3.17a,b). These movements are analogous to the differences seen in this domain between the structures of TOP and neurolysin [49], and also between neurolysin and the neurolysin N25 construct [119]. In our structures these shifts never pushed the C-terminus of peptides far enough to result in a new registration, which would be a potential mechanism for final alignment of the scissile bond with the active site that would account for the observed differences in peptide registration. It is tempting, however, to speculate that larger shifts might occur in solution. There are also small changes of side chain conformations in residues of the binding surface as it reorganizes in response to ligand binding, and these also likely contribute to broad substrate sequence recognition (Figure 3.17c).

### Subsite 1

This site (Figure 3.18) interacts with the 3rd or 4th residue from the C terminus in the structures determined. It consists of a shallow groove formed primarily by the aromatic rings of Tyr612 and Phe550 on either side, and the side chain of Glu616 is located at the end of the groove. This subsite is an excellent example of one capable of accommodating different residue types, and the structures determined show leucine, proline, arginine, and lysine residues binding here. The rings of Tyr612 and Phe550 can interact with hydrophobic (or potentially aromatic) side chains and the aliphatic portion of long charged side chains. When arginine or lysine interact at this position they form an additional salt bridge to Glu616 (Figure 3.18). The presence of Glu616 confers some specificity at this site, since it would prevent negatively charged residues from interaction, at least in the same extended conformation as that observed for the bound arginine and lysine side chains.

### Subsite 2

Subsite 2 generally interacts with the 2nd or 3rd residue from substrates' C-termini. Side chains from several hydrophobic/aromatic residues, Leu557, Met594, and Phe598, form most of the subsite surface, although polar or charged side chain and main chain groups from Tyr221, Arg553, Thr597, His600, and Tyr609 also contribute. Unlike subsite 1, subsite 2 has polar residues perfectly oriented to donate two hydrogen bonds to the backbone of substrates. Tyr609 accepts a bond from the backbone amide of the ligand residue occupying the subsite in all complex structure, and Arg553 and Gln554 are both oriented to donate hydrogen bonds to the main chain carbonyl oxygen. In the absence of ligand Gln554 may rotate to donate a hydrogen bond to Tyr609. Residues occupying subsite 2 in the complex structures are highly variable in type, including arginine, histidine, glutamine, leucine, tyrosine, and phenylalanine (Figure 3.19). Again, this subsite is a good example of a portion of the binding site surface that has evolved in such a way as to accommodate a variety of residue types.

### Subsite 3

Subsite 3 (Figure 3.20) interacts with the C-terminus of peptides bound in the standard manner at the substrate binding site, and binding interactions at this subsite are the most variable that were observed. Arg338 and Arg553 make up a prominent portion of subsite 3, but there is also an extensive cluster of aromatic and hydrophobic residues, including Phe550, Met337, Met341, Leu549, Leu584, Tyr220, Tyr221, and F225 that makes up the distal portion of the surface. Many of the side chains making up this subsite adjust their conformations to accommodate different peptide substrates. Arg338, Arg553, Tyr221, and Phe225, in particular, have multiple conformations in the unliganded TOP structure and adapt to the presence of substrates. Residues occupying this subsite are again highly variable in nature with hydrophobic, aromatic, and charged side chains represented in the crystal structures. The side chains deploy in different orientations and in some cases are not well ordered. The C-terminal carboxylate most frequently interacts with Arg338, but it also sometimes interacts with both Arg338 and Arg553 – in one case exclusively with Arg553. The side chains of the two arginines from the enzyme adjust conformation to track the variable positions of the carboxylate oxygens, forming a moldable recognition site for the C-terminus of the peptide (Figure 3.21).

Interestingly, the aromatic residues Tyr221 and Phe225 (from TOP helix 7 and the region N-terminal to it) is a highly conserved motif in TOP orthologs (Figure 3.22) confirming the observation here that it plays an important role in substrate binding. Along with Tyr224 this aromatic cluster largely makes up the surface that partially closes off one end of the substrate binding site (Figure 3.20). Any substrate binding in such a way as to extend beyond this defined end of the site would have to adopt a sharp turn in main chain path in order to avoid this cluster of side chains. The positions of Tyr221 and Phe225 are variable in unliganded TOP, and they can be crowded into a variety of positions by the C-terminal residue of substrates (Figure 3.17c).

Taken together, these three subsites clearly allow binding of many diverse sequences. How then is any specificity toward the recognized cleavage site sequences achieved? One easy example would be the exclusion of negatively charged residues from subsite 1 due to the presence of Glu616. In addition, amino acids such as glycine, alanine, and serine with short and/or polar side chains would leave subsites unfilled or interact in an energetically unfavorable manner with hydrophobic portions of the subsites. Interestingly, affinity for amino acids with larger side chains is shared in peptide recognition by the major histocompatability complex proteins of the immune system, which use aliphatic or charged residues at or near the C-terminus of peptides to anchor binding [120].

## Differences in the dual truncated form of TOP: the 599-611 residue region

As noted, concern over possible interaction with the C-terminus of an adjacent TOP molecule prompted use of a TOP construct in which the unstructured C-terminal residues had been removed. The only significant differences between the backbones of dual truncated and N truncated TOP near the substrate-binding and active sites were found in the open coil region N-terminal to helix 21 (residues 599-611). In dual truncated TOP Tyr605 points across the interdomain cleft towards Asp83 and His600 points towards the interior of TOP where it forms a hydrogen bond to the mainchain carbonyl of Tyr605. In N truncated TOP described by Ray et. al. [49] Tyr605 swings 5.2A$^{o}$ towards the active site carrying the backbone of residues 603-605 up to 1.8A$^{o}$ towards His600. His600 adopts a new rotamer and faces solvent instead of hydrogen bonding to the backbone carbonyl of Tyr605. Also, in N truncated TOP Arg498 adopts a more extended side chain rotamer, but in dual truncated TOP Tyr605 forces Arg498 into a less extended conformation.

Subsequent structures of dual truncated TOP with substrates induced conformational changes resulting in a return to the conformation of the 599-611 region seen in structures determined from crystals containing the full C-terminus of TOP. A possible explanation for the observed structural difference is that interaction of the C-terminus of a neighboring TOP molecule with the active site region (see Figure 3.23) displaces the conformation of the 599-611 region. In particular, it might shift Gly603-Tyr605 in the 599-611 loop into the liganded conformation. An alternative explanation is that the C-terminus of an adjacent molecule interacts in a disordered way with the substrate-binding site, altering the conformation of the 599-611 region in the same manner as a bound substrate peptide. The C-terminal residues would have to be sufficiently disordered so as to not give rise to substantial electron density in the crystal structures, since none is observed.

The rearrangements of the 599-611 region are stabilized by hydrogen bonds that form to substrates consistent with mutational studies replacing glycines with alanines and/or tyrosines with phenylalanines [115]. The increased backbone flexibility provided by conserved glycines 599, 603, and 604 is key in permitting rearrangement of the 599-611 loop. Substrate binding causes a moderate displacement of Gly603 and Gly604 along with Tyr605, allowing Tyr605 to hydrogen bond to the substrate backbone. Aided by the flexibility of Gly599, His600 shifts and adopts a new rotamer allowing it to hydrogen bond to substrate backbone as well (Figure 3.23a). Interestingly, Gly611 and Tyr612 do not undergo a significant movement upon substrate binding, but Tyr612 still forms a hydrogen bond to the backbone of most of the substrates.

It does not appear that mobility in the 599-611 region plays a role in accommodating different substrate sequences when they bind in the standard manner to the substrate-binding surface. The conformations of this region are bimodal, with only the unliganded and liganded conformations observed. No significant conformational differences are observed when all of the dual truncated TOP ligand-bound structures are superimposed (Figure 3.23b). This suggests that the mobility of conserved glycines in this region does not support broad recognition but perhaps to some extent provides for an entropic cost that allows for specificity without excessively high affinity, as has been suggested for unstructured regions [121].

## Individual substrate analysis and exceptions

### Angiotensin II

Angiotensin II is an eight residue (DRVYIHPF) vasoconstricting peptide that plays a role in blood pressure regulation, and a structural relative of TOP known as angiotensin converting enzyme (ACE), produces this peptide from a larger precursor. TOP has also been identified as a protein that binds tightly to angiotensin II in the cytoplasm [122, 123]. Also, an enzyme closely related to TOP, neurolysin, has recently been identified as a tight binding membrane receptor for angiotensin II [124]. The structural determinants of angiotensin II binding to TOP are of interest for predicting the binding site on all family members including neurolysin and ACE, which is of considerable interest in understanding the physiological roles of the peptide.

I was able to determine a high quality structure of angiotensin II bound to TOP. Interestingly, this peptide extends out of the substrate-binding site to cross the interdomain channel of TOP and interact at the active site (Figure 3.24). The first four residues form a short alpha helical structure and the N-terminal Asp1 coordinates the active site Zn ion. The last four residues interact with the substrate-binding site in a conformation similar to other bound substrate peptides. Ile5 from the peptide extends into hydrophobic subsite 1. His6 extends into hydrophobic subsite 2. Pro7 and Phe8 displace Phe550 and the phenyl ring of Phe8 reaches deep into subsite 3 beyond the C-terminal recognition motif (Figure 3.24c). The orientation of angiotensin II brings the alpha carbonyl of Tyr4 into position for hydrogen bonding with His600. Consequently, His600 partitions into its “liganded” rotamer. Interestingly, Tyr605 does not follow His600 into the “liganded” conformation (Figure 3.24g). This could be due to the orientation of angiotensin II which carries the backbone out of range to hydrogen bond to the "liganded" conformation of Tyr605, or it could be due to interference from the (disordered) side chain of Tyr4. In any case, it is notable that His600 can move independently of Tyr605 since in all other structures these two residues make a coordinated switch to the liganded form. Also of note, in the N truncated TOP - angiotensin II complex Tyr605 does assume the liganded conformation, providing evidence that angiotensin II and the disordered C-terminal tail of a neighboring TOP molecule are simultaneously present in the vicinity of Tyr605.

Angiotensin II interacts mostly with the domain I binding site. However, it forms two powerful interactions to domain II. First, as noted, the carboxylic acid of Asp1 participate in coordination of the active site Zn. Second, Arg2 forms ionic interactions with Glu469 and Glu509 (Figure 3.24f). Anchored in this way to the active site, angiotensin II cannot be placed into position for hydrolysis of a peptide bond by the hinge like conformational change of the enzyme. The structure, therefore, explains the extremely slow hydrolysis of angiotensin II (<5% hydrolysis rate as compared to adrenorphin [110]) and it is likely that rearrangement to another, less favorable binding interaction is required for hydrolysis by TOP.

### Immunoglobulin G4

Immunoglobulin G4 (IgG4) residues 279-287 (DSDGSFFLY) have been reported as a tight binding TOP ligand that is resistant to hydrolysis [16]. We determined the structure of IgG4 complexed to TOP to 2.5Å (Figure 3.25). The electron density is strong for the ligand, suggesting that IgG4 binds with high occupancy to the open conformation of TOP consistent with the reported $K_i$ of 0.3μM. The peptide binds to the same domain

I binding site as other substrates, but it adopts a different orientation, pointing across the interdomain cleft directly at the active site. Also, unlike most substrates, this sequence has no interaction between the C-terminal carboxyl and Arg338. Instead the peptide C-terminus interacts with Arg553 and the terminal tyrosine side chain extends into subsite 2.

Perhaps the most striking feature of the TOP - IgG4 complex structure is that it binds to the "unliganded" conformation of the 599-611 loop. The orientation of IgG4 does not induce the conformational changes in His600 or Tyr605 that normally accompany peptide interaction with the binding site. As a consequence of its unusual interaction with the binding site, IgG4 has relatively few hydrogen bonds formed to its main chain for those residues interacting with domain I. The bound peptide also interacts extensively with domain II, however. The first four residues form backbone interactions with TOP's beta sheet and the carboxyl group of Gly4 displaces the catalytic water at the active site to coordinate the active site Zn ion (Figure 3.25). The observed registration of IgG4 would place the backbone of Phe7 in position to hydrogen bond with His600 and Phe6 to hydrogen bond with Tyr605 if it followed the typical path of substrates. However, IgG4 is similar to angiotensin II in that it spans the cleft directly towards the active site Zn. This means Phe6 is too far from Tyr605 to interact with the liganded conformation of the 599-611 region. The backbone carbonyl of Phe7 is actually in the correct place to interact with His600, however, the sidechain of Tyr8 appears to sterically restrict His600 from adopting its normal bound - ligand conformation. Like angiotensin II, the orientation of IgG4 and its coordination of the active site Zn ion prevent it from being aligned for hydrolysis. In this case also, then, the bound structure is consistent and provides an explanation for the lack of or low activity of TOP with this peptide.

### Adrenorphin

Adrenorphin is a C-teminal amidated peptide cleaved three residues from the C-terminus by TOP. The structure of TOP with bound adrenorphin is unique in that two adrenorphin molecules bind in the central channel of the enzyme, one in the expected binding site in a fashion very similar to dynorphin A(1-8) and the other on domain II lying across the active site. In interacting with domain II, adrenorphin does not bind in a registration relative to the active site consistent with the known cleavage site (Figure 3.13). Also, adrenorphin only achieves high occupancy at the domain II site in the absence of the active site Zn ion. Structures of TOP complexed to adrenorphin without co-incubation with EDTA do not have adrenorphin bound to domain II. Furthermore, cleavage assays of adrenorphin with catalytically compromised, E474A TOP, showed only the predicted YGGFM - RRV cleavage site. Together these indicate that the presence of Zn ion prevents domain II binding, probably by blocking Val8 of the peptide from interacting with the pocket formed by Ala474 and Thr470.

The productive mode of adrenorphin binding, therefore, is most likely through initial interaction with the domain I binding site as seen in the dual truncated TOP complex with Zn present (Figure 3.19a, b). Adrenorphin binding to domain I is very similar to other substrates so it seems that its binding to domain II, although instructive, is merely an artifact of the TOP construct used and the soak conditions which removed the active site Zn ion.

**Luteinizing hormone releasing hormone and dynorphin B.**

During the course of this work hundreds of TOP crystals have been grown and subjected to various ligand-containing solutions. Most ligand solutions had only minor effects similar to what might be expected from small changes to the enzyme structure. However, there were at least two exceptions worth noting. First, N truncated and dual truncated TOP crystals soaked with luteinizing hormone releasing hormone (LHRH, sequence EHWSYGLRPG) in the presence of EDTA lost their active site Zn ion in less than 30 minutes of soak time (Figure 3.12). This is particularly surprising since this peptides was not seen binding in the structures determined from soaked crystals. Interestingly, LHRH was reported as not being a substrate for TOP [111]. LHRH must in some way interact at the active site to affect Zn ion binding, however, it clearly does not have a high affinity interaction with the enzyme.

Another peptide of particular interest is dynorphin B. Both dynorphin(1-9) (YGGFLRRQF) and dynorphin B(1-13) (YGGFLRRQFKVVT) had the effect of introducing disorder into the crystal lattice. The result was many poorly diffracting crystals being mounted for collection. It made no difference which TOP construct was used or what soak conditions were tried. However, we were persistent with the nine residue substrate and eventually determined structures from relatively resilient crystals without seriously damaged lattices. This could be interpreted several ways, but one possibility is that the dynorphin B sequence is particularly good at inducing closure of TOP’s large interdomain cleft. This substrate might be a good tool during crystallization screens to lock inactivated TOP in its closed structure.

### Non-peptide inhibitor soaks

Many TOP and neurolysin inhibitors have been developed and those that were available to us were soaked into TOP crystals in much the same way as peptides. Previous work in the lab attempting to soak crystals in inhibitor were ended when the crystals disintegrated. This was thought to be an indication of large conformational changes induced by the inhibitors [104]. However, in my work, TOP crystals were successfully soaked in concentrated solutions of inhibitors without dissolving or becoming disordered (Table 3.4). The key was to carefully control the pH of soaking solutions as inhibitors are generally provided in a form that results in acidification of solutions.

Despite preserving the crystal quality during soaking in inhibitor solutions, no clearly identifiable density for any of the inhibitors could be seen in the resulting structures. In the case of phosphinic compounds 3 and 5 (predicted MW = 766.8 and MW = 678.7 respectively) the true identity of the molecules is doubtful since mass spectrometry yielded masses of 503.2 and 697.3 for the inhibitors. But in the case of “Mia” (aka C28), cFP-AAF-pAB, and phosphinic compound 6 the identity of the molecules is certain. The lack of complex formation with these high affinity inhibitors is disconcerting. It may be due to the crystal lattice imposing the open conformation on TOP molecules in the crystal, but more experiments are necessary to be certain.

### Substrate fragments RPKLK and RPYIL

Dynorphin A(9-13) and neurotensin (9-13) were soaked into crystals to test the effects of leaving out residues N-terminal to the cleavage site. Structures yielded difference electron density corresponding to the expected fragments (Figure 3.26).

The product fragment dynorphin A(9-13) interacts in the same register on domain I as the full thirteen residue substrate does. This is consistent with the similar binding affinity seen for dynorphin A(1-13) and dynorphin A(9-13) in competitive inhibition assays [104]. However, the structure with dynorphin A(9-13) also shows that a second dynorphin A(9-13) molecule binds to domain II through a variety of interactions including Zn ion coordination (Figure 3.27).

Similarly the neurotensin (9-13) fragment binds to domain II and coordinates the Zn ion (Figure 3.28). But unlike the full length neurotensin the fragment gives rise to electron density at the domain I site only in subsites 2 and 3, and the observed density is not well defined. Difference density of neurotensin (9-13) after initial rigid body refinement with unliganded TOP is clearly displaced compared to full-length neurotensin (Figure 3.26c). Furthermore, the fragment only partly induces the His600 rotamer shift and none of the Tyr605/Arg498 movement seen with full-length neurotensin and other fully bound peptides. This is perhaps not surprising given that Tyr605 normally hydrogen bonds to the backbone carbonyl of Arg8, which is missing in this short fragment. Since the expected full-length neurotensin density is seen with other C-truncated TOP structures (without any EDTA soaking) this eliminates the possibility that former neurotensin structures might have been cleavage products left over from residual activity [104]. More importantly, it may indicate a role for the unseen N-terminal residues of neurotensin even in initial substrate binding to the open form of TOP.

In general, interaction primarily with residues C-terminal to the scissile bond in the open conformation of TOP has consequences for the catalytic cycle of the enzyme. After hydrolysis and resumption of the open enzyme conformation, the N-terminal product fragment likely diffuses rapidly out of the central channel. The C-terminal fragment, however, will still be bound nearly as tightly as the full length peptide. It seems, then, that the release of the C-terminal product fragment is likely rate limiting for many or all substrates. In the case of dynorphin A(1-13) which is a reported inhibitor of TOP [104], the C-terminal product clearly binds so tightly as to effectively inhibit the enzyme. Given the observed binding of some peptides to domain II, it is also possible that some products bind near the active site in a way that would also inhibit the enzyme, potentially further complicating the catalytic cycle. In that sense, it is tempting to speculate that the faster turnover rates seen for substrates with shorter C-terminal product fragments [125] is due to lack of binding affinity between those product fragments and domain I or domain II.

## Table 3.1 Crystallographic statistics for unliganded dual truncated TOP

| | |
|---|---|
| **Data collection**[1] | |
| Space group | $P2_12_12_1$ |
| Cell dimensions | |
| a, b, c (Å) | 77.9, 103.1, 106.2 |
| $\alpha, \beta, \gamma$ (°) | 90, 90, 90 |
| Resolution (Å) | 2.00(2.00-2.07) |
| $R_{sym}$ | .096(.560) |
| $I / \sigma I$ | 15.2(1.9) |
| Completeness (%) | 99.3(97.0) |
| Redundancy | 4.9(4.4) |
| | |
| **Refinement** | |
| Resolution (Å) | 2.00-43.0 |
| No. reflections | 54365 |
| $R_{work} / R_{free}$ | .1804/.2204 |
| No. atoms | |
| Protein | 5338 |
| Ligand/ion | 1 |
| Water | 482 |
| B-factors | |
| Protein | 29.4 |
| Ligand | n/a |
| Water | 36.1 |
| r.m.s. deviations | |
| Bond lengths (Å) | .006 |
| Bond angles (°) | .984 |

1. Single crystal. 2. Values in parentheses are for highest-resolution shell.

## Table 3.2 Substrate soaks with N truncated TOP

| Peptide | Sequence and modifications | Date collected | Resolution (A$^{o}$) | Activity control | Result |
|---|---|---|---|---|---|
| adrenorphin | YGGFM-RRV-NH$_2$ | Dec-09 | 2.17 | no Zn | Good density along domain II |
| angiotensin I | DRVYIHP-FHL | Apr-10 | 2.10 | Zn | Ambiguous density |
| angiotensin II | DR-VYIHPF | Apr-10 | 1.97 | Zn | Very good density domain I |
| beta amyloid 1-42 | DAGFGHD……..LMVGGVV | Oct-09 | 2.38 | Zn | No substrate density |
| bradykinin | RPPGF-SPFR | Aug-10 | 1.80 | Zn | Good density along domain I |
| dynorphin A 1-8 | YGGFL-R-RI | Dec-10 | 2.45 | Zn | Very good density domain I |
| dynorphin A 1-8 | YGGFL-R-RI | Aug-11 | 2.20 | no Zn | Good density domain I |
| dynorphin A 1-8 D8 | YGGFL-R-RD | Mar-09 | 2.00 | Zn | Very good density domain I |
| dynorphin A 1-13 | YGGFL-RRI-RPKLK | Nov-08 | 1.97 | no Zn | Very good density domain I |
| dynorphin A 1-17 | YGGFL-RRIRPKLKWDNQ | Oct-09 | 1.97 | Zn | Ambiguous density |
| dynorphin B 1-9 | YGGFLR-RQF | Jun-09 | 2.24 | Zn | Good density domain I |
| dynorphin B 1-9 | YGGFLR-RQF | Oct-09 | 2.10 | no Zn | Good density domain I |
| hemopressin | PVNF-K-F-LSH | Oct-09 | 2.28 | no Zn | Too little density |
| lut. horm. rel. horm. (LHRH) | EH-WSY-GLRPG-OH | Dec-09 | 1.80 | Zn | Too little density |
| lut. horm. rel. horm. (LHRH) | EH-WSY-GLRPG-NH$_2$ | Apr-10 | 2.60 | no Zn | Too little density |
| neurotensin | ELYENKPR-RPYIL | Dec-09 | 2.36 | Zn | Good density domain I |
| peptidylprolyl isomerase A (PPI) | ELFADKVPKTA-ENFR | Aug-10 | 2.50 | Zn | Too little density |
| proctolin | RYLPT | Nov-08 | 1.83 | Zn | Ambiguous density |
| somatostatin | AGCKN-F-FWKT-FTSC | Jun-09 | 2.07 | Zn | Too little density |
| Substance P | RPKPQ-QF-F-GLM-NH$_2$ | Mar-09 | 1.92 | no Zn | No substrate density |
| eukaryotic transl. init. factor 5a (TIF) | SAMTEEAAVAIK-AMAK | Apr-10 | 3.00 | Zn | Too little density |
| vaso. intest. peptide (VIP) | HSEAVFTDNYTRLRKQMAVKKYLNSILN | Jun-09 | 2.03 | Zn | Too little density |
| No substrate | none | Aug-10 | 2.30 | Zn | No substrate density |

*Each structure summarized here represents the best of multiple structures taken on multiple occasions. Most sequences exhibited at least a small amount of difference density in the binding site located on domain I, but achieving high enough occupancy to model the substrate unambiguously occurred only in fewer than half of cases.

# Table 3.3 Substrate soaks with dual truncated TOP

| Ligand | Sequence and modifications | Date collected | Resolution (A$^{o}$) | Domain I binding? | Domain II binding? |
|---|---|---|---|---|---|
| adrenorphin | YGGFM-RRV-$NH_2$ | Feb-12 | 2.45 | C-terminal, ambiguous registration | No |
| angiotensin II | DR-VYIHPF | Aug-11 | 2.50 | Good density domain I | No |
| bradykinin | RPPGF-SPFR | Oct-11 | 2.20 | Good density domain I | No |
| dynorphin A 1-8 | YGGFL-R-RI | Oct-11 | 2.90 | Good density domain I | No |
| dynorphin A 1-13 | YGGFL-RRI-RPKLK | Jun-11 | 3.00 | Good density domain I | No |
| dynorphin B 1-9 | YGGFLR-RQF | Dec-11 | 2.80 | Good density domain I | No |
| dynorphin A 9-13 | RPKLK | Jun-12 | 2.80 | Good density | Good density |
| IgG4 | DSDGSFFLY | Jul-12 | 2.50 | Good density | OK density |
| lut. horm. rel. horm. (LHRH) | EH-WSY-GLRPG-$NH_2$ | Aug-11 | 3.00 | Too little density | No - but Zn displaced |
| MHC epitope Pb | SYIPSAEKI | Jun-12 | 2.25 | Too little density | No |
| MHC epitope MAGE-1 | EADPTGHSY | Jun-12 | 2.70 | C-terminal, ambiguous registration | No |
| neurotensin 1-13 | ELYENKPR-RPYIL | Aug-11 | 3.10 | Good density | ?? |
| neurotensin 9-13 | RPYIL | Feb-12 | 2.40 | Novel, ambiguous, binding | Good density |
| none | none | Dec-11 | 2.00 | No | No |
| phosphinic compound 6 | MW = 452.2 | Dec-11 | 2.40 | No | No |
| Somatostatin | AGCKN-F-FWKT-FTSC | Dec-11 | 2.50 | No | No |
| Substance P | RPKPQ-QF-F-GLM-NH2 | Dec-11 | 2.40 | No | No |

*Each structure summarized here represents the best (in terms of substrate occupancy) of multiple attempts.

## Table 3.4 TOP inhibitor soaks attempted

| TOP construct | Inhibitor | Date collected | Resolution | Concentration | Time | Identity confirmed? |
|---|---|---|---|---|---|---|
| Active, N truncated | "Mia" or "C28" | Mar-12 | 1.90 | ~.1mM | 45min | Made from powder |
| Active, N truncated | cFP-AAF-pAB | Mar-12 | 2.00 | ~5mM | 45min | Made from powder |
| E474A, N truncated | phosphinic cmp 3 | Dec-10 | 2.65 | 2mM | 45min | MW by MS/MS = 503.2 |
| E474A, N truncated | phosphinic cmp 5 | Dec-10 | 3.00 | 2mM | 30min | MW by MS/MS = 697.3 |
| E474A, N truncated | phosphinic cmp 6 | Dec-10 | 2.10 | 2mM | 75min | MW by MS/MS = 452.2 |
| E474A, dual truncated | phosphinic cmp 6 | Dec-11 | 2.40 | 2mM | 5min | MW by MS/MS = 452.2 |

*Only phosphinic compound 6 structure had noteworthy electron density in the binding site.

## Table 3.5 N truncated TOP structure statistics

| | angiotensin II | adrenorphin | bradykinin | dynorphin A(1-8) | dynorphin A(1-8) D8 | dynorphin A(1-13) | dynorphin B(1-9) | neurotensin |
|---|---|---|---|---|---|---|---|---|
| **Resolution(A$^o$)** | 1.97(1.97-2.04) | 2.20(2.20-2.28) | 1.80(1.80-1.86) | 2.00(2.00-2.07) | 2.00(2.00-2.07) | 1.90(1.90-1.97) | 2.10(2.10-2.18) | 2.33(2.33-2.41) |
| **Reflections** | 55860 | 38749 | 73337 | 50512 | 55363 | 53789 | 44282 | 32215 |
| **$R_{sym}$** | .092(.705) | .112(.646 ) | .060(.569) | .087(.527) | .090 (.614 ) | .076 (.517 ) | .101(.564) | .126(.595 ) |
| **I/σI** | 15.5(2.2) | 12.4(2.11) | 22.2(2.81) | 15.3(2.0) | 15.7(2.74) | 17.4(2.51) | 10.5(2.62) | 11.3(2.08) |
| **Completeness** | 99.7(99.3) | 95.3(97.2) | 98.2() | 95.6(82.9) | 99.8(99.1) | 94.3(90.6) | 96.7(98.3) | 99.7(97.7) |
| **Redundancy** | 4.8(4.5) | 5.1(4.8) | 5.0(4.9) | 4.9(4.0) | 5.5(4.2) | 4.9(4.0) | 5.1(5.1) | 4.5(3.4) |
| **$R/R_{free}$** | .1998 / .2374 | .1965/.2415 | .1789/.2055 | .1934 / .2335 | .1939/.2272 | .2015/.2333 | .2061/.2411 | .1937/.2279 |

## Table 3.6 Dual truncated TOP structure statistics

| | **angiotensin II** | **adrenorphin** | **bradykinin** | **dynorphin A(1-8)** | **dynorphin A(1-13)** | **dynorphin B(1-9)** | **neurotensin** | **IgG4** | **RPKLK** | **RPYIL** |
|---|---|---|---|---|---|---|---|---|---|---|
| **Resolution(A$^{o}$)** | 2.50(2.50-2.59) | 2.40(2.40-2.49) | 2.20(2.20-2.28) | 2.90(2.90-3.00) | 3.00(3.00-3.11) | 2.80(2.80-2.90) | 3.10(3.10-3.21) | 2.50 (2.50-2.59) | 2.80(2.80-2.90) | 2.45(2.45-2.54) |
| **Reflections** | 27908 | 32260 | 39864 | 16745 | 15962 | 20092 | 14945 | 25900 | 19408 | 28331 |
| **$R_{sym}$** | .081(.356) | .090(.389) | .075(.378) | .113 (.405) | .076 (.517 ) | .141 (.536) | .142 (.458) | .118(.635) | .109(.503) | .078(.540) |
| **I/σI** | 13.4(2.18) | 15.6(2.5) | 16.6(2.88) | 10.3(2.32) | 3.46(2.38) | 11.4(1.9) | 8.41(2.04) | 12.7(2.18) | 11.8(2.23) | 18.9(2.47) |
| **Completeness** | 90.0(97.1) | 98.8(94.0) | 95.1(88.6) | 90.4(93.6) | 93.6(92.2) | 98.6(91.8) | 98.0(90.6) | 91.3(93.6) | 94.8(87.4) | 93.7(92.7) |
| **Redundancy** | 3.6(3.3) | 4.3(3.8) | 4.3(4.3) | 4.0(3.9) | 4.5(4.8) | 5.4(4.1) | 3.3(3.5) | 4.9(4.4) | 5.0(4.9) | 5.1(4.4) |
| **$R/R_{free}$** | .1948/.2484 | .1802 / .2205 | .1948/.2484 | .2010/.2498 | .2006/.2319 | .1951/.2437 | .1893/.2400 | .1916/.2469 | .1935/.2503 | .1893/.2392 |

**Table 3.7 Interactions formed between the TOP binding site(s) and substrates.**

| Substrate Complex | Coordinates used | Sequence modeled | Salt bridges | H-bonds mainchain | H-bonds side chains | Peptide interfacial surface area ($A^2$) | Total Δ ASA ($A^2$) | Energy of solvation (kcal/mol) |
|---|---|---|---|---|---|---|---|---|
| **Adrenorphin** | adren_e_s_dec09_refine_13.pdb | AARRV | 0[1] | 3 | 2 | 509(57%) | 992[2] | -.6 |
| **Angiotensin II** | ang2_edta_refine_11-coot-0.pdb | DRVAIHPF | 4<br>(R338/R553, E469/E509) | 4 | 0 | 822(67%) | 1451 | - 5.9* |
| **Bradykinin** | brady_e_aug10_refine_20.pdb | ASPFA | 2<br>(R338/R553) | 6 | 0 | 442(58%) | 869 | -6.0 |
| **Dynorphin A (1-8)** | top_dyn8_e_refine_20.pdb | GFARRI | 3<br>(R338/R553, E616) | 6 | 2 | 593(54%) | 1123 | -2.3 |
| **Dynorphin A (1-13)** | dyn13_edta_refine_1 .pdb | ARPKLA | 3<br>(R338/R553, E616) | 6 | 0 | 532(50%) | 1038 | -3.9 |
| **Dynorphin B (1-9)** | top679_dynb9_dec11_refine_10.pdb | AAARQA | 3<br>(R338/R553, E616) | 6 | 0 | 548(55%) | 1029 | -2.0 |
| **IgG4** | top679_igg4_1_jul12_refine_4.pdb | ASDGSAALY | $1^{(R553)}$ | 6 | 2 | 693(56%) | 1211 | -2.9* |
| **Neurotensin** | top_nt_dec09_refine_5 | ARAPYIL | $1^{(R553)}$ | 7 | 0 | 650(58%) | 1240 | -5.6 |

**Table 3.7 continued**

| Peptide complex or model | Coordinates used | Sequence modeled | Salt bridges | H-bonds mainchain | H-bonds side chains | Peptide Δ ASA ($A^2$) | Total Δ ASA ($A^2$) | Energy of solvation (kcal/mol) |
|---|---|---|---|---|---|---|---|---|
| **Domain II adrenorphin** | adren_e_s_dec09_refine_13.pdb | FMRRV | 0 | 5 | 2 | 647(67%) | 990 | -4.5 |
| **Domain II dynorphin A (9-13)** | top679_rpklk_jun12_refine_5.pdb | RPKLK | $3^{(D83,D102,H473)}$ | 4 | 2 | 588(62%) | 976 | -1.0* |
| **Domain II neurotensin (9-13)** | top679_RPYIL_feb12_refine_9.pdb | RPYIL | $3^{(D83,D102,H473)}$ | 5 | 5 | 55.8(67%) | 901 | -1.6* |
| **Domain I dynorphin A (9-13)** | top679_rpklk_jun12_refine_5.pdb | RPKLK | $3^{(R338/553,E616)}$ | 7 | 0 | 498(54%) | 903 | -2.2 |
| **TOP C-terminal** | top_Cterm_dyn8d8_2_refine_4.pdb | GCEPEPQVA | 0 | 6 | 1 | 580(48%) | 975 | -8.4 |

[1]Salt bridges and hydrogen bonds were counted using COOT. A cutoff of 3.5 $A^o$ was used for salt bridges and hydrogen bonds. In the case of bifurcated interactions, bonds were counted up to twice. [2]Changes in accessible surface area and energies of solvation were calculated using the PDBe PISA webserver. $74A^2$ buried TOP surface and -1.2 kcal/mol energy of solvation were added where appropriate due to 599-611 loop rearrangement. *No adjustments made for 599-611 rearrangement or Zn coordination

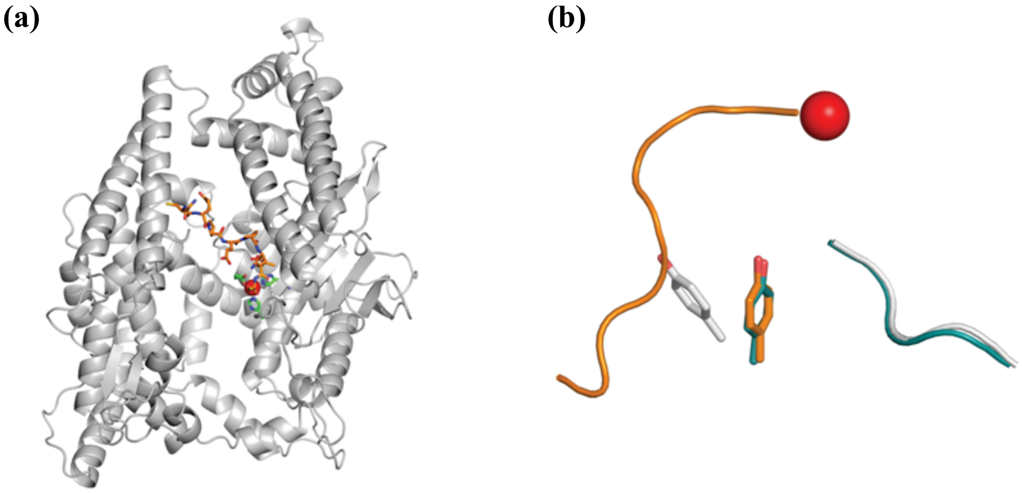

**Figure 3.1 C-terminus of symmetry related TOP. a)** C-terminus of a neighboring molecule forms intermolecular interactions near the 599-611 loop and at the active site Zn. Dynorphin A(1-8) Asp8 (March 2009) soaked crystal was used to model additional, typically disordered, TOP residues 682-689 that yielded good density. **b)** Model of TOP C-terminus using Tyr605 to represent the conformational change in the 599-611 loop. Unliganded N truncated TOP model is in orange, the unliganded dual truncated structure is in white, and the liganded dual truncated structure with dynorphin A(1-8) is in blue.

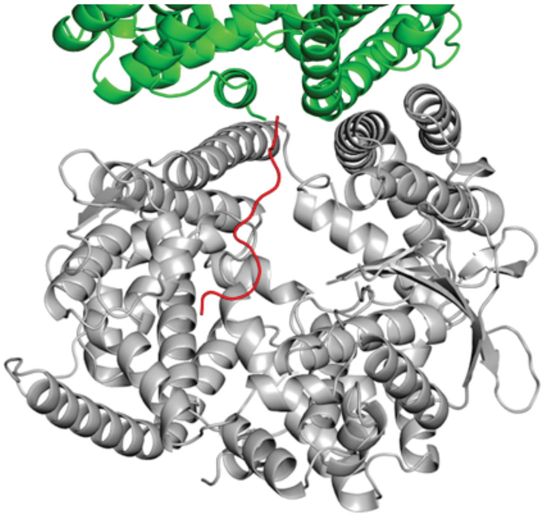

**Figure 3.2  Length of disordered residues.** Twelve disordered residues are sufficient to reach the substrate binding site on domain I from a neighboring TOP molecule. A ribbons view of TOP is in gray, a neighboring TOP molecule is in green, and a modeled conformation for the C-terminal residues is in red.

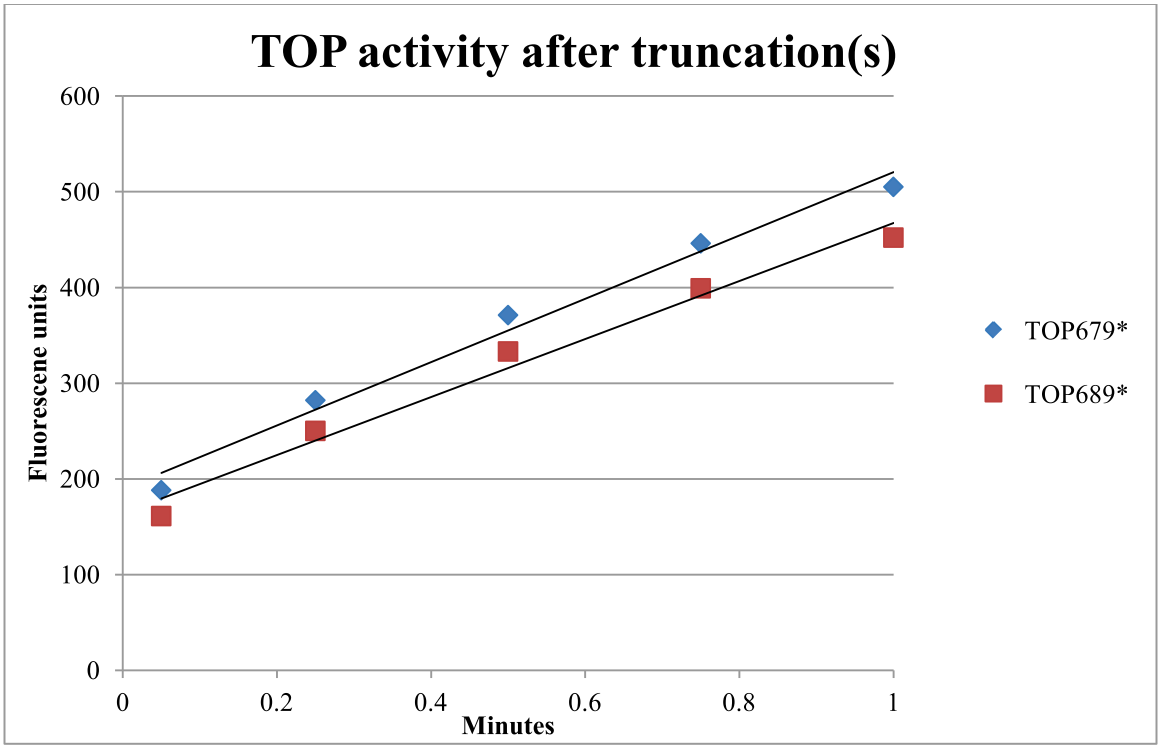

**Figure 3.3 Activity of truncated constructs.** Dual truncated TOP (blue) activity is comparable to N truncated TOP (red). The assay was carried out using a quenched fluorogenic neurotensin substrate and following the increase in fluorescence generated by substrate cleavage over time.

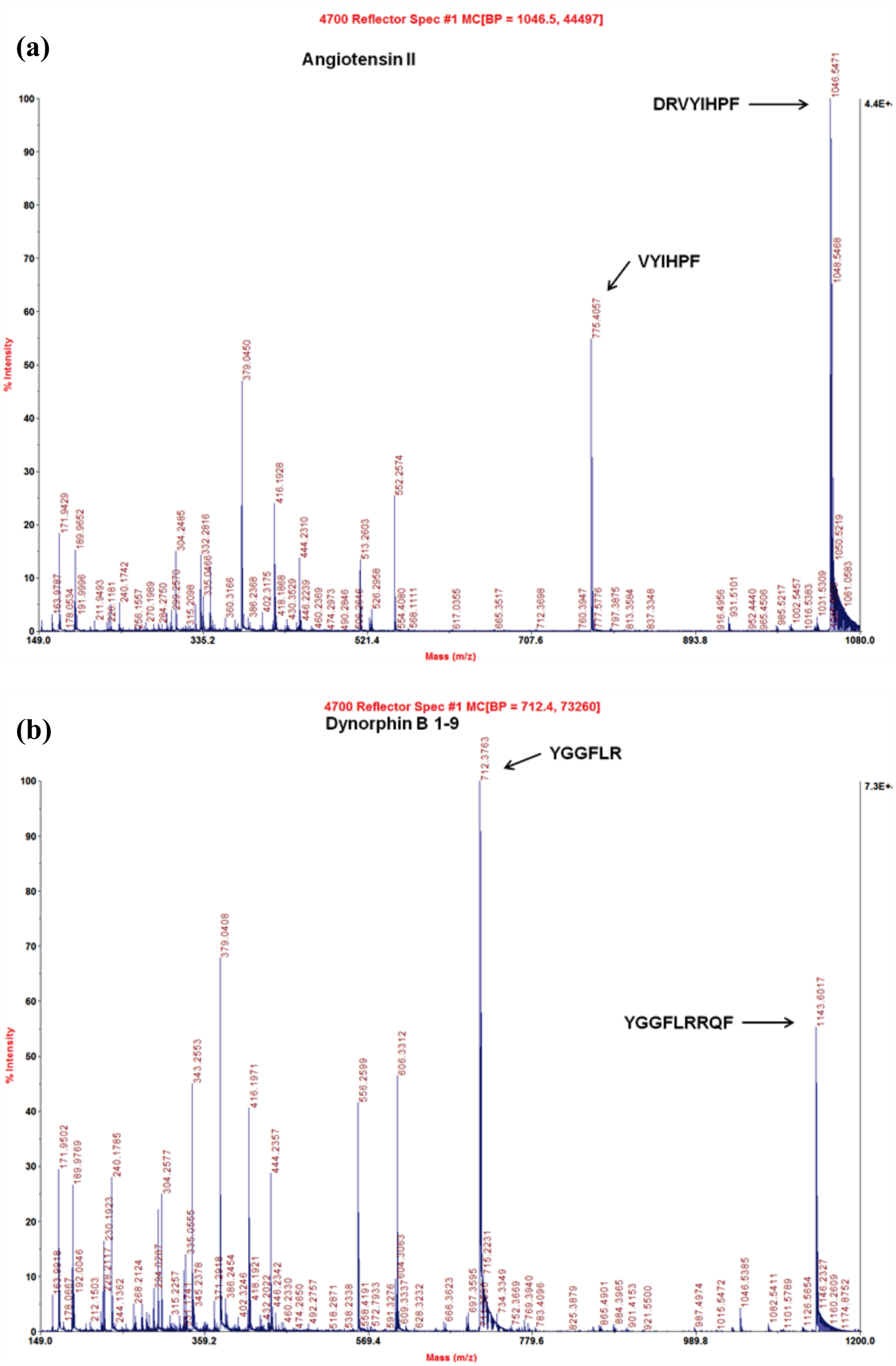

**Figure 3.4 Previously unreported cleavage sites. a)** Mass spectrum of angiotensin II fragments indicating cleavage at the R-V bond **b)** Mass spectrum of dynorphin B(1-9) indicating cleavage at the R-R bond. Samples were measured after 1hr incubation with active N truncated TOP.

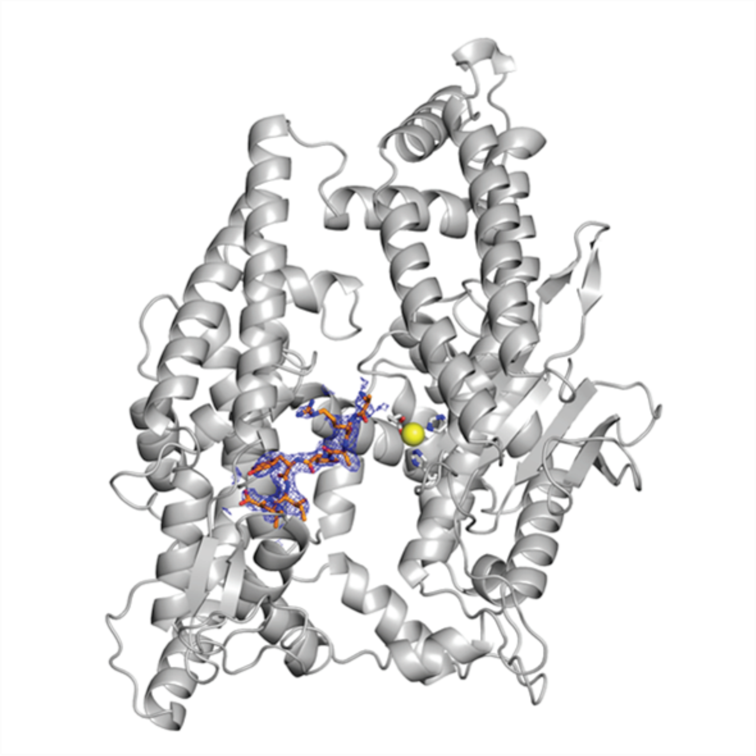

**Figure 3.5 Example of a substrate bound to TOP.** TOP is shown as gray cartoon with the HEXXH motif and Zn cofactor highlighted. Neurotensin is shown as orange sticks surrounded by its corresponding 2Fo - Fc density map. Density is displayed at 1σ.

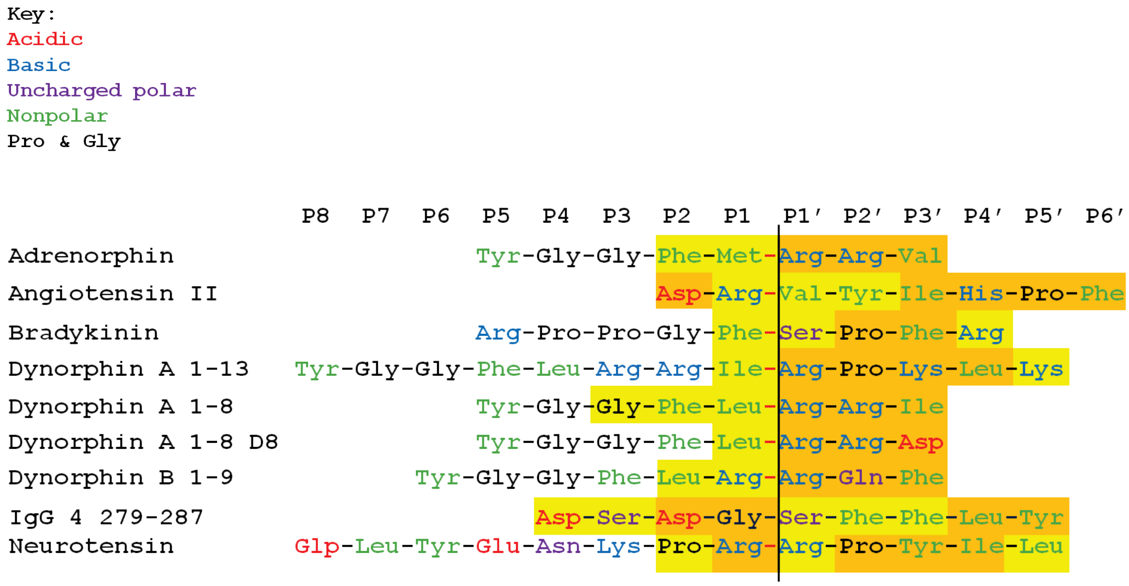

**Figure 3.6 Complexes that formed with domain I.** Orange background indicates residues with clear side chain density while yellow represents sequences with only backbone visible. Red dashes indicate reported TOP cleavage sites. Sequences have been aligned based on the bond cleaved by TOP.

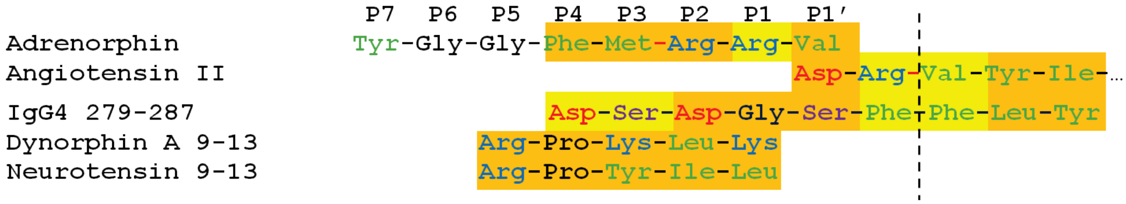

**Figure 3.7 Complexes that formed with domain II.** Orange background represents residues with clear side chain density while yellow represents sequences with only backbone visible. Red dashes indicate reported TOP cleavage sites. The dashed line indicates where substrates span the interdomain cleft.

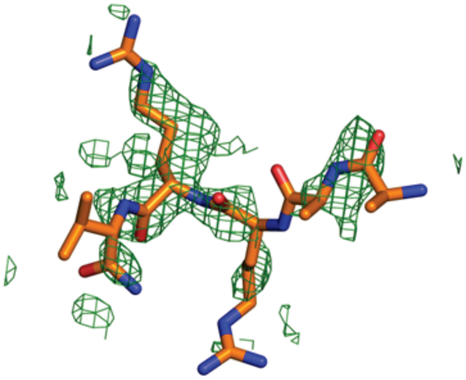

**(a)** adrenorphin

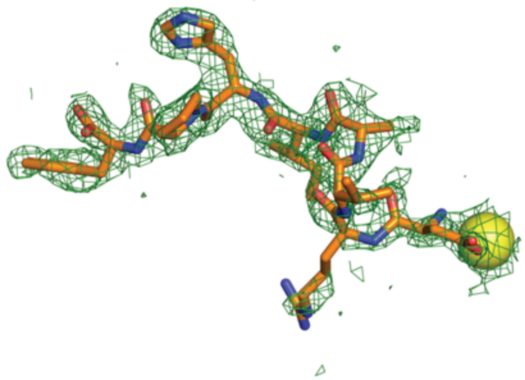

**(b)** angiotensin II

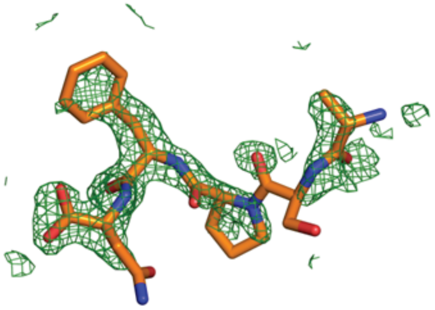

**(c)** bradykinin

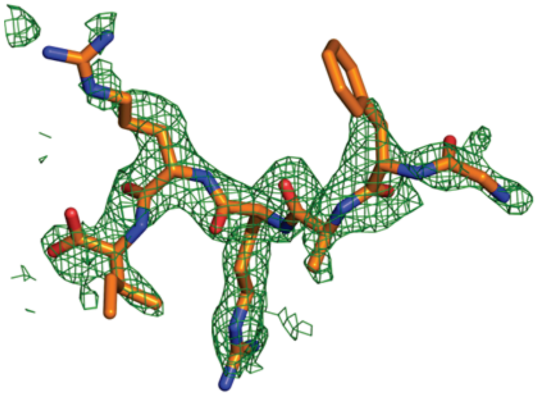

**(d)** dynorphin A(1-8)

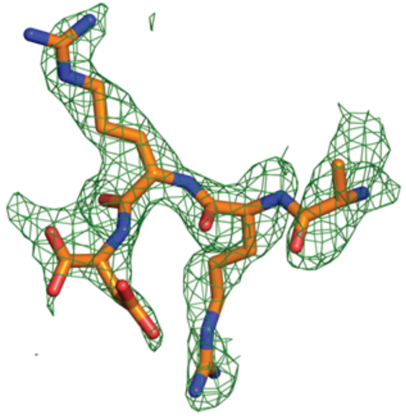

**(e)** dynorphin A(1-8) D8

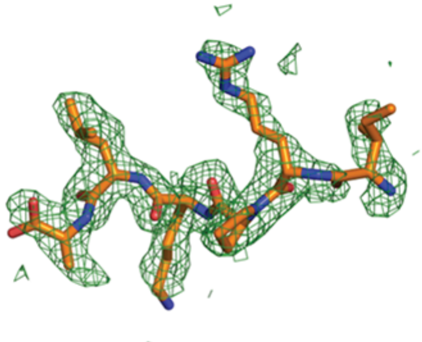

**(f)** dynorphin A(1-13)

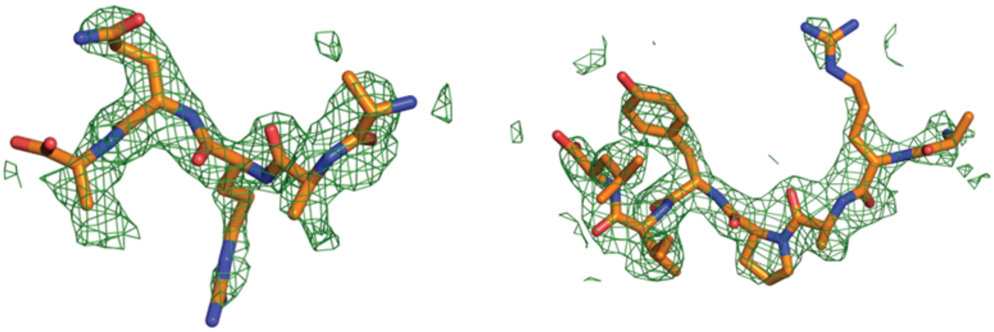

**(g)** dynorphin B(1-9) **(h)** neurotensin

**Figure 3.8 FoFc maps from N truncated TOP complexes.** Final refined models shown in stick representation are superposed onto FoFc difference maps generated from initial rigid body refinement with the empty protein model. FoFc density maps are displayed at 2σ cutoff level.

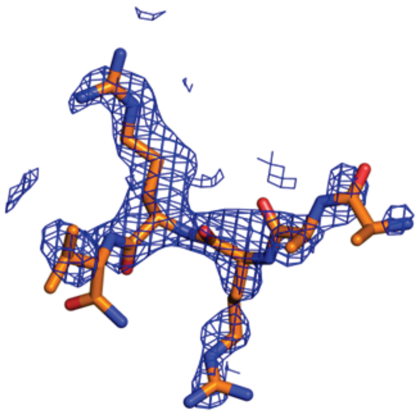

**(a)** adrenorphin

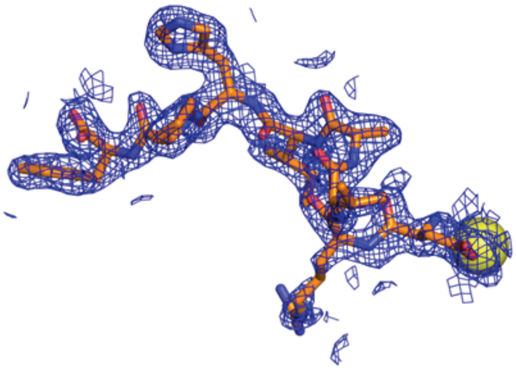

**(b)** angiotensin II

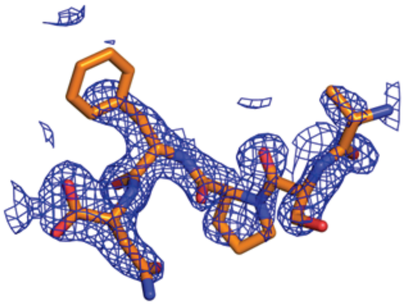

**(c)** bradykinin

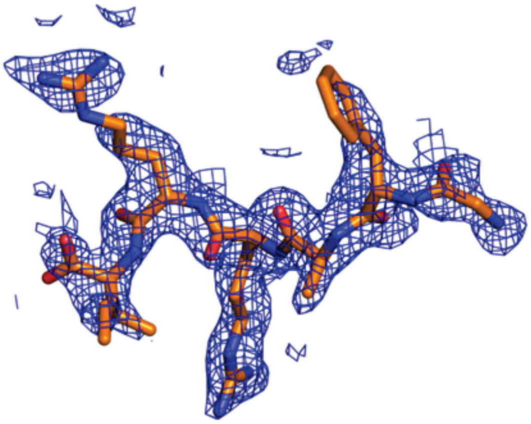

**(d)** dynorphin A(1-8)

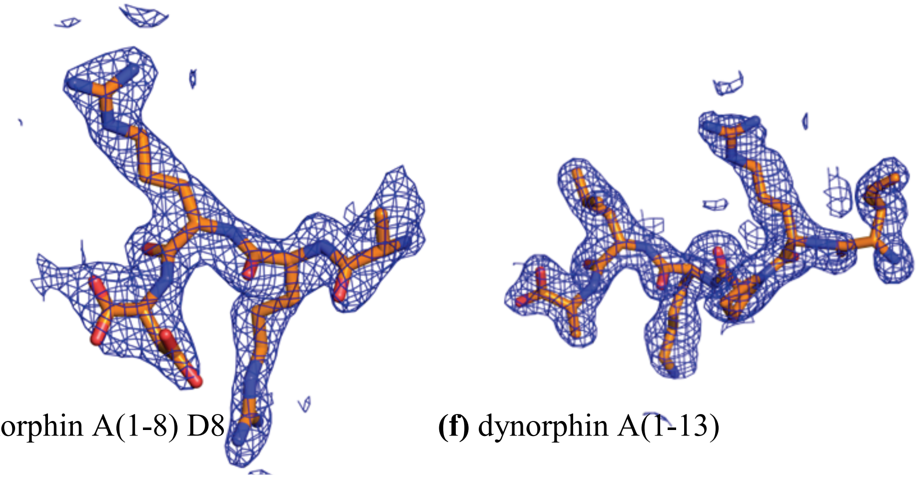

**(e)** dynorphin A(1-8) D8 **(f)** dynorphin A(1-13)

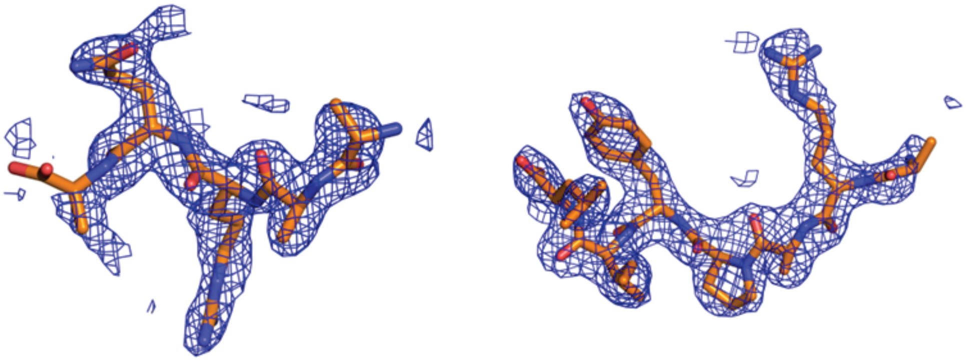

**(g)** dynorphin B(1-9) **(h)** neurotensin

**Figure 3.9 2FoFc maps of N truncated TOP complexes.** 2FoFc maps from N truncated TOP complexes are displayed at 1σ. Final refined models are shown in stick representation. The maps were generated after refinement was complete.

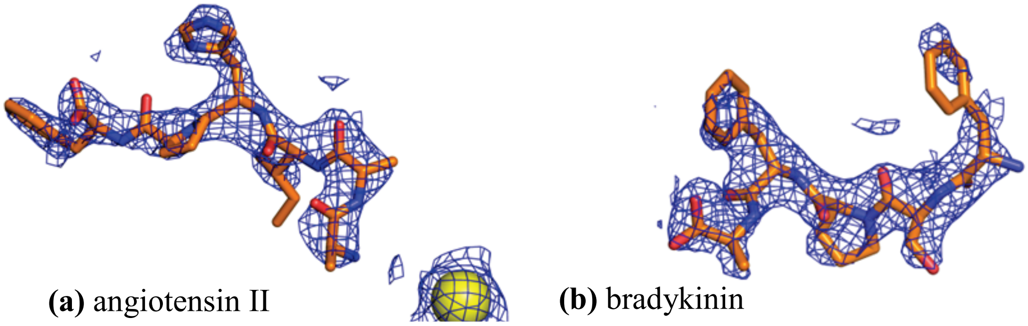

**(a)** angiotensin II **(b)** bradykinin

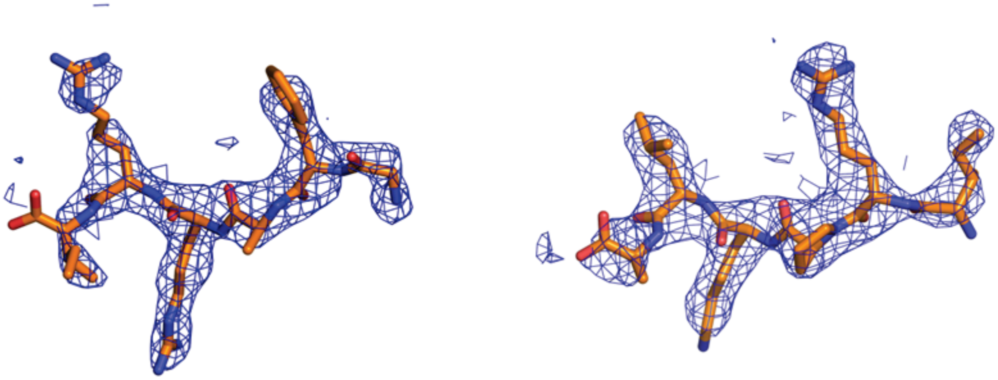

**(c)** dynorphin A(1-8) **(d)** dynorphin A(1-13)

**Figure 3.10 Dual truncated TOP ligand maps.** Substrates are represented as orange sticks. 2fofc densities of substrates displayed at 1 sigma. These are final refined models. Note: models were left incomplete at the point where density became unreliable.

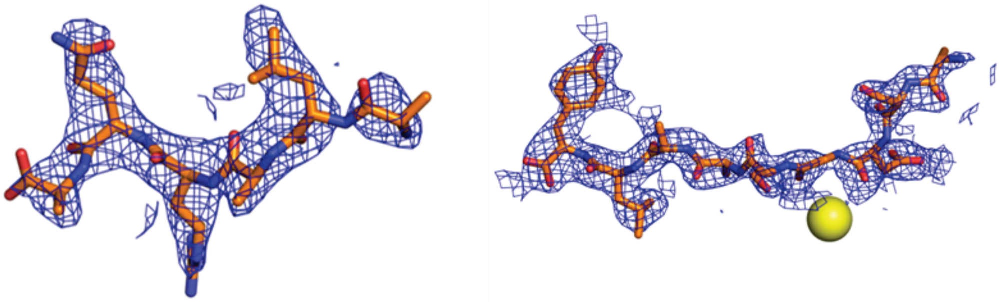

**(e)** dynorphin B(1-9)

**(f)** Immunoglobulin G4 (279-287)

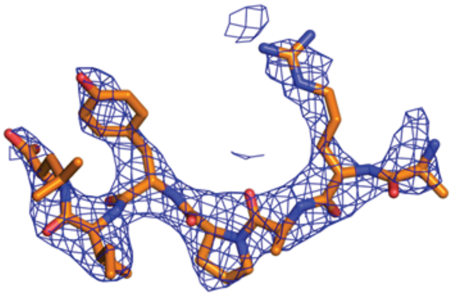

**(g)** neurotensin

**Figure 3.10 continued.** Substrates are represented as orange sticks. 2FoFc densities of substrates displayed at 1 sigma. These are final refined models. Note: models were left incomplete at the point where density became unreliable.

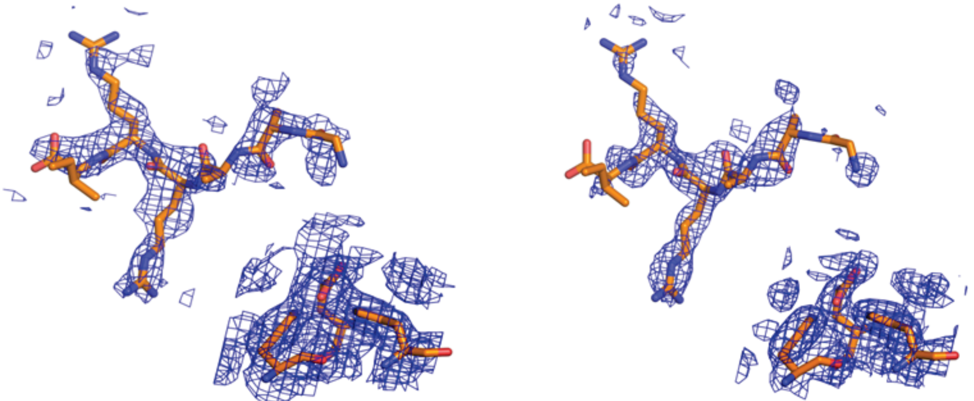

dynorphin A(1-8) dynorphin A(1-8) no Zn

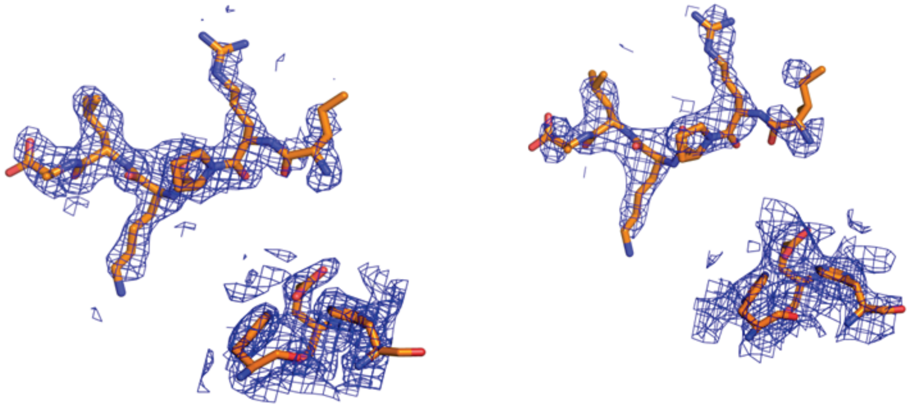

dynorphin A(1-13) dynorphin A(1-13) no Zn

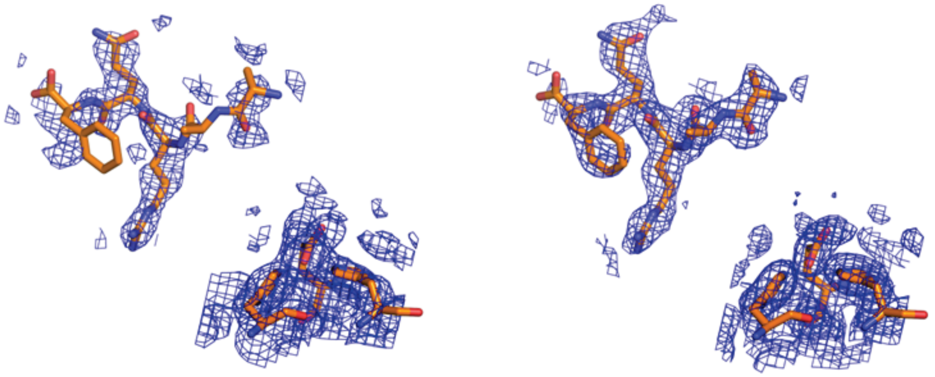

dynorphin B(1-9) dynorphin B(1-9) no Zn

**Figure 3.11 Apoenzyme controls.** TOP N15_C2S_E474A/C427S structures were refined with a Zn ion in the model. The resulting 2FoFc density of refined structures is displayed at 1 sigma. Left panel: no Zn ion removal. Right panel: Zn ion removal.

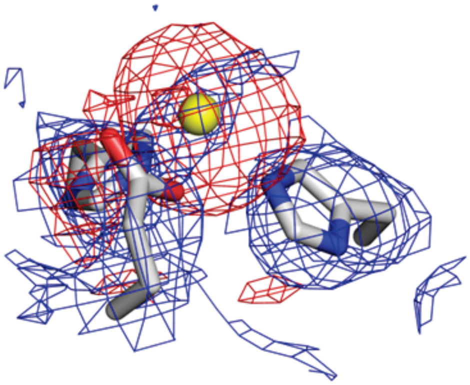

**Figure 3.12 Fast Zn removal with LHRH + EDTA.** Electron density after initial rigid body refinement with a Zn ion (yellow sphere) included in model. Blue = 2fofc density at 1.0 sigma, red = fofc density at -2.0 sigma

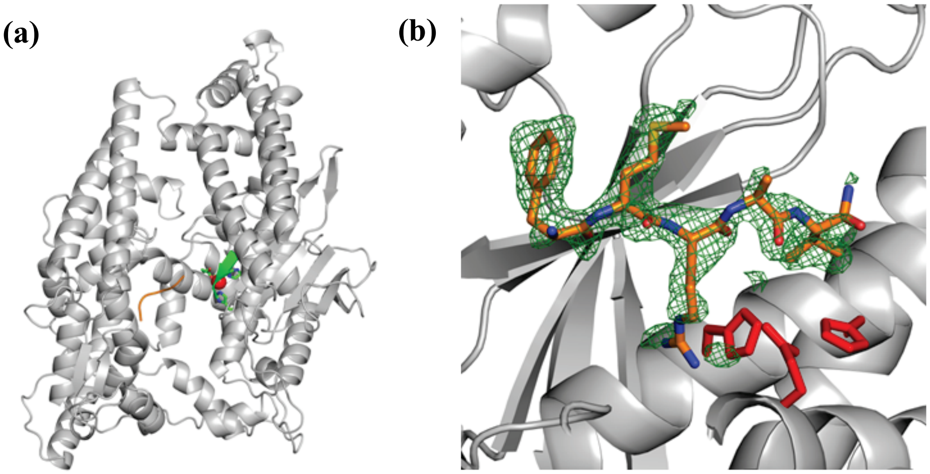

**Figure 3.13 Additional adrenorphin binding site after Zn removal. a)** Two adrenorphins bind, one on each domain. **b)** Domain II density is clearly seen lying along the beta sheet and the substrate sequence FMRRV can be modeled with the (amidated) C-terminal lying where the Zn would have been. His477 is disturbed and the Zn is gone from the active site. The C-terminal valine takes advantage of the hydrophobic surface created by the E474A mutation.

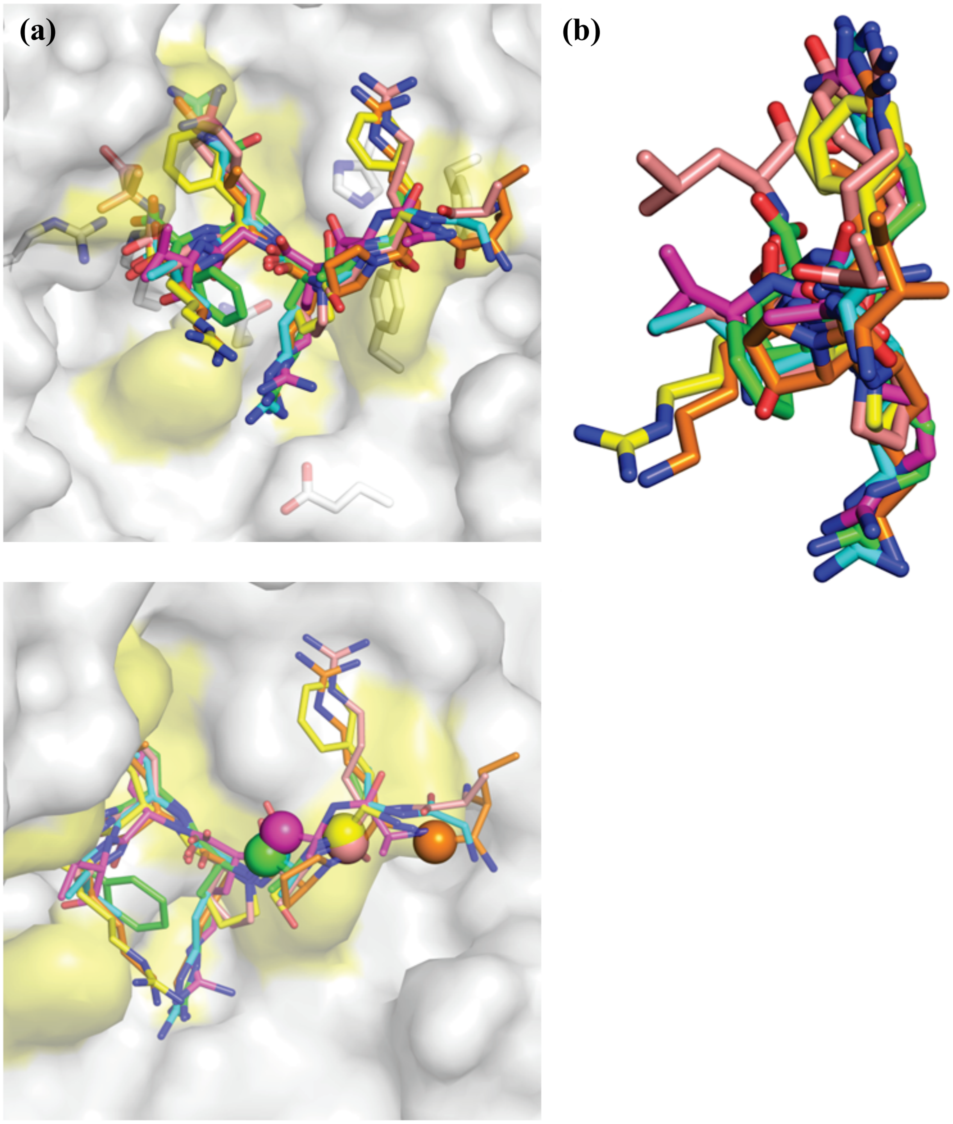

**Figure 3.14  Superposition of standard substrate complexes.** Domain I binding substrate complexes excluding angiotensin II, immunoglobulin 4, and fragment complexes are superposed on one another. **a)** Fully refined substrate models are show in stick representation. Enzyme surface taken from dynorphin A(1-13) complex's surface. Important polar surface residues also shown in sticks. Yellow surface indicates important hydrophobic or aromatic surfaces. dynorphin A(1-13) = orange, adrenorphin = dark pink, bradykinin = yellow, dynorphin A(1-8) = cyan, neurotensin = pink, dynorphin B(1-9) = green **b)** view looking down the mainchain axis of superposed substrates. TOP's flat binding surface on the right prevents side chain insertion. **c)** same as (a) but with beta carbons of cleaved bonds emphasized as spheres.

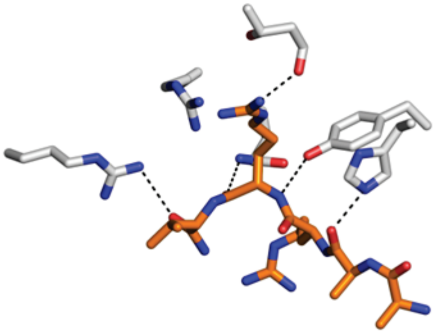

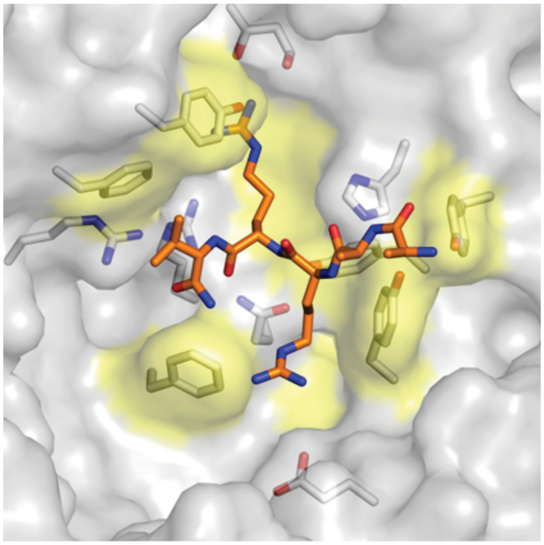

**(a)** adrenorphin

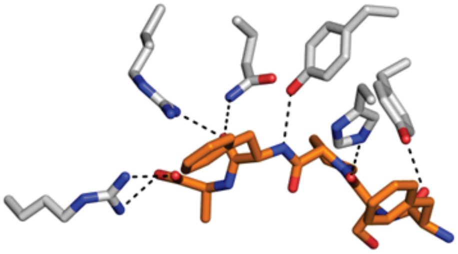

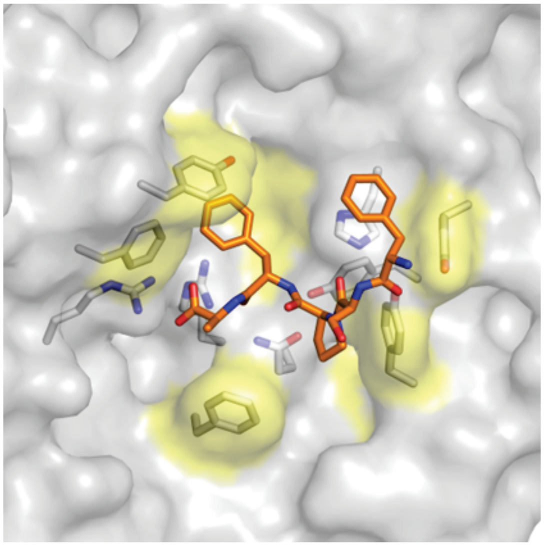

**(b)** bradykinin

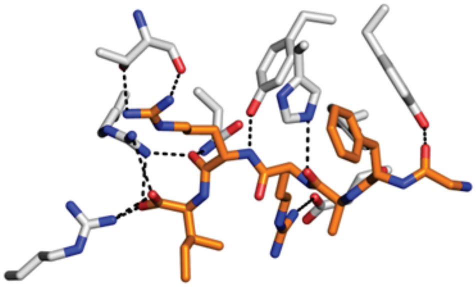

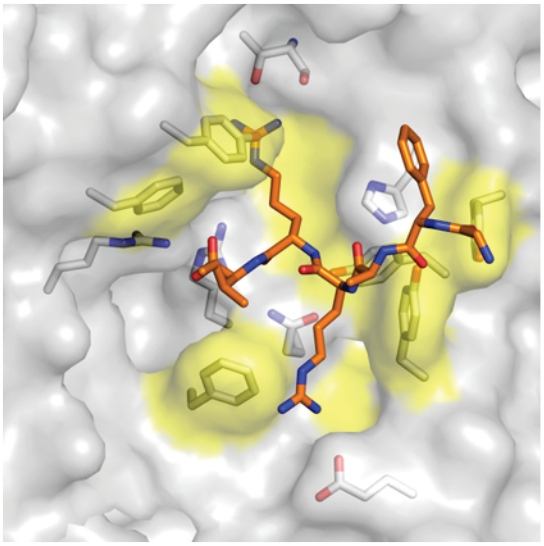

**(c)** dynorphin A(1-8)

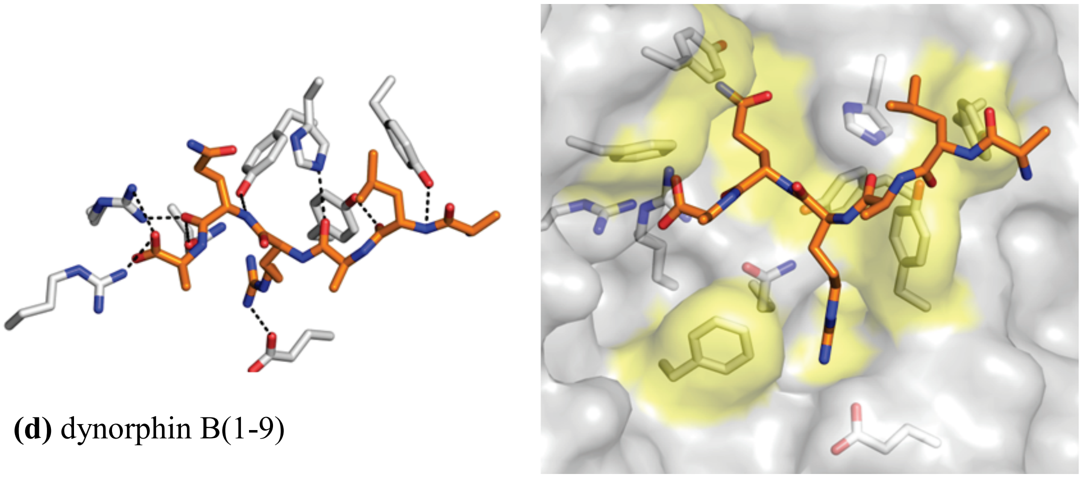

**(d)** dynorphin B(1-9)

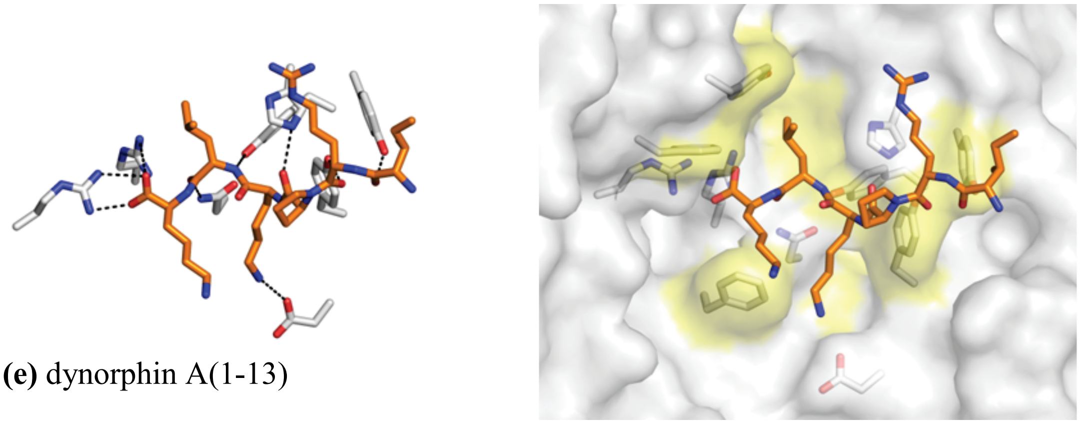

**(e)** dynorphin A(1-13)

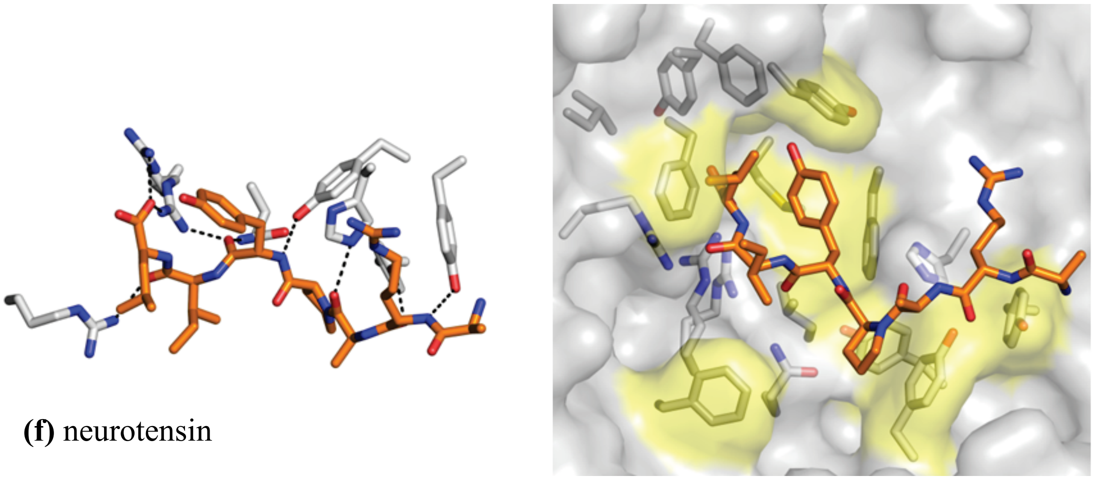

**(f)** neurotensin

**Figure 3.15 Binding site interactions for standard substrate complexes.** Substrate groups that could be placed in the structures are shown as orange sticks while TOP residues are white sticks. Left panel: hydrogen bonds and ionic interactions are shown as dashed lines. Right panel: TOP binding surface is shown with hydrophobic/aromatic residues in yellow and interacting residues as sticks within the surface.

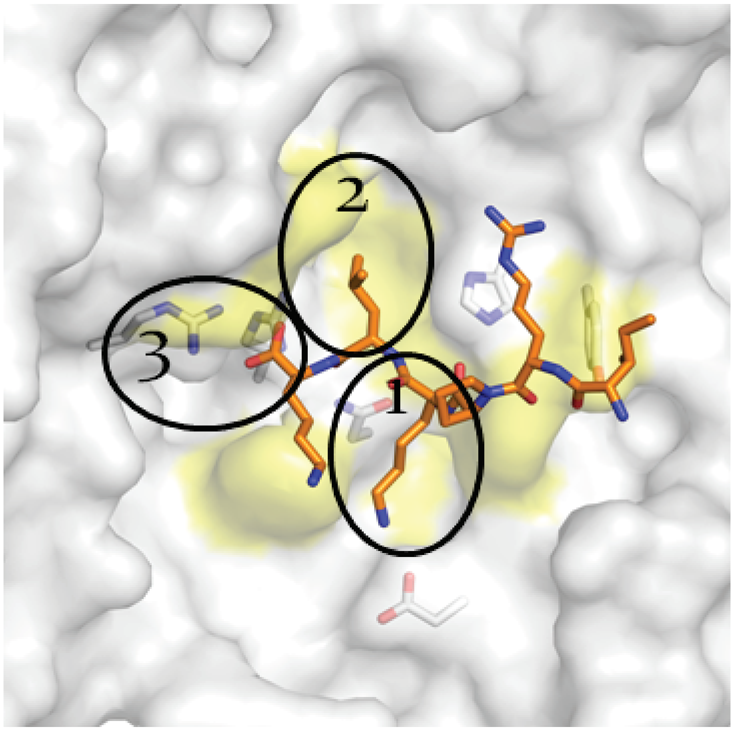

**Figure 3.16  Binding site subsites.** Dynorphin A(1-13) substrate in a stick representation. The surface of TOP is colored yellow to indicate hydrophobic / aromatic surfaces. Arg338, Arg553, Gln554, His600, Tyr605, and Glu616 side chains are modeled as sticks within the surface. The locations of subsites 1, 2, and 3 are indicted by numbered circles.

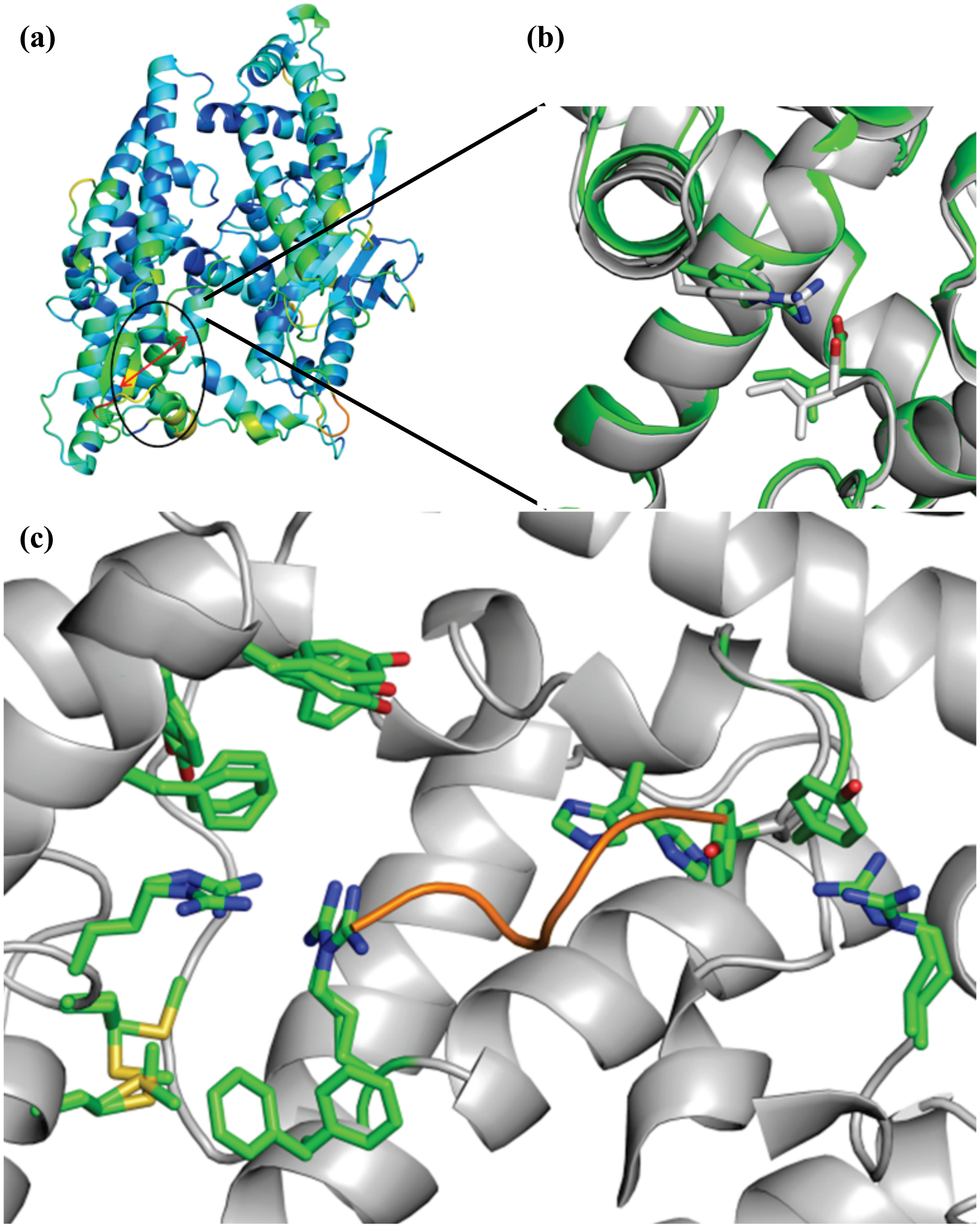

**Figure 3.17 Domain I substrate binding site and conformational shifts. a)** Ribbons view of TOP colored by crystallography thermal factor (yellow = high, blue = low). The oval indicates the helices 7,8,12 region that shows higher than average disorder. The expanded view shows two superposed N-truncated TOP - dynorphin A(1-8) complex structures from two different crystallizations illustrating variation in the region that interacts with the substrate C-terminus. **b)** All significant side chain conformational differences seen in any structure superposed into the structure of the dynorphin A(1-13) complex. dynorphin A = orange ribbon, TOP = grey ribbon, moving side chains = green sticks.

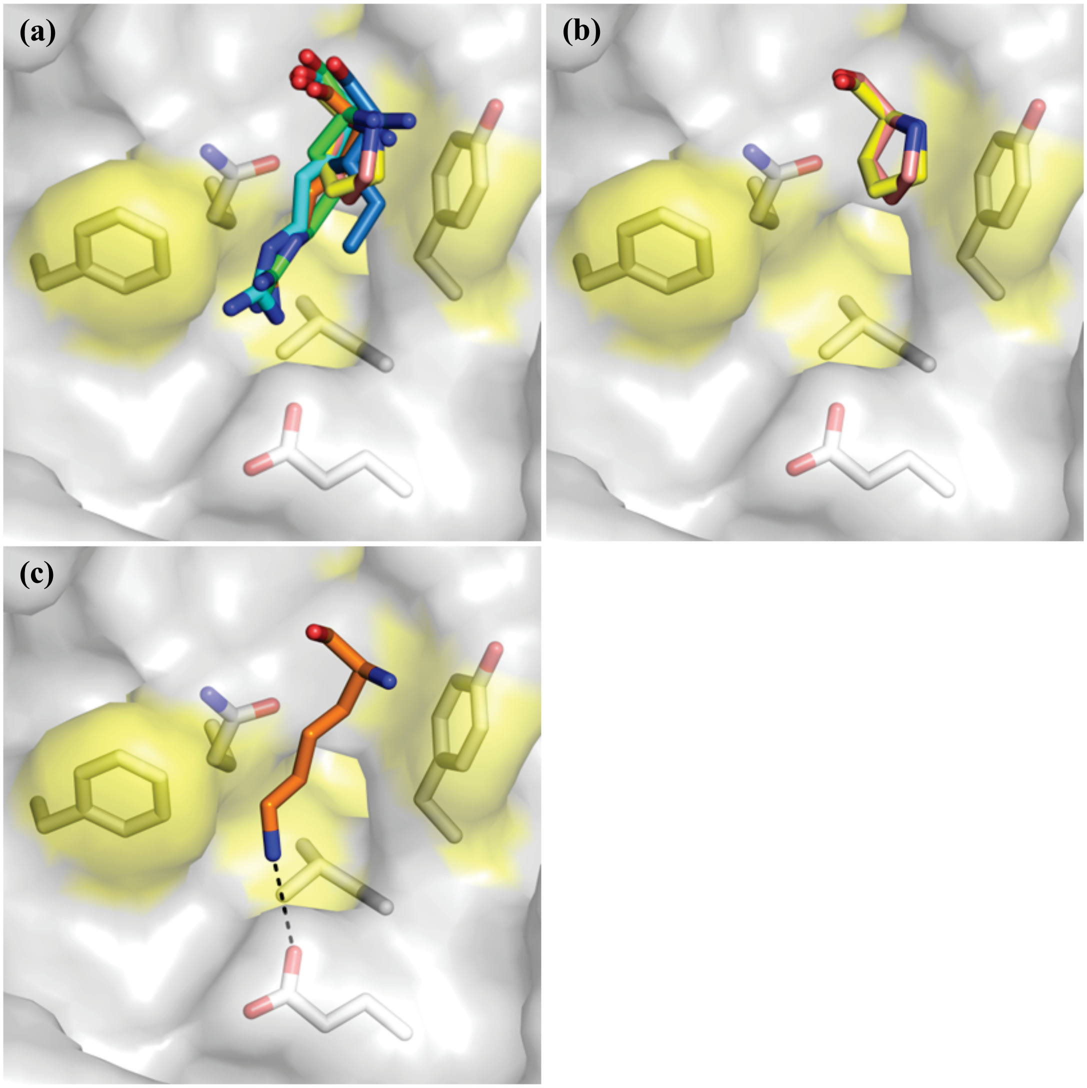

**Figure 3.18 Subsite 1.** Side chains of TOP residues F550, Q554, L613, Y612, E616 are shown in a stick representation. The molecular surface is shown with aromatic or hydrophobic portions colored yellow. **a)** Residues from different substrates occupying subsite 1 shown in a stick representation **b)** Proline residues neurotensin and bradykinin in subsite 1 **c)** Lysine residue from bound dynorphin A(1-13) demonstrating the salt bridge to E616. Other dynorphin-like sequences also make a similar interaction.

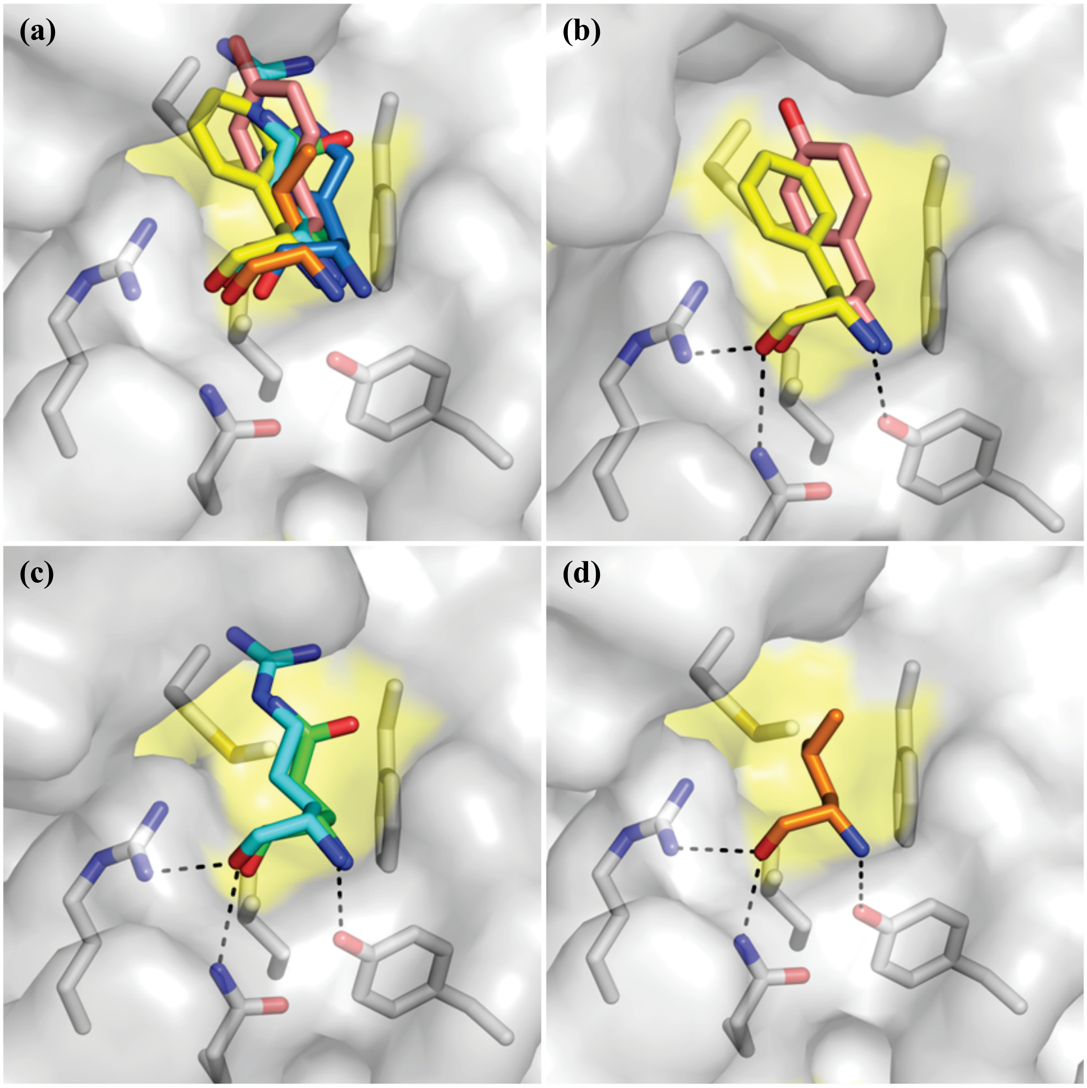

**Figure 3.19 Subsite 2.** Side chains of TOP residues R553, Q554, M594, L557, F598, and Y609 are shown in a stick representation. A semitransparent view of the molecular surface is shown with aromatic and hydrophobic regions indicated in yellow. **a)** Residues occupying subsite 2 from the standard binding orientation complex structures. **b)** Aromatic residues from neurotensin and bradykinin. **c)** Longer charged and polar residues from dynorphin B 1-9 and dynorphin A 1-8. **d)** Hydrophobic leucine from dynorphin A(1-13). All substrate residues at this subsite participate in a hydrogen bond network via backbone interactions (dotted lines).

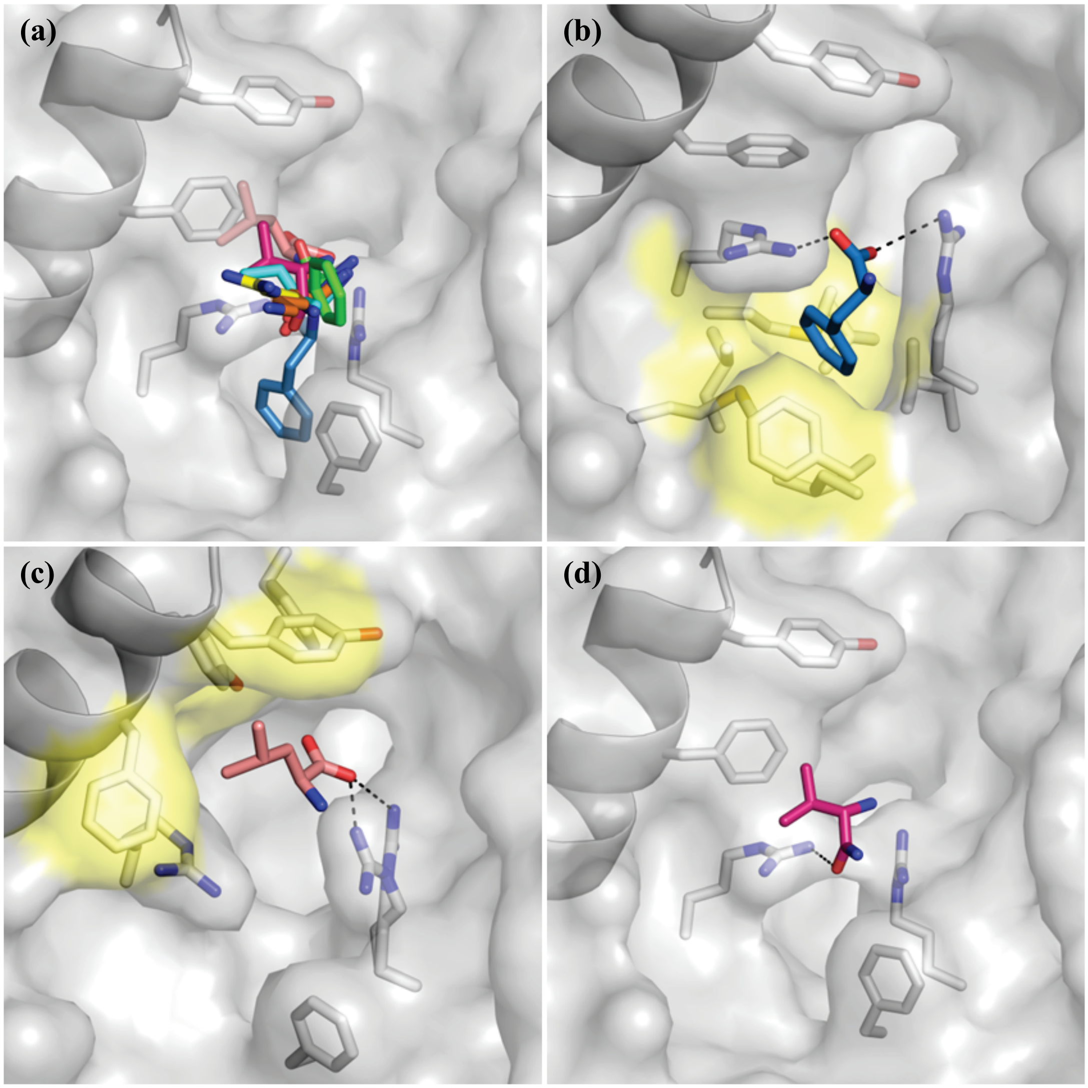

**Figure 3.20  Subsite 3.** Side chains of TOP residues R338, R553, F225, Y221, and F550 are shown in a stick representation.  A semitransparent view of the molecular surface is shown with aromatic and hydrophobic regions indicated in yellow.  Aromatic or hydrophobic surfaces are colored yellow.  **a)** Residues occupying subsite 3 from the standard binding orientation complex structures.  **b)** Angiotensin II binding reorganizes subsite 3 with nearly the entire side chain accessible surface of F8 buried in the interaction.  **c)** The C-terminal residue of neurotensin extends into a different portion of subsite 3.  **d)** The amidated valine of adrenorphin interacts with F225 slightly displacing it and Y221.

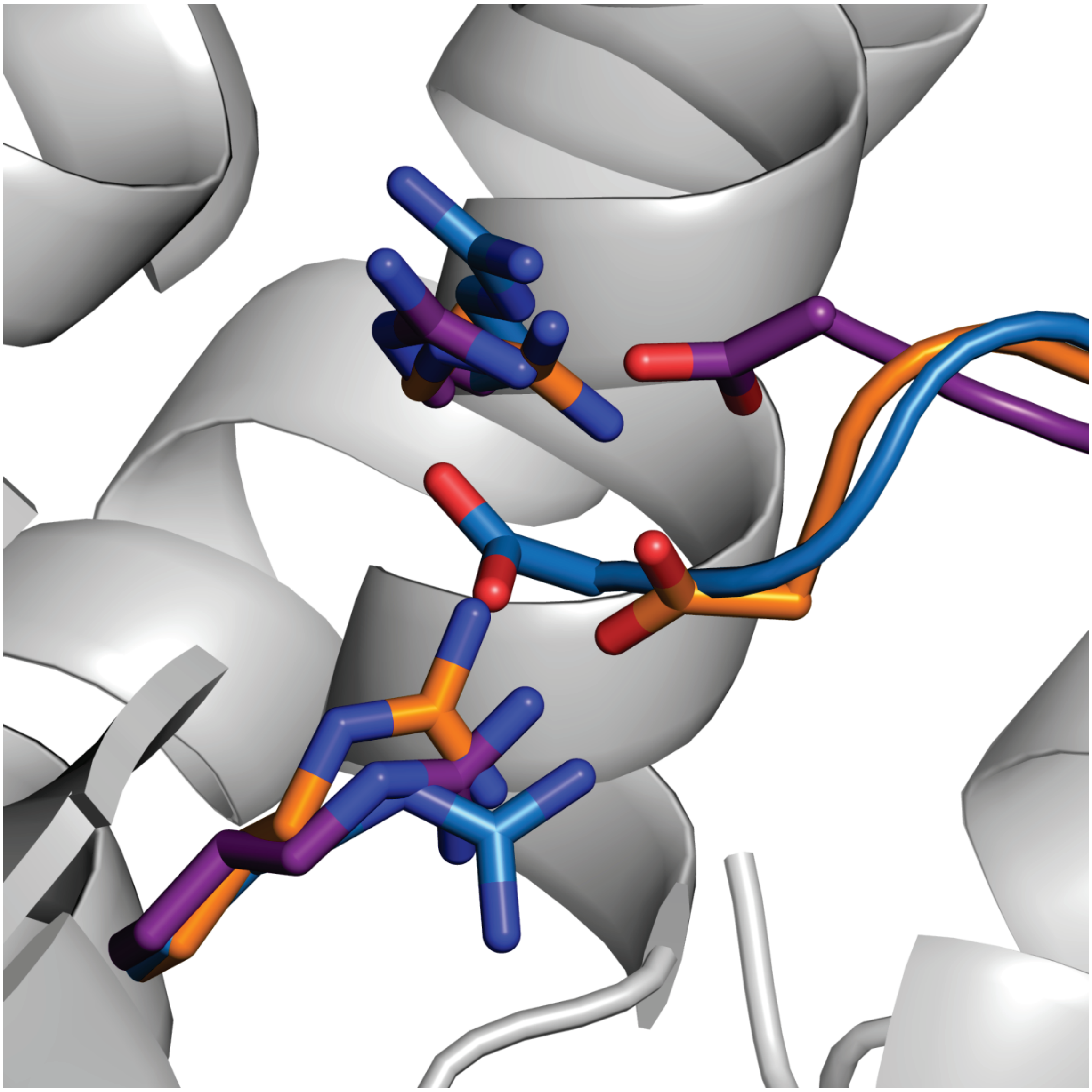

**Figure 3.21 Interaction of peptide C-termini with TOP.** TOP motif that interacts with the C-termini of bound substrate peptides consists of arginines 338 and 553. Dynorphin A(1-8) = orange, angiotensin II = blue, IgG4 = purple

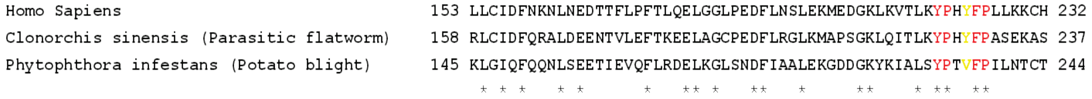

```
Homo Sapiens                                153 LLCIDFNKNLNEDTTFLPFTLQELGGLPEDFLNSLEKMEDGKLKVTLKYPHYFPLLKKCH 232
Clonorchis sinensis (Parasitic flatworm)    158 RLCIDFQRALDEENTVLEFTKEELAGCPEDFLRGLKMAPSGKLQITLKYPHYFPASEKAS 237
Phytophthora infestans (Potato blight)      145 KLGIQFQQNLSEETIEVQFLRDELKGLSNDFIAALEKGDDGKYKIALSYPTVFPILNTCT 244
                                                 * * *   * *      *   ** *   **   *     **    * **  **
```

**Figure 3.22 Conserved residues around subsite 3.** an * indicates positions of conserved residues. Those in the helix forming subsite 3 just above TOP's C-terminal recognition motif are highlighted in red (completely conserved) and yellow (conserved in type).

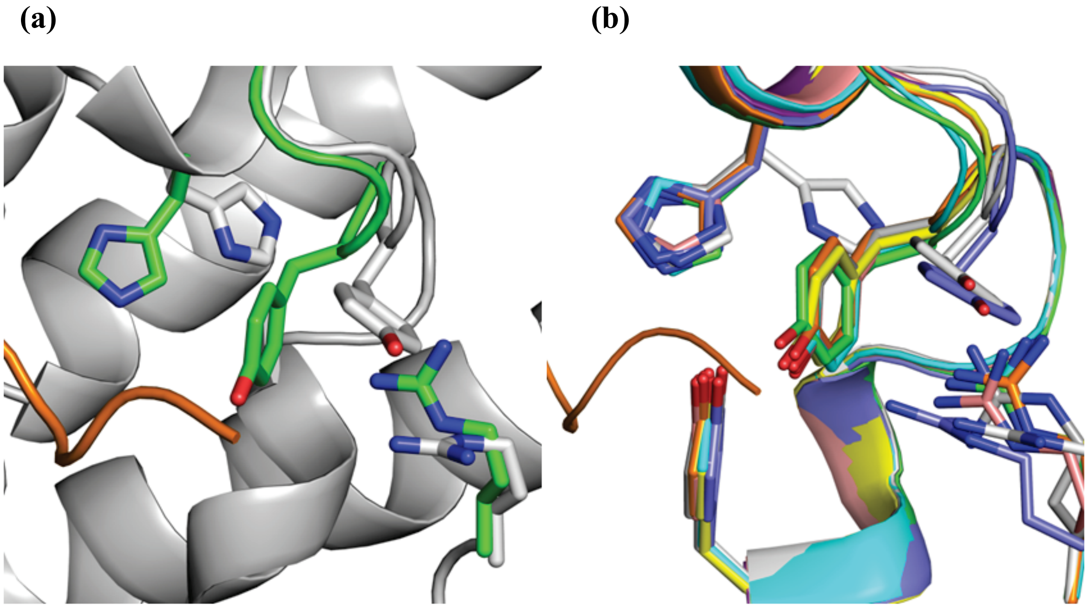

**Figure 3.23 Binding site rearrangement upon ligand binding. a)** Differences in the 599-611 loop of dual truncated TOP before (white) and after (green) binding dynorphin A(1-13). His600, Gly603-Tyr605, and Arg498 are shown in stick representation, dynorphin A 1-13 shown as cartoon (orange) **b)** residues 498, 599-612 superposed for all substrate complexes with dual truncated TOP. His600, Tyr605, Arg498 are shown in a stick representation while the remainder of 599-611 loop is cartoon. Unliganded TOP = white, dynorphin A(1-13) = orange, adrenorphin = purple, angiotensin II = dark blue, bradykinin = yellow, dynorphin A(1-8) = cyan, neurotensin = pink, dynorphin B(1-9) = green

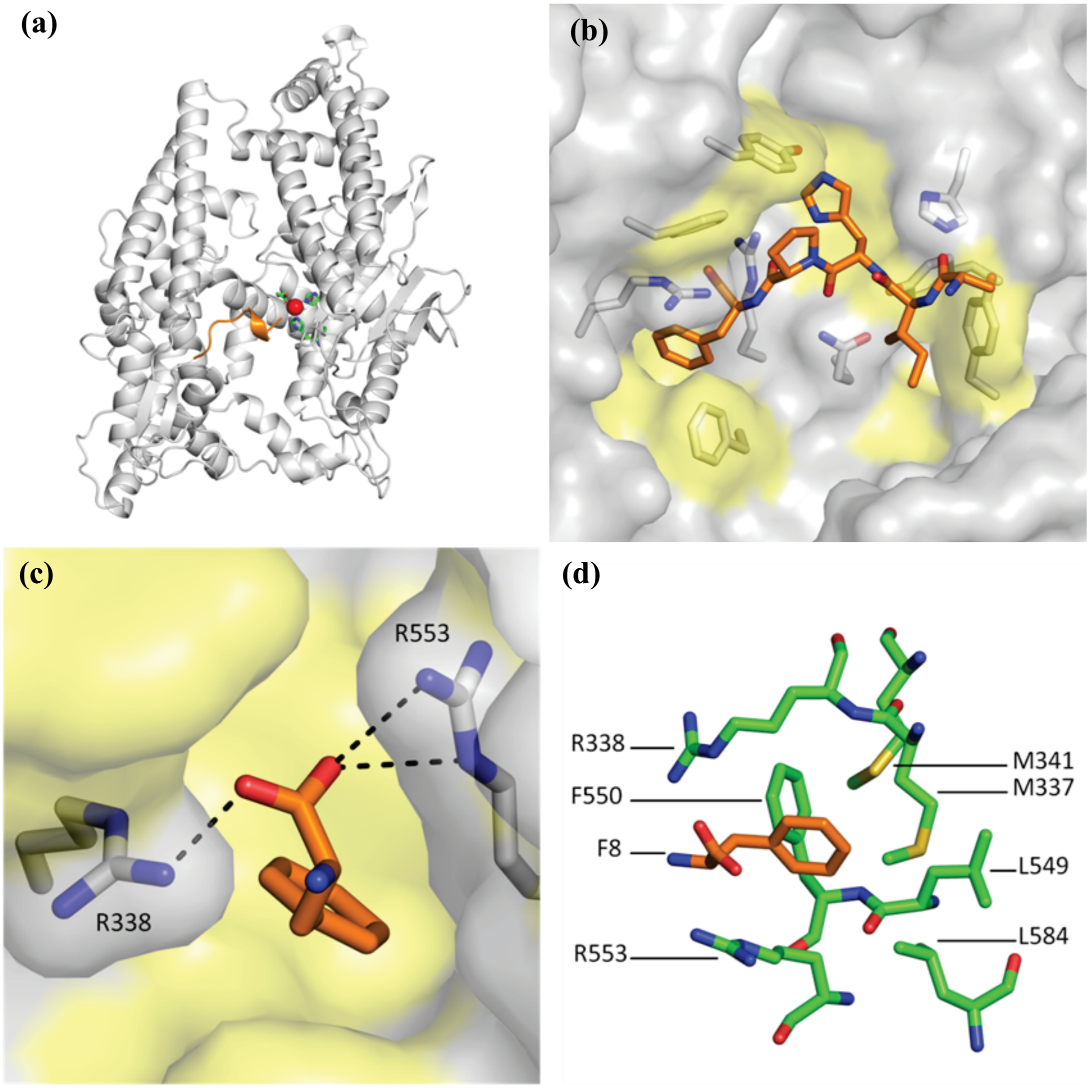
(a)
(b)
(c)
R553
R338
(d)
R338
M341
F550
M337
F8
L549
R553
L584

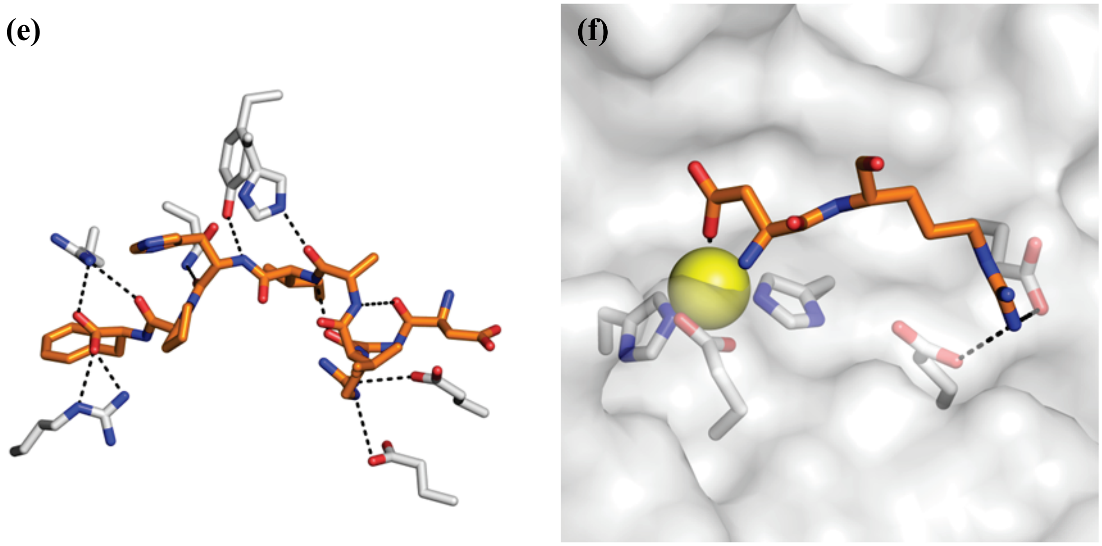

**Figure 3.24 TOP / angiotensin II complex. a)** Overview with angiotensin II (orange ribbon) and TOP (grey ribbon). **b)** Angiotensin II (orange) binding to the domain I binding site. Hydrophobic surfaces are colored yellow and relevant TOP side chains are shown as sticks behind the surface. **c)** Subsite 3 interaction. Hydrophobic / aromatic surfaces are colored yellow and dashes indicate ionic interactions. **d)** TOP residues that compose subsite 3 shown in a stick representation with green carbon bonds. The C-terminal phenylalanine of the bound peptide is also shown in a stick representation. **e)** Polar interactions with angiotensin 2. Dashed lines indicate atoms that are within hydrogen bonding distance (<3.5A) or within range for charge-charge attraction (<4.0A) **f)** Interactions formed between the N-terminal residues of angiotensin II and TOP including Zn ion coordination.

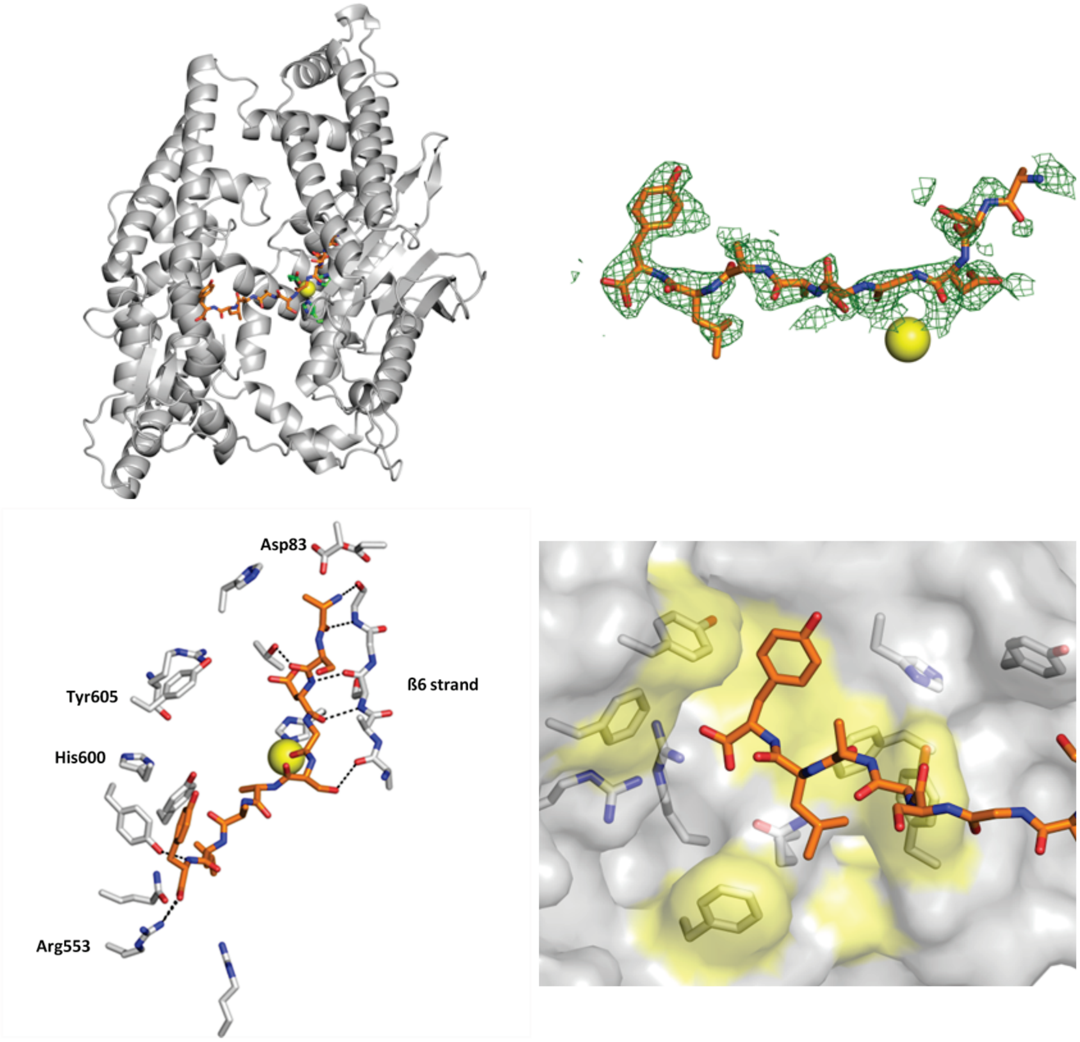

**Figure 3.25 TOP / IgG4 complex. a)** Overview with IgG4 (orange sticks) and TOP (gray ribbons). **b)** IgG4 (orange sticks) with FoFc density displayed at $2\sigma$. Zn ion is displayed as yellow sphere. **c)** Overview of IgG4 (orange sticks) crossing the interdomain cleft. Relevant TOP side chains are displayed as white sticks and ionic or hydrogen bonds are indicated with dashed lines. Side chains often participating in conformational changes are explicitly labeled. **d)** IgG4 (orange) binding to the domain I binding site. Hydrophobic surfaces are colored yellow and relevant TOP side chains are shown as sticks behind the surface.

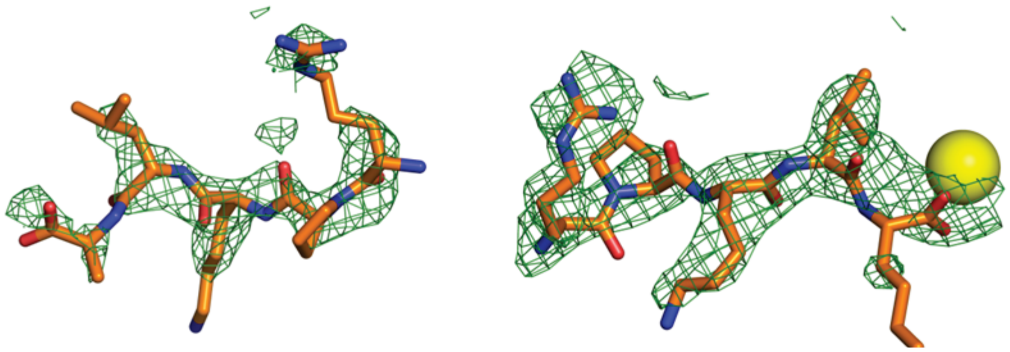

**(a)** dynorphin A(9-13) domain I **(b)** dynorphin A(9-13) domain II

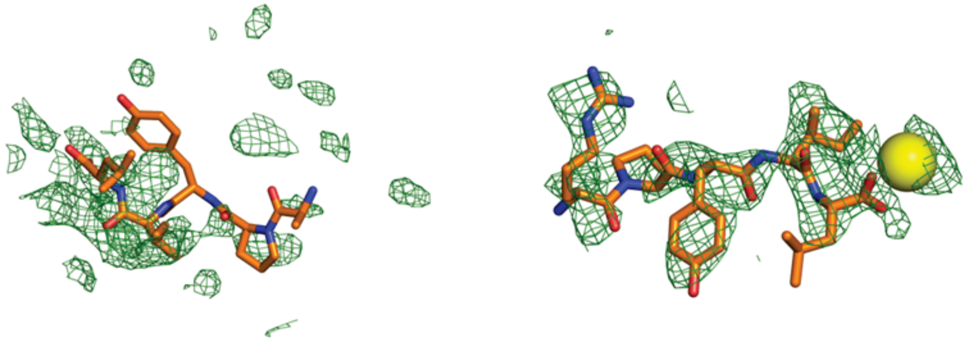

**(c)** neurotensin(9-13) domain I* **(d)** neurotensin(9-13) domain II

**Figure 3.26 FoFc density of domain II ligands.** Difference electron density for ligands of the dynorphin A(9-13)-TOP and neurotensin(9-13)-TOP structures. FoFc density at 2.0 sigma is displayed after initial rigid body replacement. Bound peptides are show as orange sticks. Zn is shown as a yellow sphere.

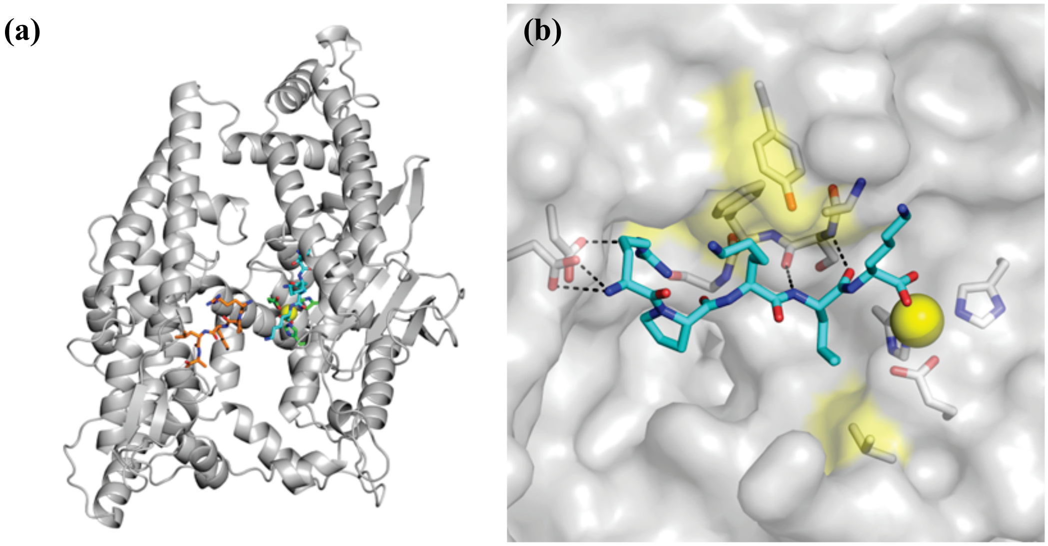

**Figure 3.27 The dynorphin A(9-13)-TOP structure. a)** Overview of bound peptides. Dynorphin A(9-13) binds to the domain I surface, interacting in the same manner the C-terminal residues of dynorphin A(1-13). A second molecule of the peptide binds to domain II. **b)** Interactions with the domain II binding site. Aromatic/hydrophobic surfaces are colored yellow and dashed lines indicate hydrogen bonds. Coordination of the active site Zn ion aids in binding. orange sticks = dynorphin A(9-13) domain I, blue sticks = dynorphin A(9-13) domain II.

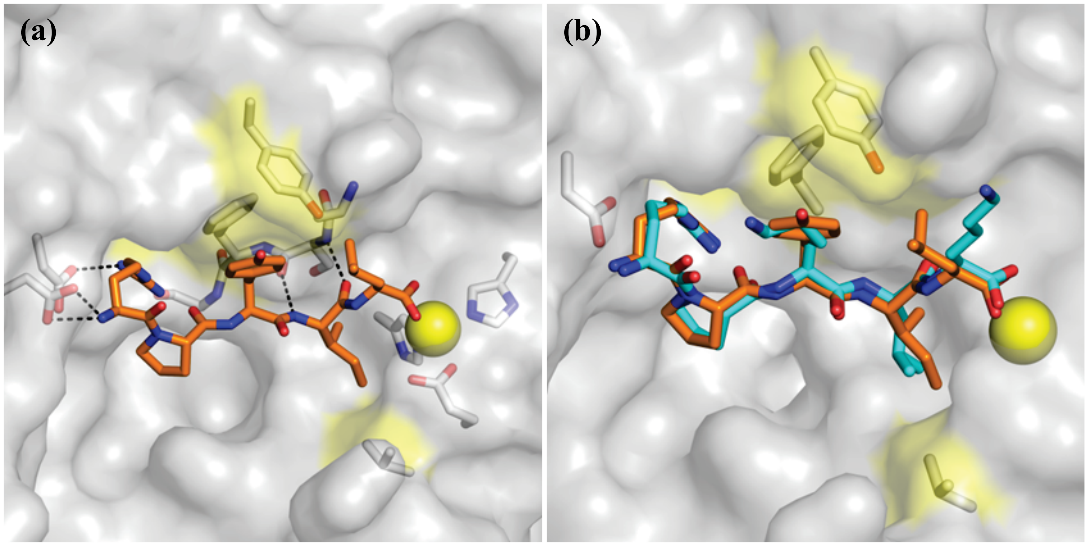

**Figure 3.28 Neurotensin (9-13). a)** Binding to across the TOP channel. The peptide is shown in a stick representation and aromatic/hydrophobic portions of the enzyme surface are in yellow. The zinc ion is shown as a yellow sphere. **b)** Comparison with dynorphin A(9-13) binding. Superimposed peptides structures are shown in a stick representation. The C-terminal product fragment neurotensin (9-13) binds to domain II similar to dynorphin A(9-13). orange = neurotensin (9-13), blue = dynorphin A(9-13)

# CHAPTER FOUR: Thermodynamics of TOP binding

Much of the work done to determine the dissociation constant and catalytic efficiency of TOP has used quenched fluorescent substrates. While these substrates may mimic the corresponding native substrate peptide in most cases, there is always a possibility that the bulky fluorescent moieties may disrupt normal binding. In order to more accurately determine binding constants as well to more completely characterize the energetics of peptide binding to TOP, I used isothermal titration calorimetry (ITC) to investigate substrate binding. Here I report thermodynamic data for a number of substrate-TOP interactions performed in Tris buffer that are useful for calculating binding constants as well as an in-depth thermodynamic analysis of the TOP-dynorphin A(1-13) interaction.

With ITC the enthalpic and entropic contributions to binding energetics can be estimated; however, a complicating factor is a change in enzyme-substrate complex protonation state. If protons are given to or taken from the buffering solution upon enzyme-substrate complex formation, the heat observed contains a component due to the enthalpy of buffer ionization. Based on a series of experiments with buffers having a range of ionization enthalpies (ionization enthalpies from [126]), it appears that proton release upon binding and subsequent ionization of the buffer makes a major contribution to the apparent enthalpy of binding of dynorphin A(1-13) to TOP (Figure 4.2). Plotting the change in enthalpy as a function of buffer ionization gives a slope of -0.55 indicating 0.55 protons released during titration with the peptide. This might be explained in terms of the conformational change observed in His600 upon ligand interaction (Figure 4.2e). The pKa of His600 was calculated in both the unliganded dual truncated TOP structure as well as the dynorphin A(1-13) bound structure using the PROPKA webserver [127]. In the unliganded structure it has a calculated pKa of 7.3, but in the dynorphin A(1-13) structure the pKa is only 3.9. At a pH of 7.5 this calculated change would result in His600 losing 0.4 protons - not far from the experimentally observed value of 0.55.

Another complicating factor in ITC experiments is competing binding reactions. Great care was taken to purchase pure peptides and use only TOP purified to homogeneity in ITC experiments. Despite this care, our recombinant TOP was only able to bind 50-70% of the expected substrate resulting in saturation at molar ratios between 0.5 and 0.7. Since crystal structures showed the propensity for TOP to bind its own disordered C-terminus I hypothesized that this interaction might compete for some of TOP's binding sites. However, this hypothesis proved incorrect since dual truncated TOP behaves much the same as N-truncated TOP (Figure 4.3). The apparent lack of binding sites could be an indication that TOP carries resistant peptides with it through purification. Another explanation might be that our peptide is contaminated with peptide sequences without a tyrosine resulting in decreased absorbance at 280 nm and underestimation of the actual substrate concentration. More troubleshooting would be necessary to fully understand why recombinant TOP saturates at a low molar ratio in our ITC experiments.

### Dynorphin A(1-13) binding

In order to preserve substrates in their full length ITC experiments utilized N-truncated or dual-truncated TOP with the active site E474A mutation. Controls carried out using wild-type TOP and E474A TOP with or without EDTA confirmed the effectiveness of the E474A mutation in preventing significant peptide hydrolysis during the course of the calorimetry experiments (Figure 4.1). By using dynorphin A(1-13) as a model ligand and subtracting the enthalpy of binding associated with buffer ionization it can be shown that ligand binding is accompanied by a favorable change in entropy of 1.6 kcal/mol and favorable enthalpy change of -1.1 kcal/mol (Table 4.1). Weak interactions such as hydrogen bonds and Van der Waal's interactions are associated with relatively small enthalpic contributions compared to ionic interactions. These ITC results are therefore consistent with binding driven mainly by water release and weak interactions such as van der Waal's as seen in the crystal structure of dynorphin A(1-13). The hydrogen bonds formed in the TOP-dynorphin A(1-13) structure would also be formed to solvent in the free TOP and free substrate state likely reducing their enthalpic effect in peptide binding to TOP.

## Salt effects on dynorphin A(1-13) binding

Varying the ionic strength over the range 60-210 mM by altering sodium chloride concentration gave more than a four fold increase in observed binding affinity by ITC (Figure 4.4 and Table 4.2). This indicates the release of water or ions during complex formation [128]. There are three ordered waters displaced from TOP's surface in the dynorphin A(1-13) complex structure, but release of these three water molecules alone would not be sufficient to cause the observed change in binding affinity, since binding varies as 0.16 x #$H_2O$ released x [salt(M)] [128]. The dependence on ionic strength most likely is also caused by release of water from the peptide during binding. Also, it is possible that TOP in solution may close around dynorphin A(1-13) in a way not seen in the crystal structure resulting in the release of water and/or ions from other regions of the enzyme surface.

## Angiotensin II, adrenorphin, and neurotensin binding

The binding of three other substrates was also examined by ITC. Angiotensin II, adrenorphin, and neurotensin, all bind with different affinities, but with similar stoichiometry and enthalpy / entropy breakdowns as dynorphin A(1-13) (Table 4.1 and Figure 4.5). It is likely that these substrate peptides release protons during complex formation in the same manner as dynorphin A(1-13), therefore further experiments using different buffers are necessary to accurately characterize the enthalpic and entropic contributions to their binding.

## C-terminal product fragment binding

Synthesized peptides corresponding to the C-terminal fragments of dynorphin A(1-13) (dynorphin A(9-13), RPKLK) and neurotensin (neurotensin (9-13), RPYIL) yielded very different enthalpic and entropic components than those determined for the full length peptides (Figure 4.6). In particular, the binding of both peptides produced an unfavorable enthalpic term. Since both peptides are known to bind at a second site on the enzyme, it is possible that this complication is responsible for the observed difference in enthalpy of binding.

Interestingly, the C-terminal portion of adrenorphin also binds at two sites like RPYIL and RPKLK, but only when the Zn ion is removed. ITC characterization of adrenorphin binding to TOP after removing the active site Zn ion with EDTA shows a typical, favorable enthalpy of binding (Figure 4.5). This result suggests that the unfavorable enthalpic term for binding of dynorphin A(9-13) and neurotensin (9-13) may be due to their interaction with the Zn ion. Displacement of the water molecule normally coordinating the Zn ion may play a role. This water is deprotonated to some extent in the unliganded structure [129]. Its release would therefore cause proton release from the Tris buffer used for these experiments, an enthalpically unfavorable process (7.4 kcal/mol). These experiments should be repeated with other buffers to test this possibility. It also might be interesting to determine if Tris can be as a thermodynamic probe for displacement of the Zn coordinated water by a given ligand as is expected for many inhibitors designed to target neuropeptidase active sites [20, 31, 130].

It is not clear from these experiments what, if any, thermodynamic contributions are made by closure of TOP's interdomain cleft. Therefore, it is not possible to positively link any of the interactions seen in TOP-substrate complexes to the values measured by ITC. However, in a broad sense, the thermodynamic characteristics of TOP-substrate binding are consistent with the binding interactions seen in the crystal structures. It appears that at least for dynorphin A(1-13) the release of water from the ligand and binding surface is likely to contribute significantly to the interaction, and that polar effects (van der Waals contacts and hydrogen bonds) make only a roughly similar contribution.

## Table 4.1 Thermodynamic binding parameters of substrates.

| **Ligand**[1] | **$K_d$ (uM)** | **ΔH (kcal/mole)** | **ΔTS (kcal/mole)** |
|---|---|---|---|
| **angiotensin II** | 8.8 | -4.6 | 2.4 |
| **adrenorphin** | 0.35 | -8.9 | 0.1 |
| **dynorphin A(1-13)** | 0.17 | -7.5(-1.1)[2] | 1.9(1.6)[2] |
| **neurotensin** | 10.33 | -16.0 | -9.1 |

[1] Dynorphin A(1-13) was most thoroughly determined.

[2] Intrinsic enthalpy in parenthesis is the apparent enthalpy seen in Tris buffer minus heat due to buffer protonation.

### Table 4.2 Dynorphin A(1-13) binding versus ionic strength

| **Total ionic strength[1]** | **$K_d$ (uM)** | **H (kcal/mole)** | **ΔTS (kcal/mole)** |
|---|---|---|---|
| **60mM** | 0.505 | -18.0 | -9.3 |
| **90mM** | 0.386 | -15.4 | -6.5 |
| **150mM** | 0.162 | -9.7 | -.2 |
| **210mM** | 0.116 | -8.6 | 1.0 |

[1] Conditions were 50 mM Tris pH 7.5, 5 mM BME, 0.1 mM $ZnCl_2$, and 10-160 mM NaCl.

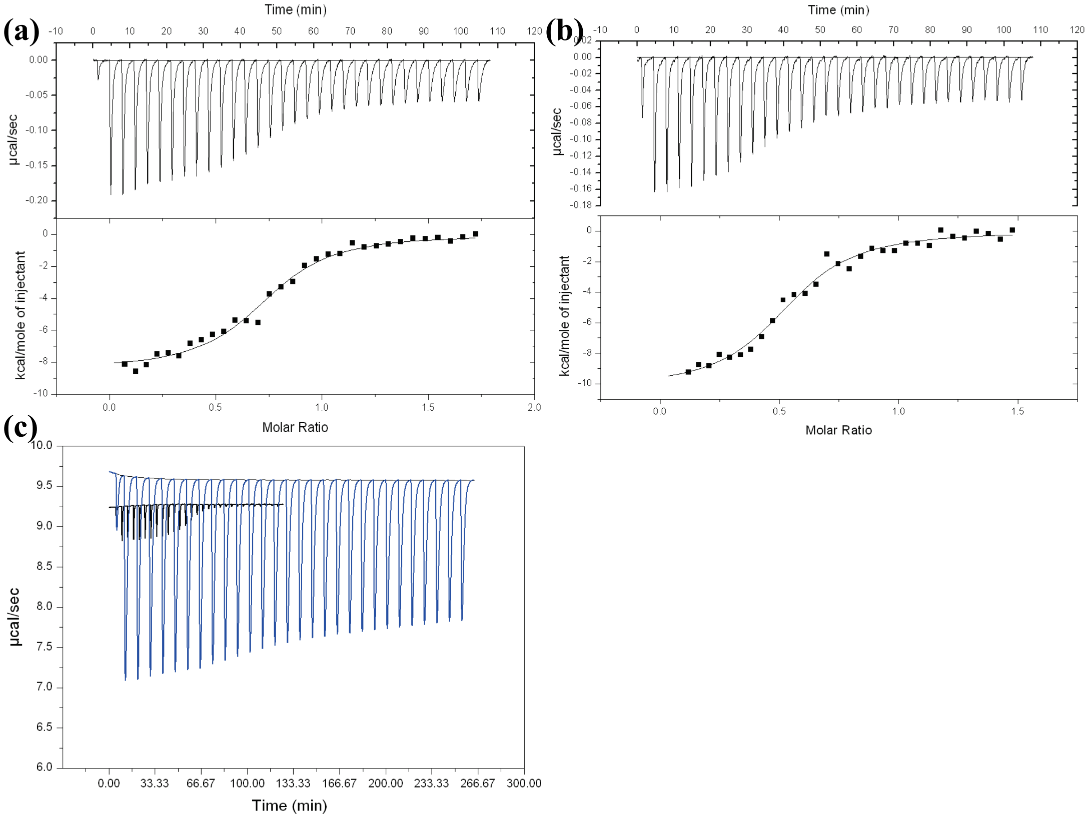

**Figure 4.1 Controls for activity during calorimetry. a)** Heats of injection versus molar ratio and enthalpy versus molar ratio dynorphin A(1-13) titrated into E474A TOP without any EDTA soak **b)** Dynorphin A(1-13) versus E474A TOP after dialyzing into 0.02 mM EDTA **c)** Heats of injection of dynorphin A(1-13) titrated into wild type TOP (blue) or E474A TOP (black). Activity results in a failure to achieve saturation and much larger heats of titration.

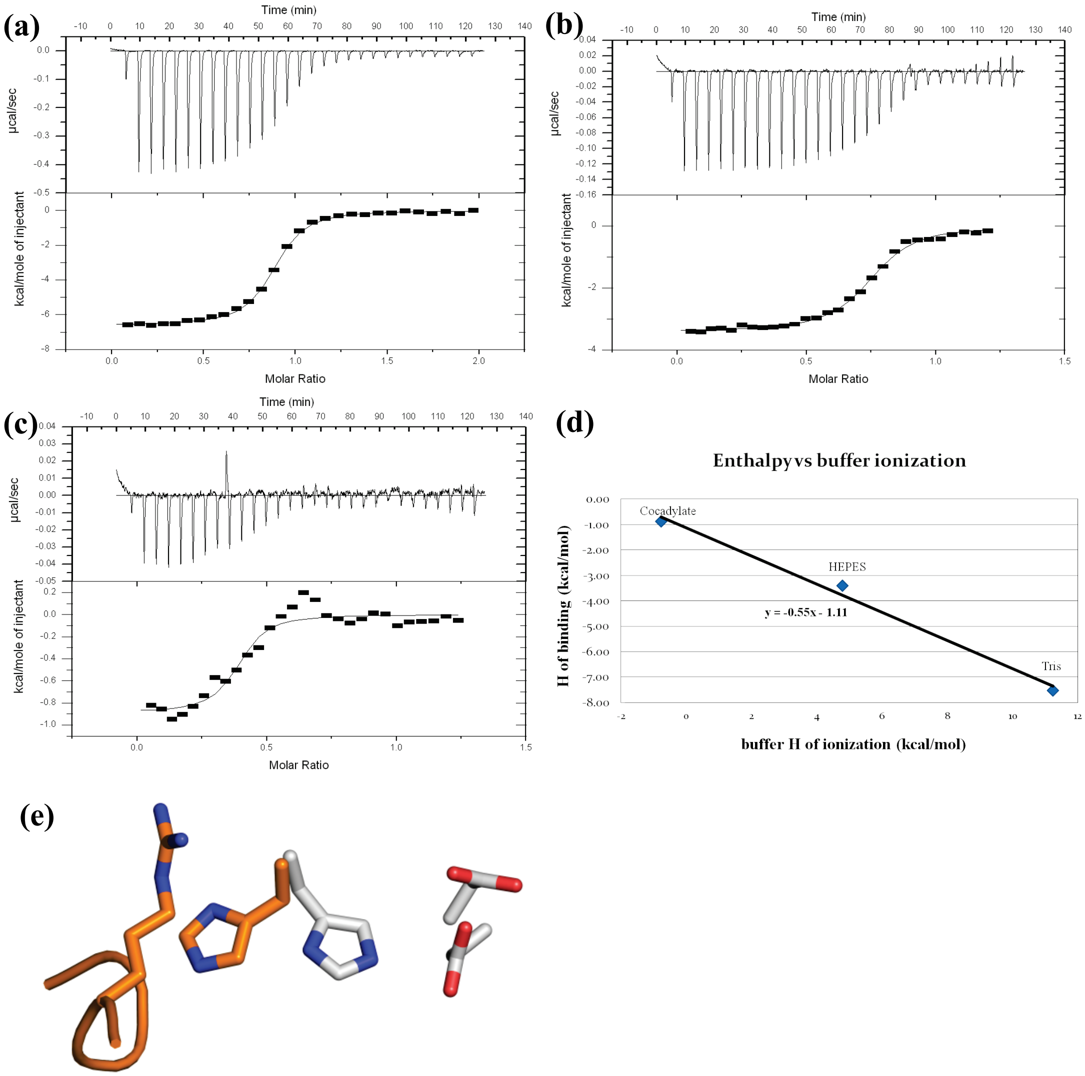

**Figure 4.2 Deprotonation upon ligand binding. a)** TOP vs dynorphin A(1-13) in 50 mM Tris pH 7.5 **b)** A parallel experiment with 50 mM HEPES buffer **c)** Parallel experiment with cocadylate buffer **d)** Plot of enthalpy versus buffer heat of ionization. The slope of the plot suggests one proton released upon peptide binding. **e)** His600 is a candidate for proton release because its conformational change moves it from a relatively acidic to basic environment upon dynorphin A(1-13) binding.

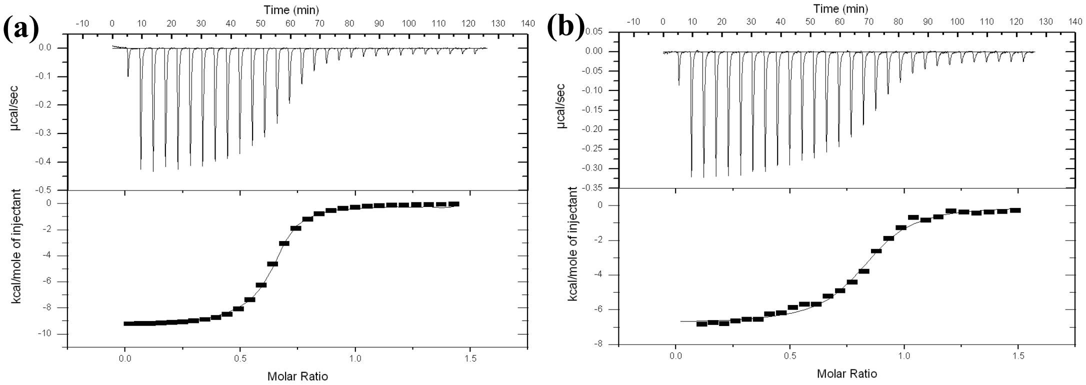

**Figure 4.3 Binding of dual truncated TOP vs N-truncated TOP.** Conditions were 50 mM Tris pH 7.5, 100 mM NaCl, 5 mM BME. **a)** Titration using N-truncated TOP $K_d$ = 0.16 μM. **b)** Titration using dual truncated TOP $K_d$ = 0.23 μM.

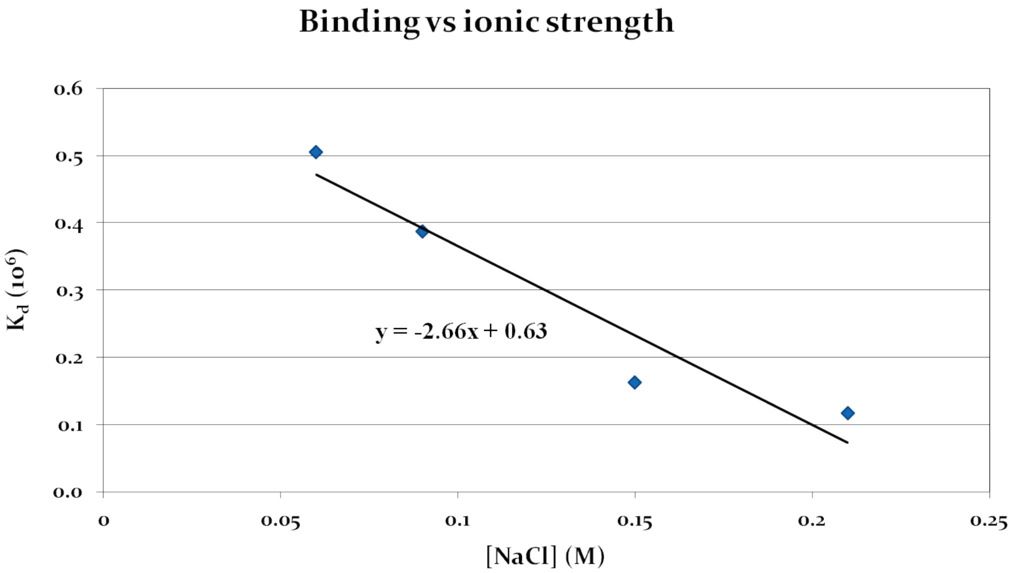

**Figure 4.4 Dynorphin A(1-13) salt series.** Binding constants are plotted as a function of ionic strength based on isothermal titration calorimetry of the peptide binding to TOP.

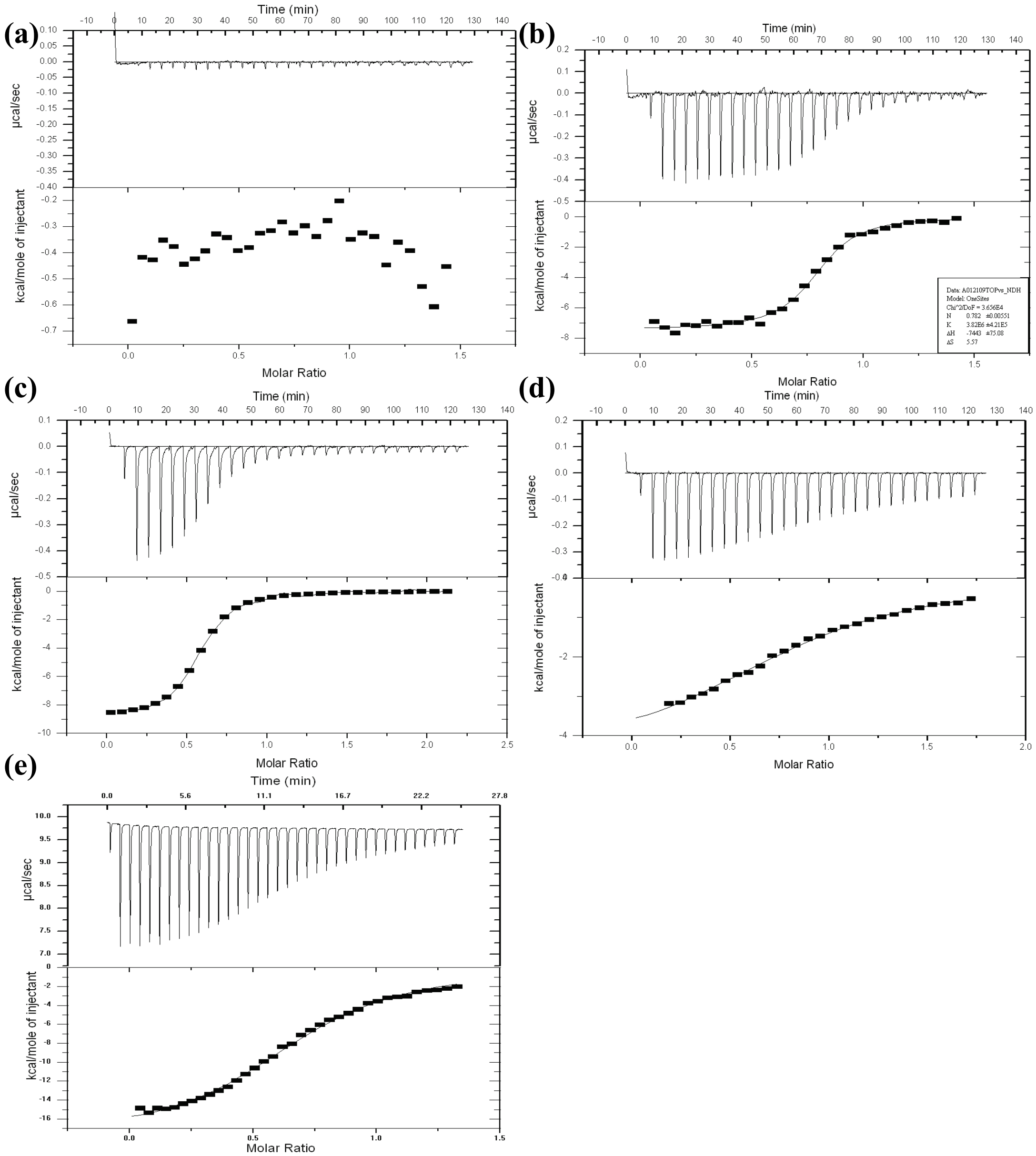

**Figure 4.5 Variety of substrates binding to TOP.** Conditions were 50 mM Tris pH 7.5, 100 mM NaCl, 5-10 mM BME. In the case of adrenorphin, 1 mM EDTA pre-soak was used to mimic crystal soaking conditions. **a)** Negative control with dynorphin A(1-13) titrated into buffer without TOP. **b)** dynorphin A(1-13). **c)** adrenorphin. **d)** angiotensin II **e)** neurotensin

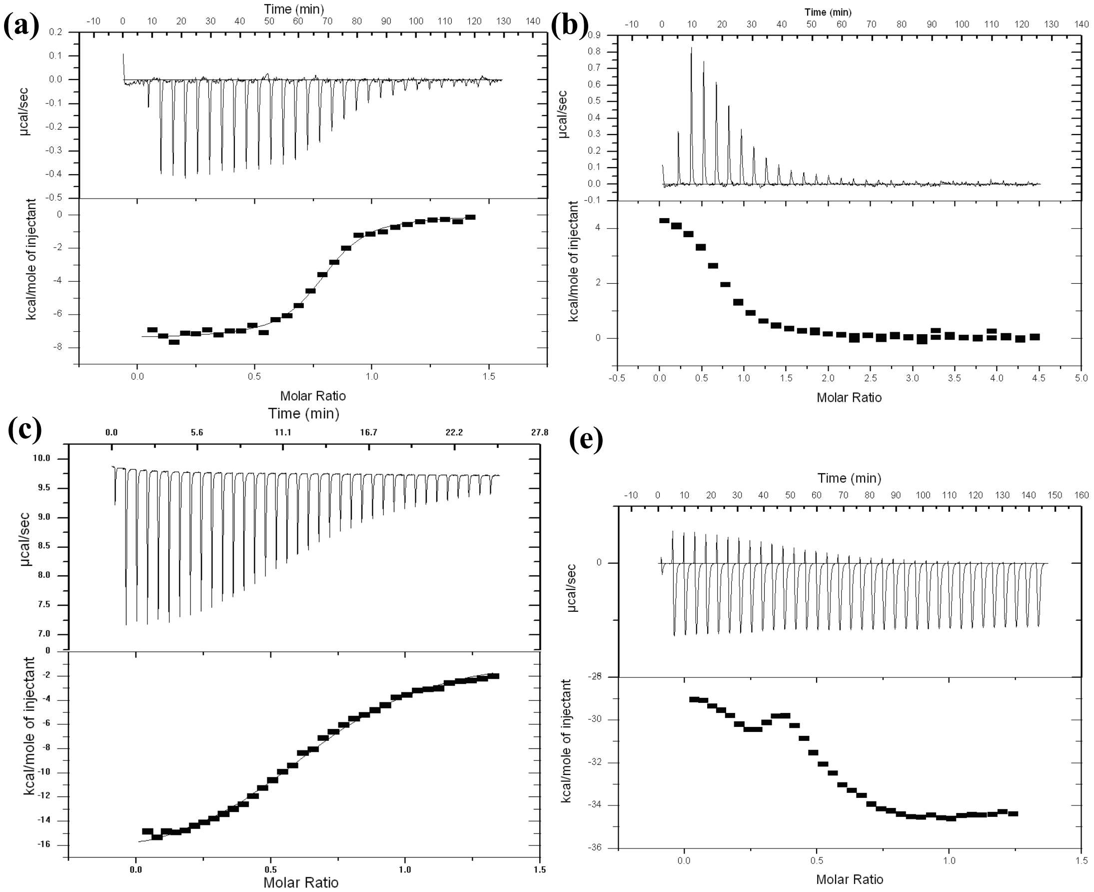

**Figure 4.6 Product fragment thermodynamics. a)** dynorphin A(1-13) **b)** dynorphin A(9-13) **c)** neurotensin (1-13). **d)** neurotensin (9-13). During neurotensin (9-13) titration the endothermic peaks do not show saturation indicating that they are likely due to mixing effects not binding.

# CHAPTER FIVE: Development of nanoparticle test tube fabrication method

## Approach to nanoparticle test tube manufacture

This is the first report of non-destructive replication being used to produce suspended nano test tube particles. A number of different parameters were varied during development of the test tube production method including: template pore depth, diameter, and lattice constant, metal composition and thickness, method of metal deposition, solvent polarity, ionic strength, pH, and temperature, sonication method and duration. Not all parameters could be systematically varied for each experiment. Most efforts failed to produce tube-shaped particles suspended in solution due to the difficulty of removing the tubes from the replication tape used as a mould to prepare them. After identification of a few of the critical parameters, a remarkably simple protocol for nano test tube formation and suspension was developed.

Porous aluminum oxide templates were wetted with a thin layer of acetone using a cotton swab. Cellulose acetate replicating tape 0.22 mm thick was touched to the wet surface with minimal pressure and capillary action was responsible for drawing the polymer down into the pore. After drying for 30 seconds the replicating tape was peeled off. Imprinted replicating tapes were mounted on glass slides and metal(s) deposited using a vapor deposition technique such as sputtering. Metal(s) were deposited at a rate of approximately 0.1 nm/sec and the samples spun to insure even coating. A quartz thickness monitor was placed beside the samples to measure thickness during deposition, and total metal deposition was kept to <10 nm. After coating the samples were cut off of their glass supports and immersed in a minimal volume of water in a glass vial. Finally, the glass vials containing immersed samples were sonicated for 15 min to release the nano test tubes from the surface.

### Critical parameters for template formation

Porous aluminum produced by one-step anodization of aluminum on a silicon wafer proved a robust template both in terms of life span and in terms of homogeneity of pore size. These templates (Figure 5.1 and Figure 5.2) lasted through 100-200 replications with a slow, predictable, decrease in pillar height (~2-2.5 nm / replication) and increase in pillar diameter (~0.2-0.3 nm / replication). Commercially available materials were also used, but in the case of porous aluminum oxide there were clear advantages to making our own. For trials with commercial material, I bought Whatman Anodiscs (AAO filters) and used them to make 200 nm diameter test tubes. However, this was a time consuming and difficult procedure because Anodiscs are designed without a backing and so had to be filled with epoxy and the epoxy carefully etched back prior to replication in order to control the pillar height. The anodiscs also contained multiple pore lattices sometimes resulting in heterogenous nano test tubes with multiple diameters (Figure 5.3a).

### Critical parameters for pillar coating

Large 200 nm pillars coated with 100, 50, 30, 15, or 10 nm of aluminum or titanium failed to release upon sonication. Efforts to encourage pillar breakage by tilting samples 45$^{o}$ during deposition in order to allow shadowing changed the morphology of test tubes to canoe shaped particles released into solution (Figure 5.3b). Only a 3-8 nm coating of metal(s) deposited face-on to pillars allowed pillars to be broken into single tube-shaped particles during sonication (Figure 5.4). It did not matter what method of physical vapor deposition was used, both thermal evaporation and sputter coating worked equally well.

Interestingly, the maximum thickness possible for the metal coating did not vary much for pillar lengths in the range used. For both 250 nm long and 1000 nm long pillars, the maximal coating thickness for good pillar release was about 8 nm of metal. Even using 200 x 1 μm diameter pillars from the densely packed pores of Anodiscs did not significantly alter the maximum amount of metal that could be deposited. Although it might be expected that shadowing by nearby pillars would prevent metal deposition at the base of pillars, this effect was not found in practice (Figure 5.5a-c). This was particularly unexpected, since sputtering is frequently described to be a poor method for depositing at the base of trenches with aspect ratio >1 [131, 132]. The good metal deposition at the base of pillars is probably due to the continuous network formed by inter-pillar trenches unlike the isolated pits used in previous reports [131, 132]. In our case, TEM micrographs revealed that metal was deposited to 8 nm thick only on pillar tips. The coating thins to about 4 nm at a point 200 nm below the tip, then thins more gradually to about 1 nm 800 nm below the tip (Figure 5.5). Pillars with bases varying between 250 nm to 1 μm in length could be coated with 8 nm of metal(s) and still converted successfully to nano test tubes presumably because the metal(s) at the base of these pillars all fell within the 1-4 nm thickness range. Pillars only 125 nm tall were attempted, but failed to release after initial experiments presumably because the metal at their bases exceeded 4 nm thick.

## Approaches for pillar release

A number of strategies for pillar release were tried, including polymer dissolution with solvents, sonication, heat shock, and oxidative plasma degradation of polymer (Figure 5.6). Out of these only oxidative plasma degradation and sonication were effective. Simple sonication in water breaks pillars off at the base provided the metal coating is thin enough (Figure 5.4). In contrast, oxidative plasma etching rapidly degrades the replicating tape and frees the whole sheet of pillars from the surface (Figure 5.7). This results in release of a significant amount of undesirable flat metal surface from the polymer in addition to pillars. Furthermore, release by plasma degradation still required sonication to break apart the sheets of pillars. Release by plasma degradation might be useful in some cases where hollow tubes are desired since tubes sonicated into water initially are filled with polymer, but plasma etching may partly hollow out the inside of pillars (Figure 5.8). In the interest of quality and simplicity, we adopted sonication alone as a method for pillar release.

## Quantification of suspended test tubes

The protocol developed here for nano test tube synthesis is simple and cost effective. Each template replication takes only a minute, so large pillared surface areas can be produced. Imprinting pillars on the surface potentially increases the final surface area by a factor between 0.5 and 7.6 depending on the density and dimensions of pores in the template (Table 5.1). This surface area is only achieved if all the replicated pillars break off and go into suspension. In our experience 70-90% of all pillars are released into suspension during sonication as quantified by cutting and weighing printed SEM micrographs of released pillars (Figure 5.9).

For applications utilizing the surface of nanoparticles, nano test tubes are competitive with standard commercially available nanoparticles. Producing $9 \times 10^{10}$ test tubes (~90 $cm^2$ of replicated template surface at the 100 nm diameter size) only requires a couple hours using a 4 $cm^2$ template. This yields the same number of particles found in 1 mL of commercial 40 nm gold colloid as ordered from BBI (Ted Pella catalog # 15707-20). However, a 40 nm colloidal gold particle has only 5024 $nm^2$ surface area. Depending on their dimensions each nanotube has 8 - 275 times that much surface. So, a preparation of nano test tubes could carry a much larger amount of surface immobilized therapeutics such as enzymes. The same porous alumina template can be used to produce $9 \times 10^{10}$ test tubes at least five times before a new template is needed.

Nano test tubes have the potential to demonstrate efficacy as delivery vehicles for biologics, with the delivery of enzymes being a particularly promising application. As catalysts, enzymes have the ability to convert large numbers of important metabolites over a long period of time. An approximation of the number of nano test tubes required for enzyme therapy can be calculated using Elaprase enzyme therapy for Mucopolysaccharidosis II (Hunter syndrome) as an example [133]. This therapy requires administration of 0.5 micromoles of idursulfase enzyme every two weeks. With a diameter of 4 $nm^2$ per molecule a dose would cover 13000 $cm^2$ of surface area. Projecting immobilization of idursulfase only on inner tube surfaces with dimensions 50 nm x 1 μm 6400 $cm^2$ of AAO template would be needed per dose. Using such a large AAO template is impractical if the template must be remade after each synthesis. However, by using our non-destructive method to quickly turn out 100 secondary templates from a single AAO primary template, 6400 $cm^2$ of pillars can be produced relatively rapidly from only 64 $cm^2$ of template. This replication process could be easily automated by passing acetone treated tape through a roller with AAO template on its surface.

Most enzyme therapeutics are quickly inactivated in the body. Idursulfase, for example, has an active half-life of only 114 minutes in the bloodstream. If enzymes could be stabilized through immobilization within nano test tubes they would exhibit active lifetimes beyond current enzyme therapies [67]. This, in turn, would allow much smaller doses requiring fewer nano test tubes.

Our nano test tube fabrication method produces tubes with walls varying between 1-8 nm in total thickness. Producing nano test tubes with very thin metal walls is attractive from a toxicity standpoint in therapeutic uses because it minimizes the amount of metal introduced into the body for a given surface area. For example, if a dose of idursulfase were immobilized on nano test tubes with an average 3 nm thickness the resulting injection would contain only 2 μl total metal volume. Once diluted in the bloodstream it would be well within amounts deemed innocuous for gold particles in cell viability assays [134].

### Advantages of gold and titanium during suspension

The incorporation of gold into nano test tubes has several potential advantages. The strong absorbance of gold allows visual and spectrophotometric quantification of tubual yield (Figure 5.10). The absorbance of nano test tube suspensions per mg of gold was comparable to that expected based on the absorbance of standard gold colloid solutions, indicating close to 100% suspension. Standard 5 nm diameter colloidal Au solutions had an adsorption of 472 abs/mg-cm while the tubes had 389 abs/mg-cm. (The dispersed Au nano test tube mass (.003 mg) was calculated using a sample with 3 nm thick gold on tube tips and presuming only 1 nm on sides with a yield of 76% pillars released.)

Incorporating gold also allowed us to follow nano test tube settling over time. Nano test tubes remained suspended in water in a 30 mL glass sample jar for up to twelve hours before noticeable settling began. After settling to the bottom of their containers they were easily resuspended by 15 minutes of sonication. The settling time after such re-suspension was measured by following the absorbance of a typical nano test tube sample at 600 nm over two weeks. Interestingly, the test tubes settled much more slowly in a 1 cm plastic cuvette than in a large sample jar. It took six days for half of the particles to completely settle in the cuvette (Figure 5.11).

During attempts to bond material to the nano test tubes, sonication after filtering samples was necessary to re-suspend particles washed on alumina filters. Titanium coating appeared to aid in resuspension. This advantage of titanium is likely due to the isoelectric point of titanium dioxide (6.0), which results in most of the groups being ionized in neutral solution. Purely gold tubes lacking the repulsive charge did not resuspend as well, resulting in some minor sample loss during washes (Figure 2.7).

### Nano test tube homogeneity

Non-destructive replication yielded homogenous mixtures of nano test tube particles as assessed by electron microscopic inspection. SEM micrographs show that nominally fifty nanometer diameter tubes vary in the range of 40-60 nm in diameter, and the length of each tube varies by less than 100 nm (Figure 5.4). The biggest challenge to producing homogenous test tubes is preventing pillars from being linked during metal deposition. Most samples had less than 5% of nano test tubes fused in this way. However, some samples had as many as 50% of tubes attached to at least one neighbor. Fusion can occur if metal is deposited too thickly causing pillars to join together at the base. Fusion also occurred sometimes at the tips or sides of pillars that were touching prior to metal deposition. Using AAO templates made in the laboratory, which had more widely spaced pores than commercially purchased templates, resulted in much lower levels of linking. Also, using a face on coating geometry, instead of coating at an angle to the pillar axis, was helpful in preventing pillar bending during deposition. Uniform pillar bending as a result of coating at an angle, however, might provide a means of making curled nano test tubes [89].

### Composite nano test tubes for differential surface chemistry

The ability to produce layered gold/titanium nano test tubes was confirmed using transmission electron microscopy. TEM images clearly show test tubes with two metal layers having different apparent densities, consistent with the presence of both metals (Figure 5.12). Titanium oxidizes in atmospheric conditions, unlike gold which remains in its elemental form. Thus, the outer surface has hydroxyl groups while the inner surface is lined with underivatized metal. Gold is a potentially useful inner surface since there is considerable experience with linking molecules of interest to gold surfaces [135]. Titanium is a desirable outer surface since tethers such as silanols allow macromolecule immobilization on titanium, potentially allowing PEGs or targeting macromolecules to be attached.

Unfortunately, all attempts to direct surface chemistry specifically to the inner surface of nano test tubes were unsuccessful. During the course of these investigations, it became clear that surface chemistry is possible on the outer surface of nano test tubes, but not the inner surface. This strongly suggests that the polymer core is not being completely removed from the nano tubes and is blocking access to the inner surface. In one experiment, test tubes were plasma cleaned long enough to remove more than 1 μm of polymer (1hr). They were washed and soaked with acetone and dimethylformamide (DMF) to dissolve polymer. Then they were burned in air at 500°C for one hour. Finally, they were washed in solvents again to remove any residual polymer ash. After this extensive attempt at polymer removal, biotinylation attempts using a thiol-biotin tether resulted in significant biotin detected on tubes with gold outer surfaces. However, in spite of all attempts to remove polymer no biotin was observed to attach on the gold lined titanium tubes, indicating the continued unavailability of inner test tube surfaces (Figure 5.13).

**Table 5.1 Nano test tube surface area increases by template.**

| diameter | 250nm depth | 500nm depth | 750nm depth | 1000nm depth |
|---|---|---|---|---|
| **50nm** | 0.5 | 0.9 | 1.4 | 1.8 |
| **100nm** | 1.0 | 1.9 | 2.8 | 3.7 |
| **200nm** | 2.2 | 4.0 | 5.8 | 7.6 |

*Values are based on averaging the number of pillars/area in SEM micrographs of the respective template replicas then calculating their outer and inner surface areas.

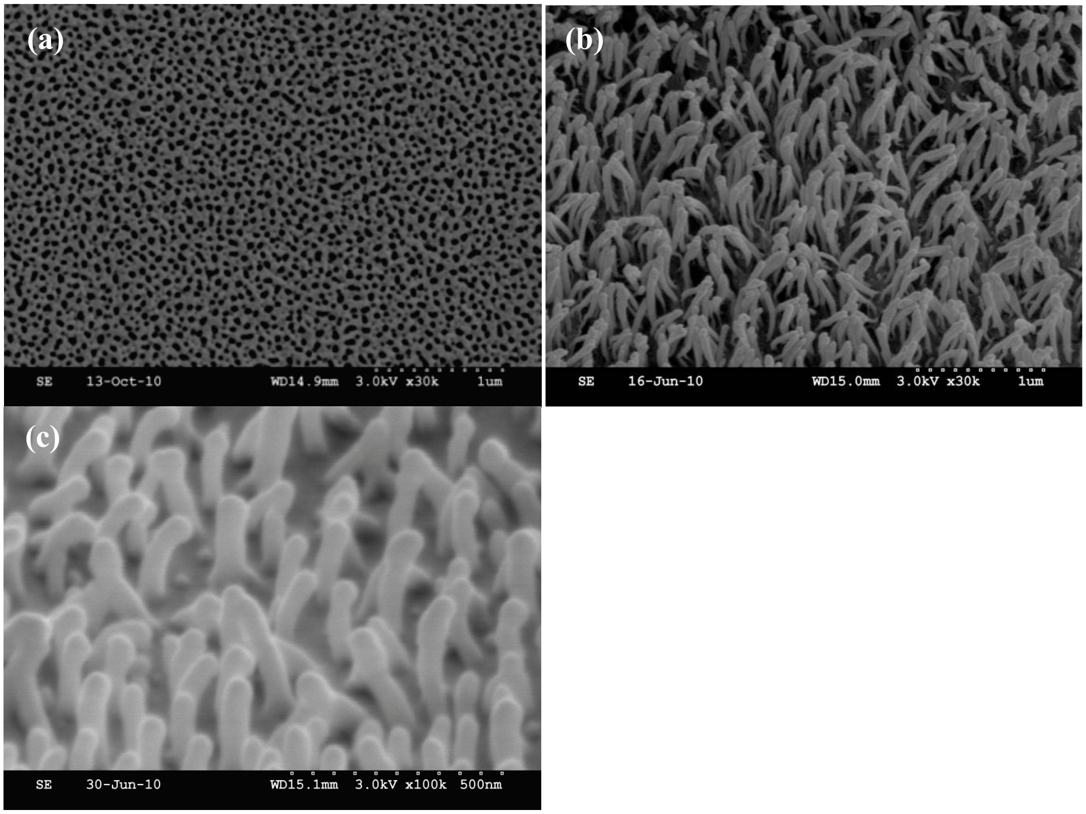

**Figure 5.1 SEM of 50 nm templates and pillars. a)** 50 nm pore diameter laboratory produced AAO template **b)** Resulting 1 μm tall pillars. **c)** 500 nm tall pillars resulting from replicating a thinner 50 nm pore size template.

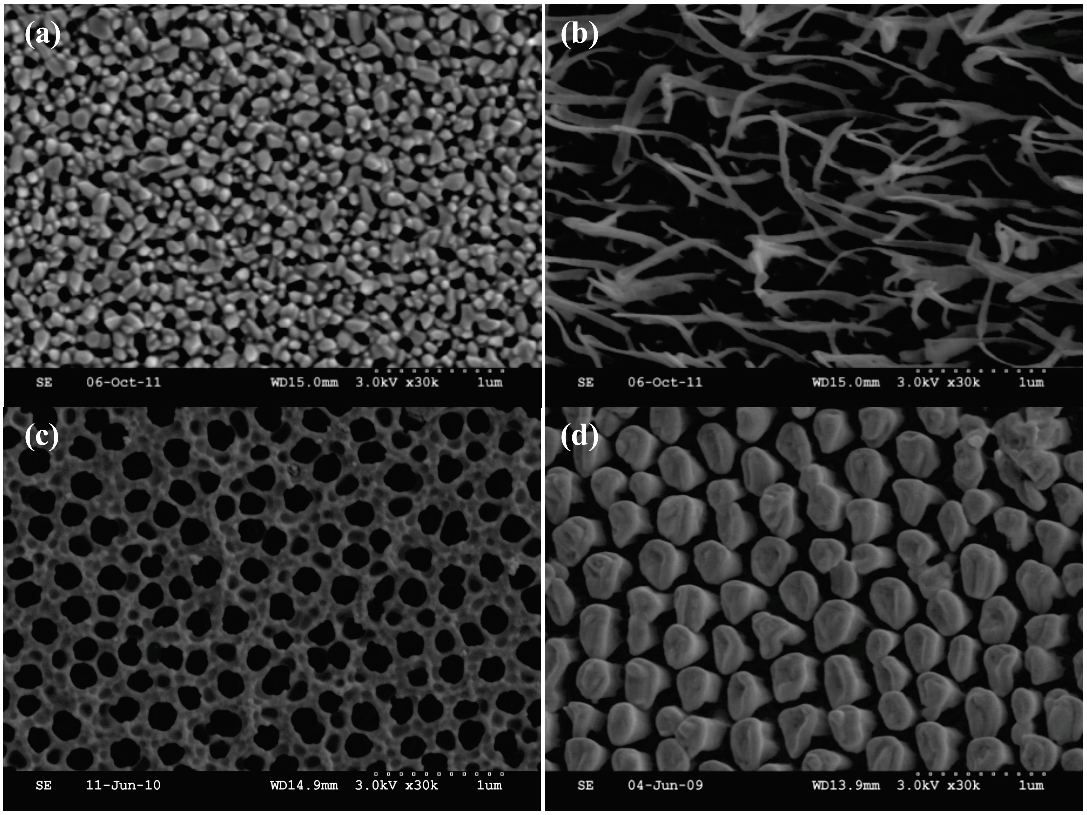

**Figure 5.2 100 nm and 200 nm templates and pillars. a)** 100 nm pore diameter laboratory produced AAO template. **b)** Pillars after replication of a template made similar to the one shown in panel a. **c)** 200 nm Whatman Anodisc$^{\text{TM}}$. **d)** Pillars from replicating Whatman Anodisc$^{\text{TM}}$ after partially filling the pores with epoxy.

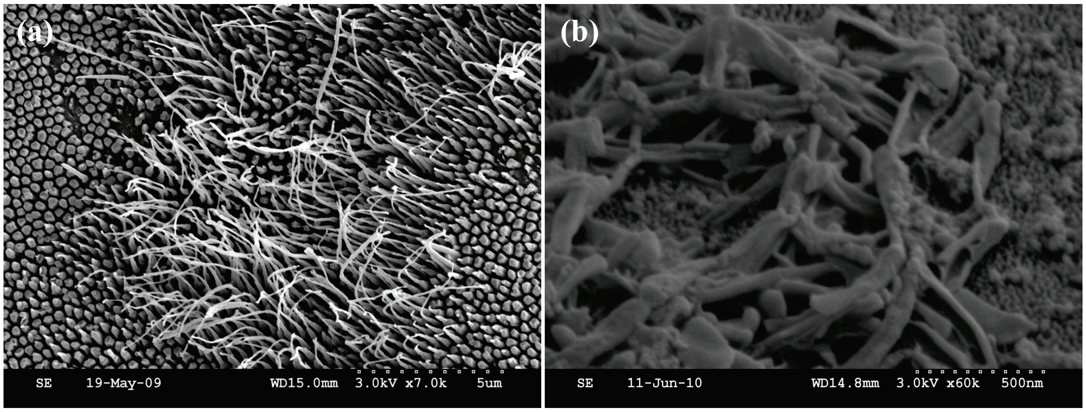

**Figure 5.3 Nano tentacles and nano canoes. a)** Patches of pillars replicated from 200 nm diameter Whatman anodiscs frequently had a single, very long, tentacle sprouting from their top. **b)** Nano test tubes (50 x 1000 nm) sputter coated with 5 nm of aluminum from a 45° angle. The metal is thick on one side and missing on the other resulting in canoe shapes.

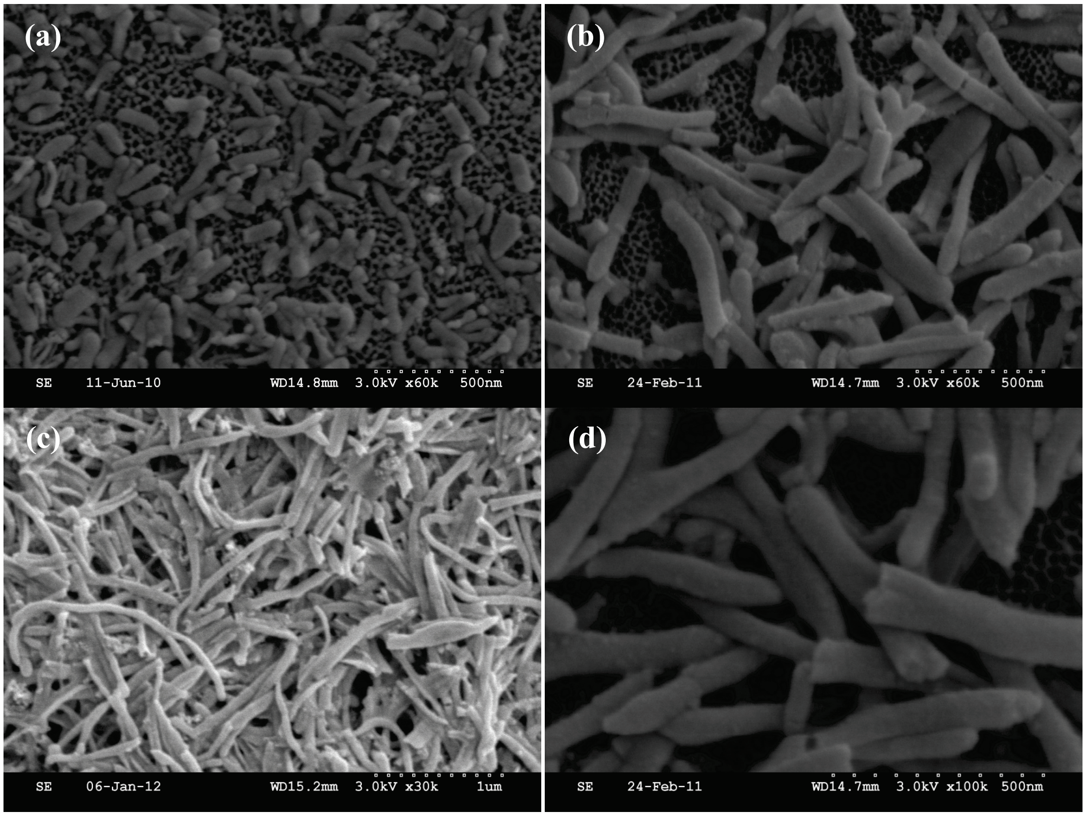

**Figure 5.4 Nano test tubes after suspension and filtration.** Nano test tubes on 20 nm porous aluminum filters after release from replication tape surface by sonication. **a)** 50 x 250 nm titanium test tubes. **b)** 50 x 500 nm test tubes. **c)** 50 x 1 µm test tubes. **d)** Close up of polymer filled titanium tubes.

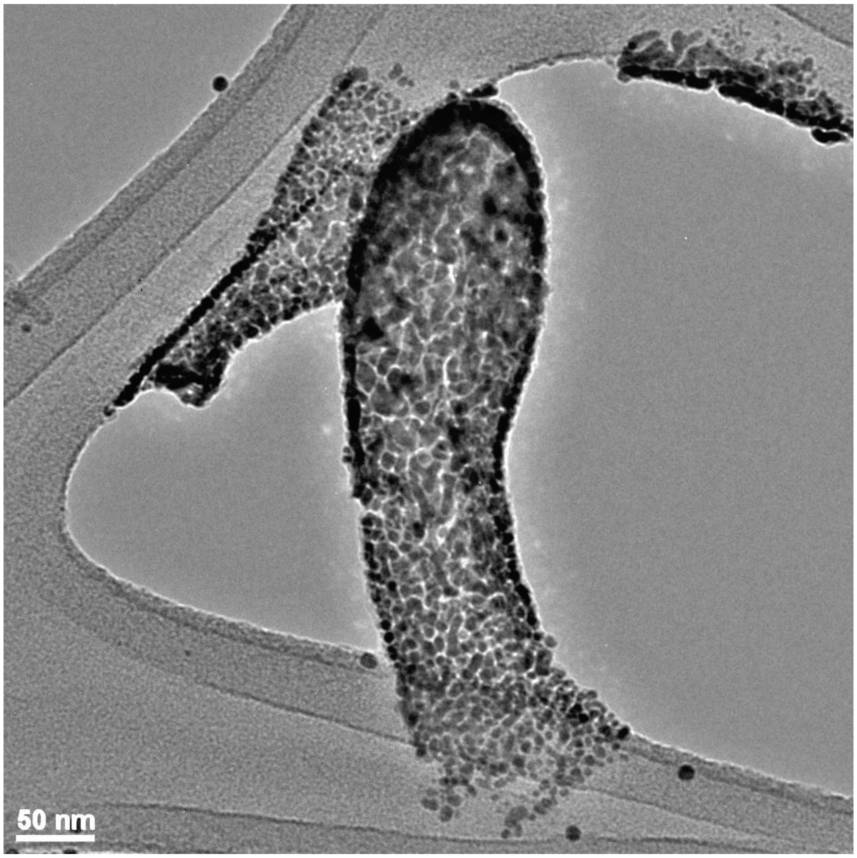

**Figure 5.5 Sputtered metal deposition.** This 100 nm diameter test tube was sputtered with nominally 4 nm gold. In practice the gold is only 4 nm at the tip and thins to 1 nm along the sides of the tube.

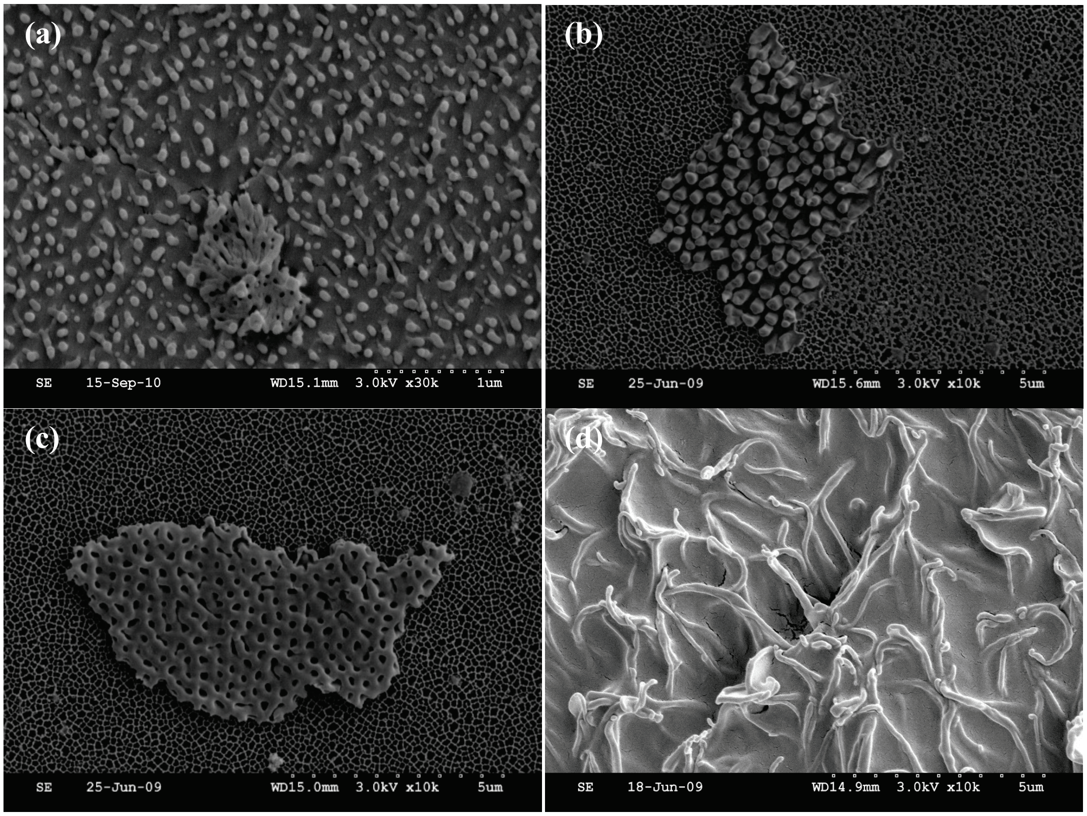

**Figure 5.6 SEM micrographs of unsuccessful pillar release. a)** Remaining 50 x 500 nm pillars on a replication tape sonicated after coating with 10 nm of titanium. **b)** Top view of tubes that released during sonication but remained connected at the rims in a large sheet. **c)** Bottom view of tubes that released in a large sheet. **d)** Pillars after attempted release by immersing coated replicas in acetone.

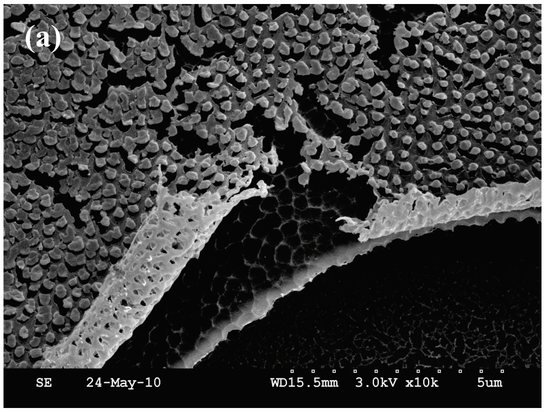

**Figure 5.7 Plasma degradation releases pillars.** 200 x 500 nm replicated pillars subjected to 1.5 hrs of oxidative plasma etching.

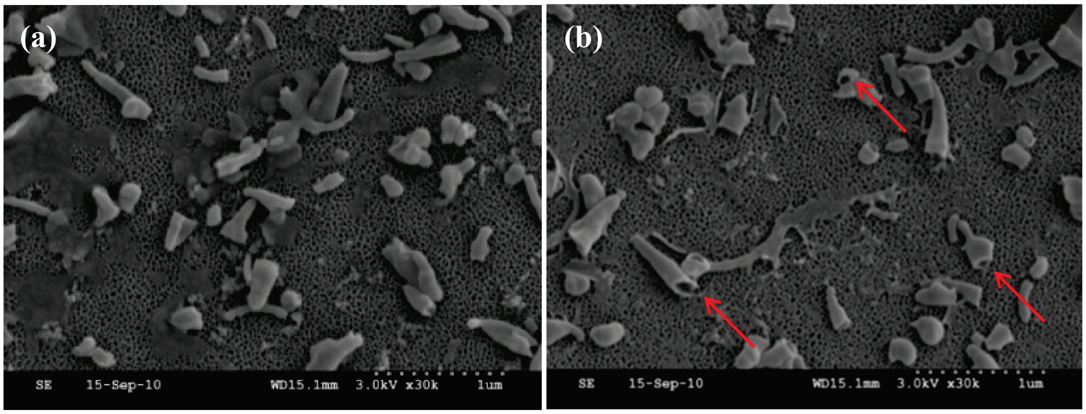

**Figure 5.8 Removing polymer from inside tubes.** Tubes are shown **a)** before and **b)** after plasma oxidation.

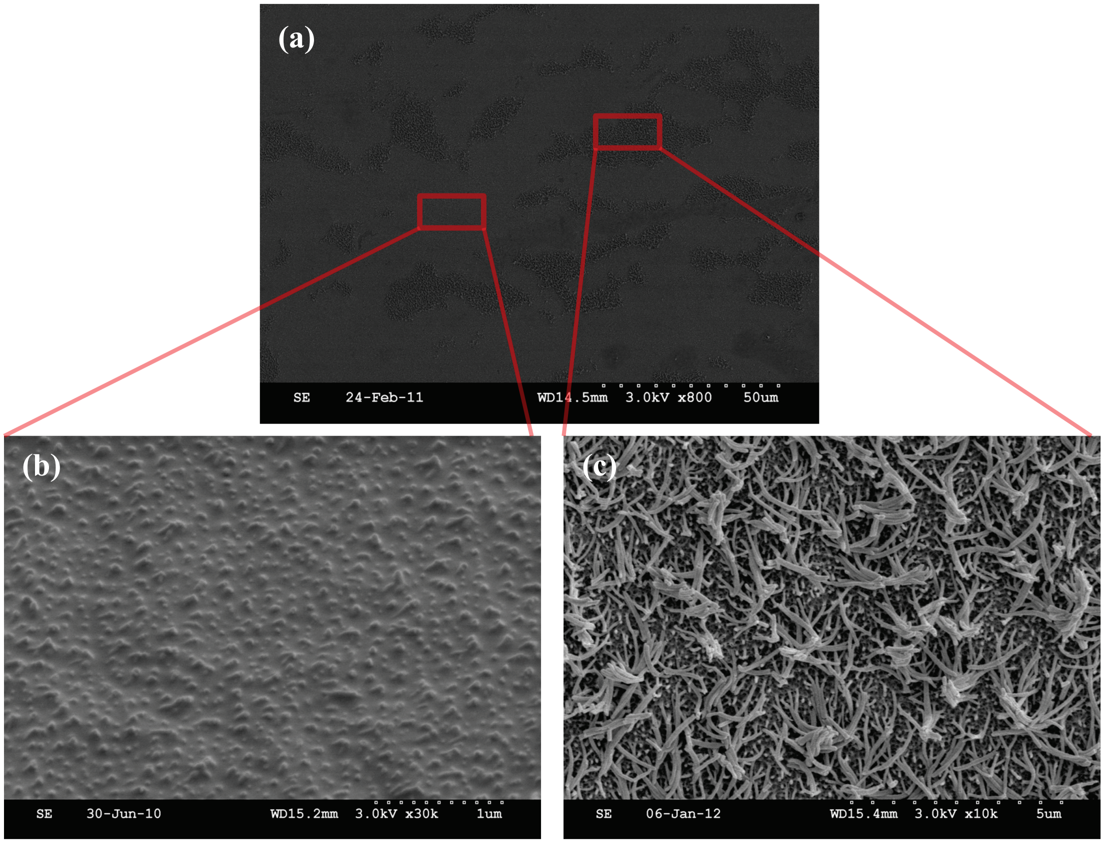

**76.2%** **23.7%**

**Figure 5.9 Quantification of test tube yield. a)** SEM micrograph of a replicating tape surface after sonication to remove pillars. **b)** Close up showing successful release (76.2%). **c)** Close up of area of incomplete release (23.7%).

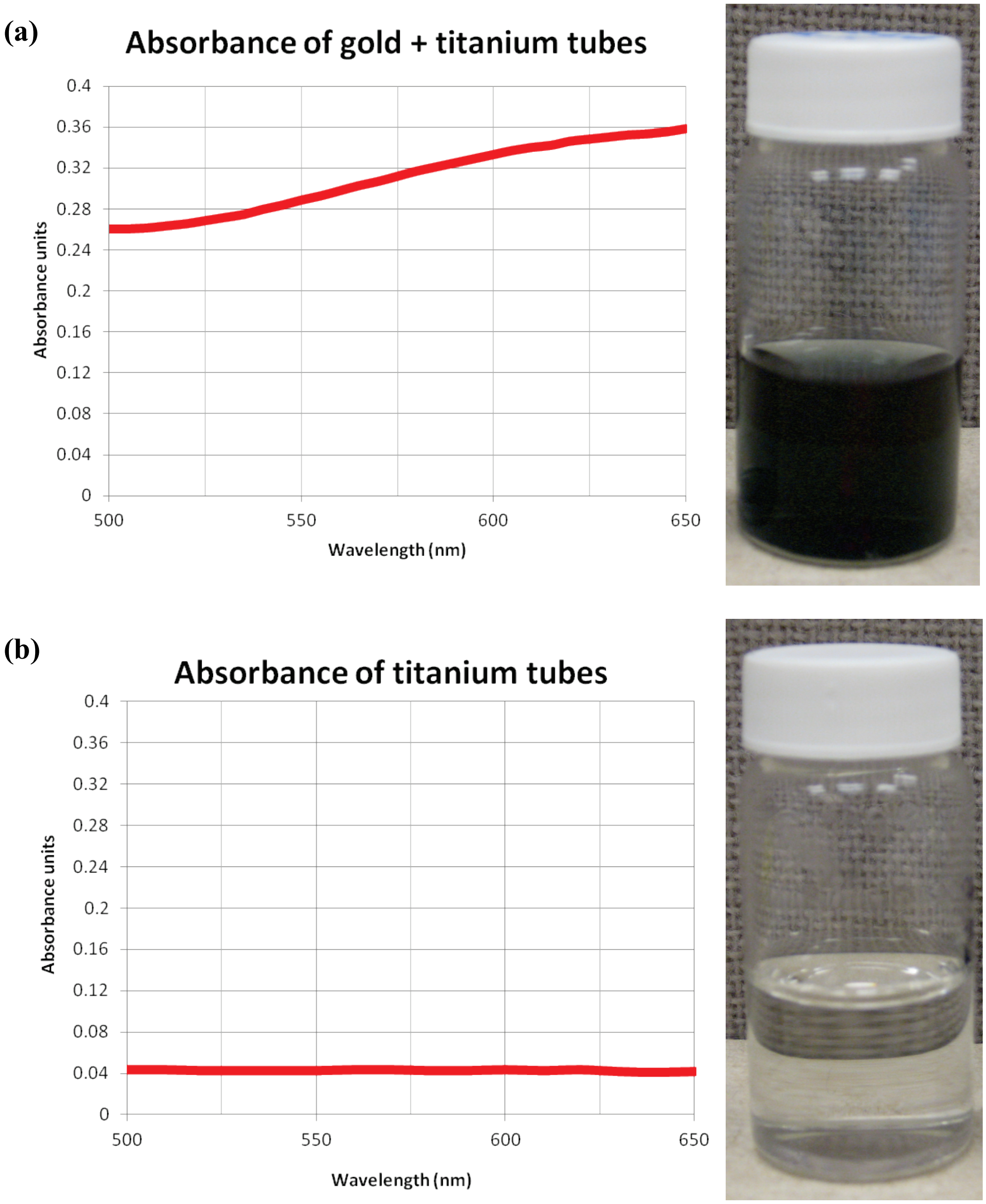

**Figure 5.10 Gold nano test tube absorbance spectrum.** The absorption spectrums of 100 nm x 1 µm test tubes at a concentration of $6.5\text{x}10^9$ tubes/mL (0.29 cm path length). **a)** Gold-titanium hybrid test tubes showed relatively high absorption with a maximum at 650 nm. **b)** Titanium test tubes at the same concentration had negligible absorption.

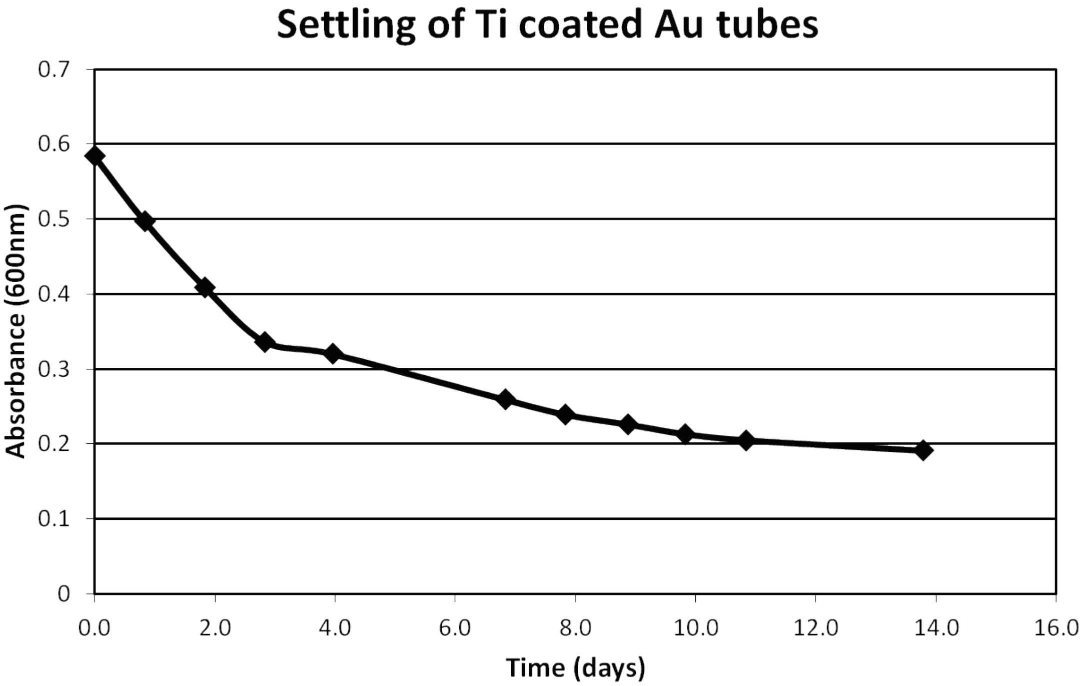

**Figure 5.11 Gold nano test tube absorbance over time.** 100 nm x 1 μm nano test tubes composed of a 5 nm gold layer coated with 3 nm titanium were allowed to settle in a 1 cm cuvette. Absorbance of the suspension at 600 nm was measured at the indicated time points.

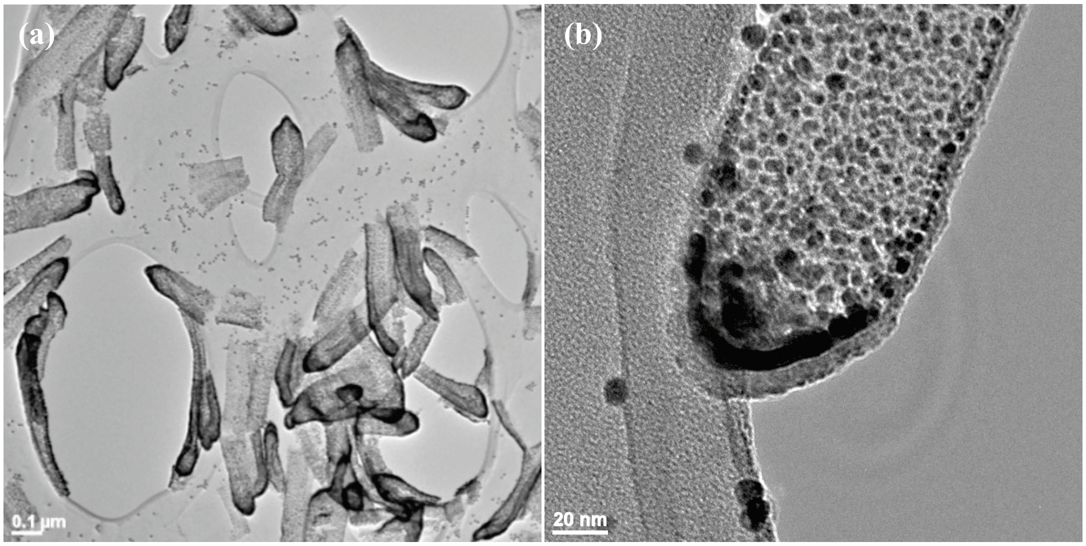

**Figure 5.12 Gold lined titanium test tubes in TEM. a)** 50 x 500 nm gold lined titanium test tubes. **b)** Close up view of a test tube showing the layers of dark (gold) and light (titanium) contrast.

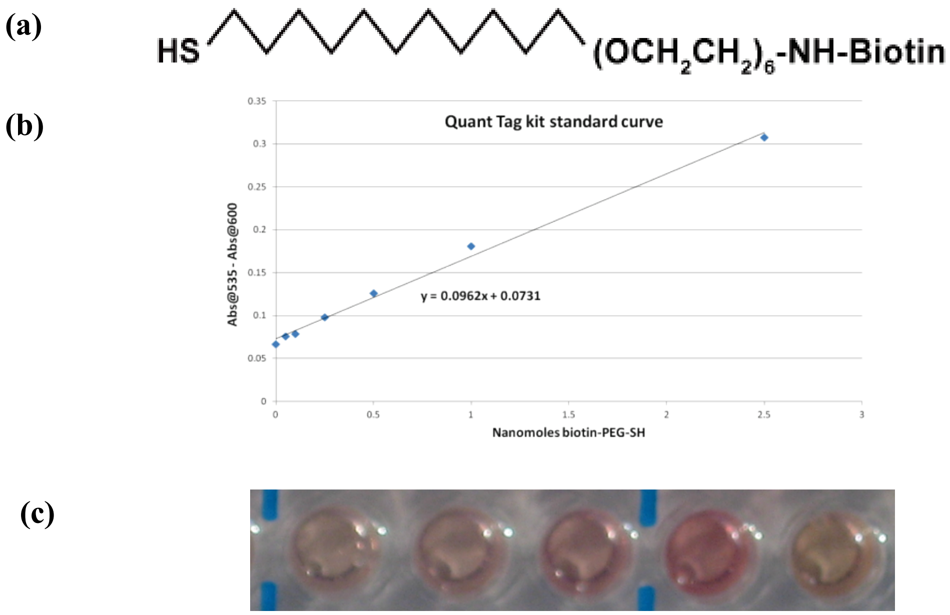

(d)

| Sample | Attached biotin (nmoles) |
|---|---|
| All gold tubes | .58 |
| Gold lined titanium tubes | .05 |
| Titanium tubes | -.04 |

**Figure 5.13 Biotin immobilization on nano test tubes. a)** Biotin conjugated thiol linker **b)** A representative standard curve for the Quant Tag biotin detection kit. (A standard series was done in parallel with each experiment.) **c)** Photograph of the four most concentrated biotin standards followed by pure gold test tubes sample. **d)** Quantification of biotin on each sample using Quant Tag standard curves.

# CHAPTER SIX: Summary and future directions

## Structural basis for TOP substrate recognition

A model for TOP substrate recognition and hydrolysis was developed in a previous dissertation from our group [104]. This model has been refined based on the work presented here. Changes to the model largely stem from a more critical evaluation of substrate electron densities plus the introduction of a new TOP construct lacking the last ten C-terminal residues. Structures with improved ligand occupancy led to the conclusion that adrenorphin, bradykinin, dynorphin A(1-8), and neurotensin complexes should be modeled with the substrate's registration shifted to fill unexplained density at the C terminus. Unfortunately, LHRH, dynorphin A(1-17), and substance P complex structures both in this work and in previous studies [104] had poor density that could not be used to unambiguously assign substrate registration in complex with TOP. Therefore these structures were not included in the current analysis. Of the previously modeled TOP-substrate structures, angiotensin II and dynorphin A(1-13) structures were judged in the correct registration, and these were carried over largely as originally modeled, with additional residues modeled on the N terminus of angiotensin II. Models for adrenorphin, bradykinin, dynorphin A(1-8), and neurotensin have been revised, and new structures have been determined for dynorphin A(1-8) D8, dynorphin B(1-9), and immunoglobulin 4 ligands binding to TOP.

This study identifies the unusual binding surface that TOP and similar neuropeptidases use to recognize their substrates, and it sheds light on the conformational changes associated with initial substrate binding. We propose that unliganded TOP in its open form typically interacts initially with substrates through domain I at the identified

C-terminal binding site. Initial binding is mediated through interactions with four to eight substrate residues, with the strongest interactions generally occurring with residues C-terminal to the scissile bond. The broad substrate specificity of TOP is due to the characteristics of the binding surface (Table 6.1). The relatively flat, carbon rich, binding surface that allows interactions to a wide variety of substrate sequences, which bind in an extended conformation. Furthermore, differing sequences near the substrate C-termini are accommodated by residues that alter conformation to optimize interactions. Side chains from residues of the bound peptide generally lie in shallow grooves rather than recognition pockets characteristic of interactions conferring specificity in proteases [136, 137]. These binding sites are able to accommodate multiple residue types and generally make few specific interactions. The backbone path of bound peptides was seen to vary for the different sequences, presumably the flat surface permits them to optimize interactions in this manner.

The long, flat binding surface found in TOP is in contrast to sequence specific proteolytic enzymes such as trypsin, chymotrypsin, and matrix metalloproteases, that recognize specific side chains through interactions at one or two relatively deep pockets [136-138]. The shallowness of TOP's subsites allows side chains to adopt a variety of conformations so that the substrate's side chains can deploy in whatever way maximizes the burial of hydrophobic surface and forms the most van der Waal's interactions. Substrates in our structures can be clearly seen taking advantage of this freedom when their coordinates are superposed (Figure 3.14). Studies systematically varying the residues in TOP substrates or inhibitors have previously identified mild preferences for a basic residue at P2' and a hydrophobic residue at P3' [31, 43]. These preferences are probably caused by Glu616 which lies at the bottom of subsite 1 and by the particularly hydrophobic nature of subsite 2. TOP substrates such as dynorphin A(1-13) that are able to insert both a basic and hydrophobic residue at once into these two subsites might be expected to have a particularly low $K_m$.

An early study of TOP activity found that a minimum length of six residues is required for substrate peptides [110]. This minimal length is generally consistent with the findings reported in this dissertation, since between four and eight residues were found to be ordered at the binding site. The structures reported here also explain to some extent the restriction on maximum length of peptides to about 17 residues [43, 110]. Simple modeling of a 17 residue peptide in extended conformation with the C-terminus placed appropriately at the substrate-binding site, suggests that only about that many residues can be accommodated in the closed end of the central channel of the enzyme. It would be difficult for the N-terminal residues of the peptide to turn and exit the channel, since elements from the enzyme overhang the channel at the closed end.

Dual truncated TOP provided unexpected insights into the true unliganded structure of the TOP binding site. Earlier structures of TOP showed His600 and Tyr605 located in the binding surface roughly facing the open end of the central channel. Upon truncation of TOP's disordered C-terminal tail the binding site surface, most notably His600, Tyr605, and Arg498 was observed adopting a different conformation. The apparent conformational changes illustrate the value of crystallizing TOP without the terminal disordered regions.

Analysis of related structures of enzymes in the cowrin family reveals that all were crystallized with disordered regions long enough to interact with the binding site except for neurolysin (reviewed by [139]). Furthermore, residues in these paralogs, with the exception of neurolysin, equivalent to His600 and Tyr605 in TOP have conformations similar to those seen in TOP when the disordered C-terminal residues are present [52, 140-142]. It may be that cowrins tend to crystallize with their neighbor's tail inhabiting their binding site which could have the dual benefit of stabilizing a relatively labile region during crystallization and also providing intermolecular contacts. Neurolysin is the exception because it has no disordered C-terminal tail [50], and here the loop containing the equivalent of Tyr605 is disordered. The substrate-binding surfaces of these paralogs probably adapt to substrates as the binding surface of TOP does, but it may be necessary to crystallize shortened constructs before the conformational change upon ligand binding can be visualized.

## TOP and antigen processing

Out of the vast array of possible sequences for MHC I presentation there is a culling process that reduces the number of peptides that might be loaded onto MHC I (Figure 1.2). The trimming and culling of the antigenic peptide population in the cytosol is attributable to a number of cytosolic oligoendopeptidases, oligoexopeptidases, and aminopeptidases. It has recently been shown that TOP, in particular, is key in limiting the population of peptides available for association with MHC I [15, 16, 143-145]. Interestingly, although TOP hydrolyzes many cytosolic oligopeptides in general, against a pool of randomly selected MHC I antigenic peptides it performed very poorly [16]. The lack of processivity was not due to poor affinity, since each MHC I peptide bound

TOP with affinities in the nanomolar to low micromolar range. Rather, the peptides acted as competitive inhibitors [16, 146]. That TOP plays a role in culling out peptides for MHC I presentation was confirmed by T cell activation studies using specific TOP inhibitors. Antigen presenting cells were transfected with hsp65 then their ability to induce proliferation of T cells was tested with or without addition of a specific TOP inhibitor (cFP-AAY-pAB) into the cytosol. The ability of inhibitor treated cells to activate T cells through CD8 / MHC I antigen presentation was reduced by more than half [144]. TOP's substrate binding surface, identified here, with shallow hydrophobic / aromatic grooves and adjustable C-terminal recognition motif suggests it is well adapted for hydrolyzing a large set of potentially antigenic sequences. In addition, the structure of the antigenic IgG4 fragment binding to TOP as a competitive inhibitor provides one example of how certain sequences avoid hydrolysis and increase their chance of presentation on MHC I.

## Productive versus non-productive binding conformations

The conformations adopted by substrates on TOP's binding surface can be correlated with successful processing. The most dramatic examples of poorly processed peptides that yielded structures are dynorphin A(1-13), angiotensin II, and IgG4 peptides. In the case of dynorphin A(1-13) product inhibition by the C-terminal is likely responsible for inhibition of TOP. Previous studies in this group showed that TOP processes dynorphin A(1-13) at least once and that peptides corresponding to the C-terminal product fragment dynorphin A(9-13) potently inhibits TOP with a $K_i$ of 0.4μM [104].

The structures of TOP complexed with angiotensin II and IgG4 point to a different explanation for their inhibitory properties. Both angiotensin II and IgG4 bind to TOP in a manner that differs from a typical substrate peptide. Instead of extending at a $45^{o}$ angle out from domain I and up towards the closed end of the central channel, they bridge the cleft in a direction nearly perpendicular to the channel (Figure 6.1a,b). The strong Zn coordinating interactions that these two substrates form with domain II likely stabilize this binding orientation. Angiotensin II coordinates Zn through the side chain of its N-terminal aspartate residue and also interacts with Glu469 and Glu509 through Arg2 of the peptide (Figure 3.24). IgG4 coordinates the Zn ion through the carbonyl carbon of Gly4, which displaces the catalytic water at the active site. It also forms a charge-charge interaction with Arg498 through a bridging water molecule and 4-5 hydrogen bonds to the β6 strand of the enzyme, which is located over the active site (Figure 3.25).

The conformations of angiotensin II and IgG4 in the domain I binding site fail to induce the liganded conformation of the 599-611 loop seen in normal substrates. If they bound in the normal manner, angiotensin II would form a hydrogen bond with Tyr605 through the backbone carbonyl oxygen of Val3 and IgG4 would do the same through Gly4. But this is not the case. Tyr605 remains in its extended conformation pointing into the channel at Asp83 instead of pointing towards the active site Zn ion (Figure 6.1c).

Overall, then, both angiotensin II and IgG4 bind in a manner that is incompatible with hydrolysis by the enzyme. Instead of binding primarily to the hydrophobic surface on domain I with their C-terminal residues mediating the interaction, they cross the interdomain cleft and interact with domain II via polar interactions and Zn ion coordination. Not only are the N-termini more ordered, but the last C-terminal residue is also more ordered in angiotensin II and IgG4 since in both cases the last residue interacts with less mobile areas of TOP's surface (Figure 6.1d). This partly explains good density seen for the whole length of these substrates and suggests that these sequences may lack contacts with TOP surfaces that physically destabilize the other substrates. Furthermore, although these peptides coordinate the Zn ion in the open TOP complexes they do not form the expected geometry for hydrolysis. Angiotensin II coordinates Zn through an aspartate side chain, and the closest peptide bond is located well away from the active site. IgG4 interacts with the Zn ion with coordinating main chain carbonyl oxygens but in such a way that the catalytic water is displaced and hydrolysis cannot occur. Thus these two peptides act as classic competitive inhibitors, blocking the active site machinery to inactivate the enzyme.

## Implications for neuropeptidase inhibitor design

The angiotensin II, IgG4, dynorphin A(9-13), and neurotensin (9-13) structures provide examples of tight binding that are instructive for designing specific TOP inhibitors. In contrast to substrates that are efficiently hydrolyzed, these sequences have significant interactions formed with domain II as well as domain I. Furthermore, each of these is seen to coordinate the active site Zn.

Angiotensin II binding is anchored in large part by its N-terminal aspartate and C-terminal phenylalanine. If angiotensin II is used as a template for inhibitor design these terminal anchor residues should remain the same. However, the binding affinity might be improved by changing His6 to a large hydrophobic/aromatic residue in order to take better advantage of hydrophobic subsite 2. Also, Val3 appears to remain solvent accessible in the complex structure, so it could be changed to a small polar residue to improve substrate solubility.

Dynorphin A(9-13) and neurotensin (9-13) bind to both domains of TOP and either site would effectively compete for binding with other substrates (Figure 3.28). Both fragment structures confirm that five residues is a suitable length for binding to domain II. Their binding is anchored on domain II by the C-terminal carboxylate group and by Arg9 so these should be conserved in inhibitors. The structure of neurotensin (9-13) is poorly defined on domain I and so cannot serve as a template for inhibitor design. The dynorphin A(9-13) structure provides opportunity for optimizing binding to both domains. Lys13 may interact unfavorably with His424, and it could be converted to a negatively charged or polar residue to improve affinity. Similarly, Lys11 of dynorphin A(9-13) may interact unfavorably with His87 on domain II; however, it forms a favorable interaction with Glu616 in subsite 1 of domain I. It might be advisable to exchange it for a neutral hydrophobic residue such as a methionine or leucine since this would be favorable in the domain I interaction and less unfavorable interacting with domain II.

The strategy outlined would produce inhibitors for binding to both domains in the open form of TOP. Fortuitously, the structure of TOP in complex with dynorphin A(9-13) also provides an opportunity for designing longer TOP inhibitors that bind to the closed form. The two peptides with sequence RPKLK interact on opposite sides of the cleft, and where one peptide ends the other begins. This can be best visualized by dividing the two domains of TOP and superposing them on the structure of bacterial dicarboxypeptidase (DCP) (pdb ID 1Y79) which was solved in the closed form. This simple movement carries R9 of the fragment bound on domain I to the same position as

K13 of the fragment bound on domain II (Figure 6.2). A single sequence RPKLRPKLK can be modeled making all the same interactions as the two fragments except with the surrounding TOP protein closed similar to DCP. This peptide inhibitor could then be improved by introducing a phosphinic group [20] between Lys5 and Arg6 to coordinate Zn ion and prevent cleavage. Also, a variation of the sequence might improve binding as described above, by replacing Lys3 with a hydrophobic residue (ie RPMLRPKLK) to prevent clashes with His87.

## Domain I residues in catalysis

Thermolysin-like metalloenzymes such as TOP are believed to use at least one polar or charged residue to stabilize the anionic catalytic intermediate [147]. His600, Tyr605, and Tyr612 have all been shown to affect TOP catalysis with mutation of Tyr612 having a particularly large effect [115, 148]. An important role for Tyr612 is supported by these structures since it is within hydrogen bonding distance of all backbone carbons attacked with the exception of resistant substrates such as dynorphin A(1-13) and angiotensin II. However, the orientation of Tyr612 relative to the backbone must change during hinge closure as the carbonyl oxygen of the scissile peptide bond coordinates the Zn ion at the active site. His600 and Tyr605 interact with the main chain of bound peptides, again consistent with mutagenesis identifying them as important in the catalytic cycle.

## Models for closed TOP / substrate complexes

As has been noted, the substrate binding seen in the crystal structures presented here represents an initial binding event, and a hinge-like, partial closing of the central channel would be required to move the bound peptide into position for hydrolysis by the enzyme. It is important to keep in mind that substrate peptide residues N-terminal to those ordered in the complex structures reported here would likely interact more strongly with the enzyme in the closed form. Contacts with other TOP molecules in the crystal lattice prevent the closure from occurring in the crystals, and to date TOP has not been crystallized in the closed form despite extensive trials. Other metallopeptidases in the TOP/neurolysin fold group have been crystallized in the closed form, however [51, 52]. In all cases, the closed form has been seen only when the enzyme is in complex with a bound ligand.

Based on the structure of the closed form of peptidyl dipeptidase (Dcp), I constructed a model of the closed form of TOP (Figure 6.3a). Using this model, the bound neurotensin and bradykinin substrates are brought into position with the carbonyl group of the known scissile bond roughly in position to coordinate the zinc ion and with the catalytic water within the range for nucleophilic attack (Figure 6.3b). Applying the same treatment to the dynorphin A(1-8), dynorphin B(1-9), and adrenorphin complexes shows that the peptides are not positioned for cleavage at the known scissile bond. There are two possible explanations for this observation. Either the enzyme has some variability in the closing hinge motion that is influenced by interactions of the peptide with domain II, or the bound peptide is able to shift registration in the closed form of the enzyme (Figure 6.4). In the absence of closed-form TOP-ligand structures, it is not possible to distinguish between the two models.

## Application of nano test tubes

I present here an efficient procedure for fabrication of nano test tubes that is potentially scalable for bulk manufacturing. A long range goal of this work is to encapsulate enzymes such as neuropeptidases in nano test tubes to demonstrate their potential utility as delivery devices for medical and industrial applications. During the course of this work we attempted multiple strategies for the immobilization of enzymes inside nano test tubes, but without success. It seems possible that some of the original polymer material used as a template in making the nano tubes is contaminating the inner tube surface, preventing access in attempts to derivatize that surface. The contamination was apparently not fully cleaned away despite oxidative plasma cleaning, exposure to high temperatures, or exposure to organic solvents - all of which were tried alone or in combination. Future attempts at enzyme immobilization inside nano test tubes should focus on using different polymers or solvents for non-destructive replication of AAO templates or on different metals other than gold that might bond less tightly to polymer during coating. It might be possible to shake off empty test tube shells from nano pillars during sonication if the strength of the polymer / metal interaction were reduced.

In other future applications of nano test tubes, the polymer core might actually be used to advantage. The idea would be to permeate therapeutic compounds into the polymer and then use the test tubes as timed-release delivery devices. Many otherwise promising drug leads suffer from water insolubility, so nano test tubes could be used as a means of “nanosuspension” of otherwise insoluble drugs [149, 150]. The time course of release might be controlled by adjusting the length and diameter of the nano tubes. Importantly, the outer test tube surface, which can be derivatized, could be used to attach targeting molecules such as antibodies, peptides, or DNA. It should be straightforward to include a therapeutic compound by simply dissolving the drug in the solvent used to wet the primary template. This should result in incorporation of the drug into the polymer matrix as the solvent evaporates from inside the pores of the primary template (Figure 6.5).

Although our goal of enzyme immobilization in nano test tubes was not realized the non-destructive method for template replication of nano test tubes we developed makes it possible to synthesize test tube shaped nanoparticles in yields up to one hundred fold larger than current methods. We report the use of non-destructive template replication to manufacture test tube shaped nanoparticles with diameters of 50-200 nm and lengths of 250 nm -1 μm without modification of the synthesis method. Shorter tubes only 125 nm in length could not be released, but this limit was not investigated in detail and it may be possible to produce tubes shorter than 250 nm long by simply using thinner metal coatings. The ability to vary the aspect ratio with this technique may have advantages when using the particles as therapeutics or in industrial processes. The vacuum deposition method of forming nano test tubes is versatile allowing the incorporation of a number of useful materials including magnetic metals.

## Conclusion

In conclusion, we have greatly improved our understanding of substrate recognition in neuropeptidases. By characterizing the unusual binding surfaces of a model neuropeptidase my work explains the mechanism for a key characteristic of this group, the ability to recognize a broad set of cleavage site sequences. This work also adds to our understanding of peptide recognition in general, and even bears upon the transient protein-protein interactions that underlie many cellular processes. Understanding the structural basis of TOP recognition also paves the way for future efforts to design specific inhibitors to this important family of enzymes. Finally, characterization of TOP’s binding surfaces now allows efforts toward rational retargeting of the enzyme to primarily metabolize specific bioactive peptides. Neuropeptidases reengineered to target particular peptides would be promising therapeutics for a variety of human disorders including heart disease and Alzheimer’s disease.

I have also developed a new method for synthesis of nano test tubes, which can be formed in a variety of sizes and compositions. We show that the particles retain most of the desirable qualities of previously synthesized nano test tubes and that yields are on the scale necessary for therapeutic delivery vehicles. The increased yields from our non-destructive replication method provide ample material for laboratory testing and provide natural avenues for scaling up for large scale production. More work is necessary to demonstrate the efficacy of these nano test tubes in delivery of biological molecules for industrial and therapeutic applications.

**Table 6.1 Binding mechanisms summary**

| Mechanisms of broad substrate recognition by TOP |
|---|
| Relatively flat binding surface rich in carbon allows Van der Waal's optimization |
| Ordered waters are displaced from surface |
| Hydrogen bonds formed mainly with substrate backbone |
| Shallow, multifunctional, grooves in surface accommodate side chains |
| Adaptive C-terminal recognition motif adds plasticity in border of binding site |

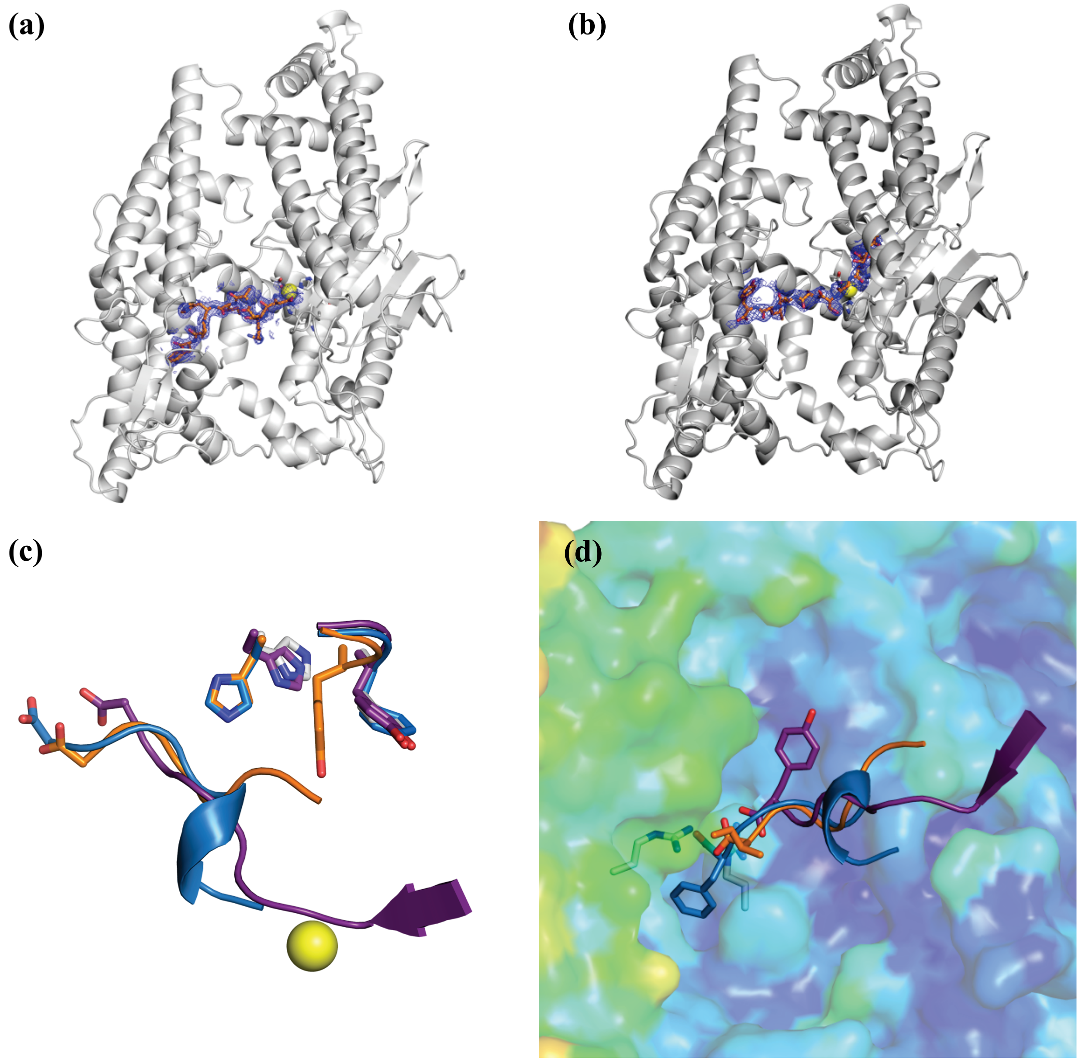

**Figure 6.1 Characteristics of non-productive binding.** Superposed complex structures of dynorphin A 1-8 (orange ribbon), angiotensin II (blue ribbon), and IgG4 (purple ribbon). **a)** Angiotenin II is shown as orange sticks with refined 2FoFc density displayed at 1σ while TOP is shown as gray ribbons **b)** IgG4 279-287 is shown as orange sticks with refined 2FoFc density displayed at 1σ while TOP is shown as gray ribbons **c)** His600, and Gly603-Tyr605 of TOP are shown in the background (color coded for their respective ligands) along with unliganded TOP (white) **d)** dynorphin A(1-8) (orange ribbon), angiotensin II (blue ribbon), and IgG4 (purple ribbon) with the C-terminal residue side chain shown. TOP is shown as a surface color coded by B factor (blue = lower, yellow = higher). Arg338 and Arg553 are shown as sticks.

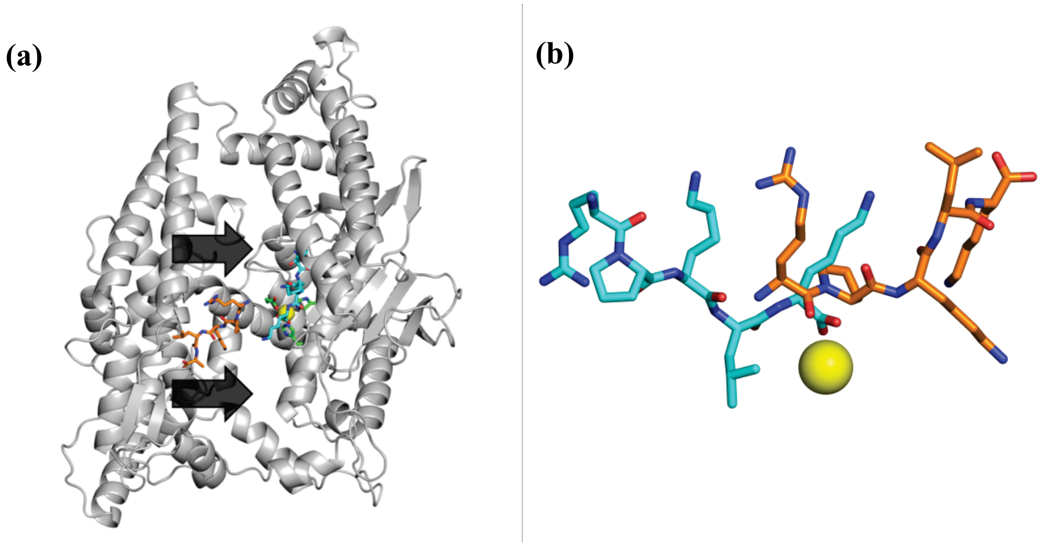

**Figure 6.2 Dynorphin A(9-13) closed model. a)** TOP is shown as gray ribbons. with the active site highlighted. The two fragments bound to either domain are shown as orange sticks (domain I) or blue sticks (domain II). Arrows indicate the rigid movement modeled by independent superposition of the two domains on closed DCP structure. **b)** Stick models of fragments after closed form modeling. Zn is shown as a yellow sphere.

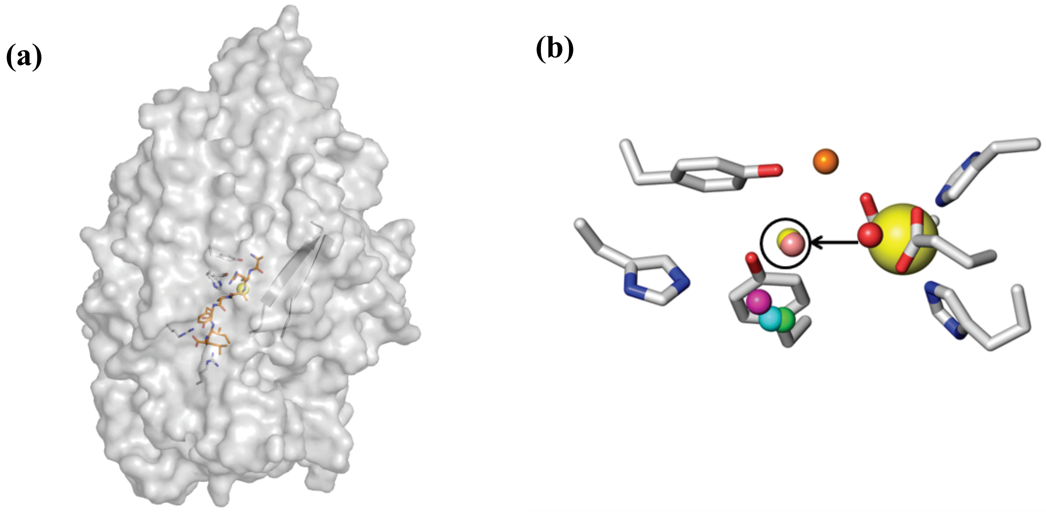

**Figure 6.3 Closed model of active site. a)** The two domains of each TOP substrate complex (domain I = residue #1-145, 350-543, 615-689 and domain II = residue #146-349, 544-614) were separated then superposed independently onto the closed DCP structure (1y79). The morph function in Chimera was then used to morph an open structure of unliganded TOP into the closed model. Neurotensin and other substrates were subsequently superposed into the closed model by alignment with domain I. **b)** Closeup of the active site geometry. The catalytic water (red) in the closed model is within range for nucleophilic attack on a given area (represented by an arrow and black circle). The coordinates of the alpha carbonyl of each known attacked carbon in the closed model are indicated by spheres (adrenorphin = dark pink, bradykinin = yellow, dynorphin A(1-8) = light blue, dynorphin A(1-13) = orange, dynorphin B(1-9) = green, neurotensin = light pink). TOP side chains involved in catalysis are shown as stick models including His600, Tyr605, Tyr612, His473, Glu474, His477, and Glu502.

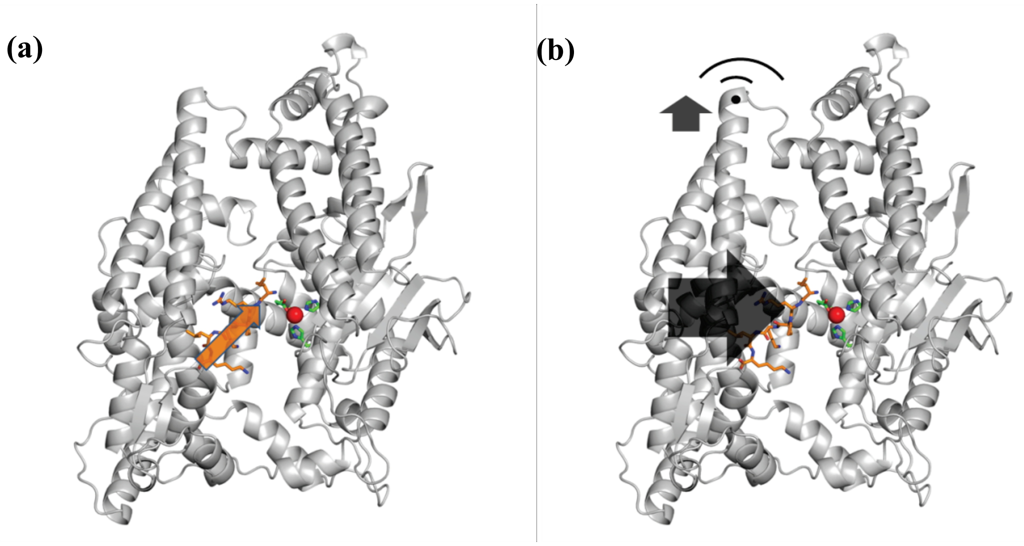

**Figure 6.4 Alternative models for substrates during hinge closure.** One of two models can be used to explain the registration of initial substrate binding. **a)** during hinge closure some substrates lift off and change registration in the binding site **b)** during hinge closure domain I shifts carrying the substrate with it in the current registration.

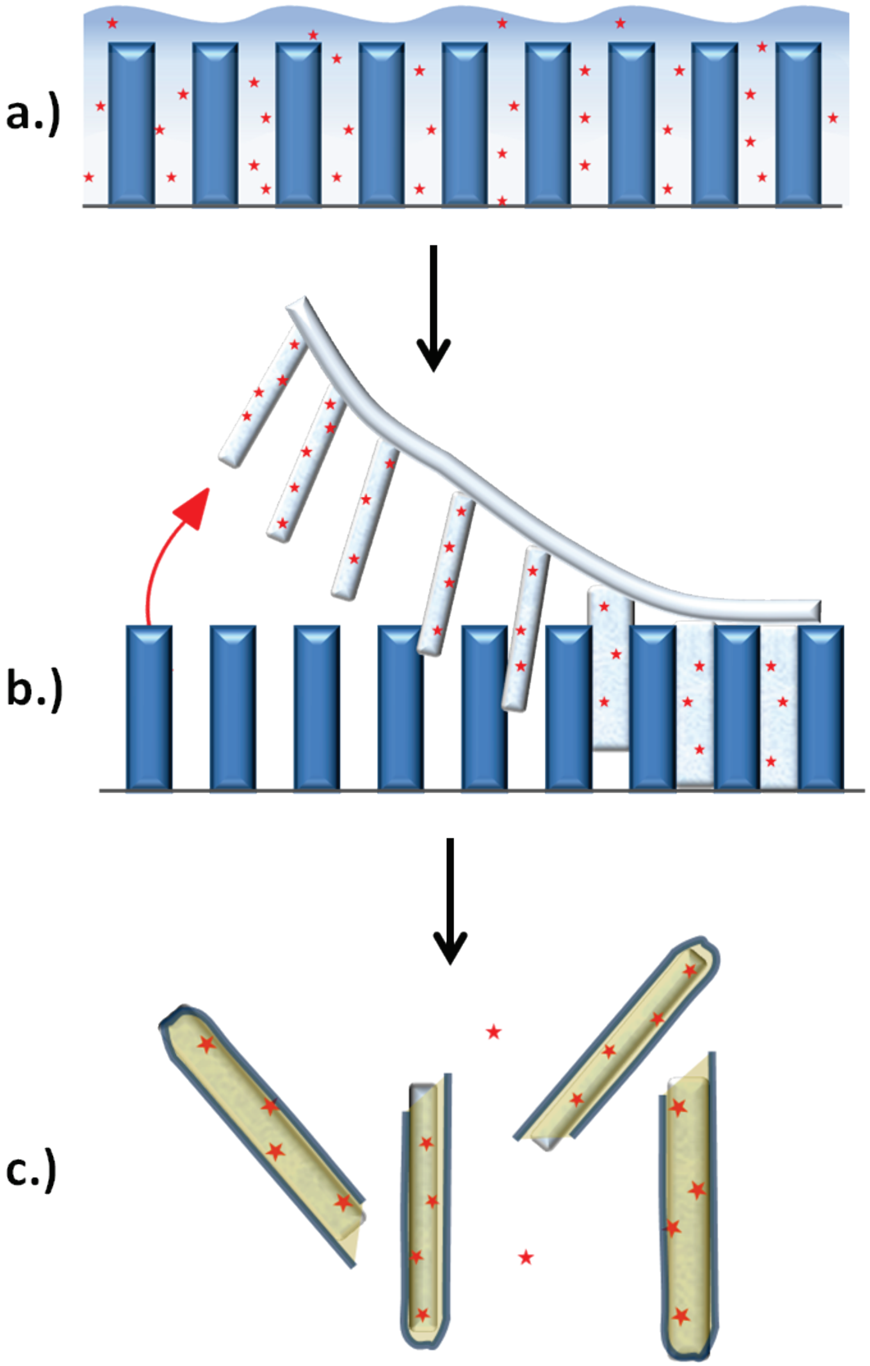

**Figure 6.5 Proposed incorporation of drug into nano test tubes. a)** dissolve the drug in solvent and apply to alumina template **b)** non-destructive replication as usual **c)** after coating and sonication the drug will be suspended in aqueous solution and trapped inside nano test tubes.

# BIBLIOGRAPHY

1. Shrimpton, C.N., A.I. Smith, and R.A. Lew, *Soluble metalloendopeptidases and neuroendocrine signaling.* Endocrine Reviews, 2002. **23**(5): p. 647-664.
2. Heise, T., et al., *Pharmacokinetics, pharmacodynamics and tolerability of multiple oral doses of linagliptin, a dipeptidyl peptidase-4 inhibitor in male type 2 diabetes patients.* Diabetes Obesity & Metabolism, 2009. **11**(8): p. 786-794.
3. Garg, R. and S. Yusuf, *OVERVIEW OF RANDOMIZED TRIALS OF ANGIOTENSIN-CONVERTING ENZYME-INHIBITORS ON MORTALITY AND MORBIDITY IN PATIENTS WITH HEART-FAILURE.* Jama-Journal of the American Medical Association, 1995. **273**(18): p. 1450-1456.
4. Pitt, B., et al., *The effect of spironolactone on morbidity and mortality in patients with severe heart failure.* New England Journal of Medicine, 1999. **341**(10): p. 709-717.
5. Yusuf, S., et al., *Effects of an angiotensin-converting-enzyme inhibitor, ramipril, on cardiovascular events in high-risk patients.* New England Journal of Medicine, 2000. **342**(3): p. 145-153.
6. Vincent, B., et al., *Contribution of endopeptidase 3.4.24.15 to central neurotensin inactivation.* European Journal of Pharmacology, 1997. **334**(1): p. 49-53.
7. Kest, B., M. Orlowski, and R.J. Bodnar, *INCREASES IN OPIOID-MEDIATED SWIM ANTINOCICEPTION FOLLOWING ENDOPEPTIDASE-24.15 INHIBITION.* Physiology & Behavior, 1991. **50**(4): p. 843-845.
8. Mentlein, R. and P. Dahms, *ENDOPEPTIDASE-24.16 AND ENDOPEPTIDASE-24.15 ARE RESPONSIBLE FOR THE DEGRADATION OF SOMATOSTATIN, NEUROTENSIN, AND OTHER NEUROPEPTIDES BY CULTIVATED RAT CORTICAL ASTROCYTES.* Journal of Neurochemistry, 1994. **62**(1): p. 27-36.
9. Molineaux, C.J. and J.M. Ayala, *AN INHIBITOR OF ENDOPEPTIDASE-24.15 BLOCKS THE DEGRADATION OF INTRAVENTRICULARLY ADMINISTERED DYNORPHINS.* Journal of Neurochemistry, 1990. **55**(2): p. 611-618.
10. Kim, S.I., et al., *Novel roles of neuropeptide processing enzymes: EC3.4.24.15 in the neurome.* Journal of Neuroscience Research, 2003. **74**(3): p. 456-467.
11. Genden, E.M. and C.J. Molineaux, *INHIBITION OF ENDOPEPTIDASE-24.15 DECREASES BLOOD-PRESSURE IN NORMOTENSIVE RATS.* Hypertension, 1991. **18**(3): p. 360-365.
12. Norman, M.U., et al., *Regulation of cardiovascular signaling by kinins and products of similar converting enzyme systems - Endopeptidases 3.4.24.15 and 24.16 in endothelial cells: potential role in vasoactive peptide metabolism.* American Journal of Physiology-Heart and Circulatory Physiology, 2003. **284**(6): p. H1978-H1984.
13. Smith, A.I., et al., *A novel stable inhibitor of endopeptidases EC 3.4.24.15 and 3.4.24.16 potentiates bradykinin-induced hypotension.* Hypertension, 2000. **35**(2): p. 626-630.
14. Kim, S.I., et al., *Regulation of cell-surface major histocompatibility complex class I expression by the endopeptidase EC3.4.24.15 (thimet oligopeptidase).* Biochem. J., 2003. **375**(Pt 1): p. 111-120.
15. Saric, T., et al., *Major histocompatibility complex class I-presented antigenic peptides are degraded in cytosolic extracts primarily by thimet oligopeptidase.* Journal of Biological Chemistry, 2001. **276**(39): p. 36474-36481.
16. Portaro, F.C.V., et al., *Thimet oligopeptidase and the stability of MHC class I epitopes in macrophage cytosol.* Biochemical and Biophysical Research Communications, 1999. **255**(3): p. 596-601.

17. Molineaux, C.J., et al., *ENDOPEPTIDASE-24.15 IS THE PRIMARY ENZYME THAT DEGRADES LUTEINIZING-HORMONE RELEASING HORMONE BOTH INVITRO AND INVIVO.* Journal of Neurochemistry, 1988. **51**(2): p. 624-633.
18. Paschoalin, T., et al., *Characterization of thimet oligopeptidase and neurolysin activities in B16F10-Nex2 tumor cells and their involvement in angiogenesis and tumor growth.* Molecular Cancer, 2007. **6**.
19. Yamin, R., et al., *Metalloendopeptidase EC 3.4.24.15 is necessary for Alzheimer's amyloid-beta peptide degradation.* Journal of Biological Chemistry, 1999. **274**(26): p. 18777-18784.
20. Jiracek, J., et al., *DEVELOPMENT OF HIGHLY POTENT AND SELECTIVE PHOSPHINIC PEPTIDE INHIBITORS OF ZINC ENDOPEPTIDASE-24-15 USING COMBINATORIAL CHEMISTRY.* Journal of Biological Chemistry, 1995. **270**(37): p. 21701-21706.
21. Wilkins, M.R., R.J. Unwin, and A.J. Kenny, *ENDOPEPTIDASE-24.11 AND ITS INHIBITORS - POTENTIAL THERAPEUTIC AGENTS FOR EDEMATOUS DISORDERS AND HYPERTENSION.* Kidney International, 1993. **43**(2): p. 273-285.
22. Vincent, B., et al., *PHOSPHORUS-CONTAINING PEPTIDES AS MIXED INHIBITORS OF ENDOPEPTIDASE-3.4.24.15 AND ENDOPEPTIDASE-3.4.24.16 - EFFECT ON NEUROTENSIN DEGRADATION IN-VITRO AND IN-VIVO.* British Journal of Pharmacology, 1995. **115**(6): p. 1053-1063.
23. Lim, E.J., et al., *Swapping the substrate specificities of the neuropeptidases neurolysin and thimet oligopeptidase.* Journal of Biological Chemistry, 2007. **282**(13): p. 9722-9732.
24. Checler, F., J.P. Vincent, and P. Kitabgi, *PURIFICATION AND CHARACTERIZATION OF A NOVEL NEUROTENSIN-DEGRADING PEPTIDASE FROM RAT-BRAIN SYNAPTIC-MEMBRANES.* Journal of Biological Chemistry, 1986. **261**(24): p. 1274-1281.
25. Dahms, P. and R. Mentlein, *PURIFICATION OF THE MAIN SOMATOSTATIN-DEGRADING PROTEASES FROM RAT AND PIG BRAINS, THEIR ACTION ON OTHER NEUROPEPTIDES, AND THEIR IDENTIFICATION AS ENDOPEPTIDASES 24.15 AND 24.16.* European Journal of Biochemistry, 1992. **208**(1): p. 145-154.
26. Norman, M.U., et al., *Regulation of cardiovascular signaling by kinins and products of similar converting enzyme systems - Metalloendopeptidases EC 3.4.24.15/16 regulate bradykinin activity in the cerebral microvasculature.* American Journal of Physiology-Heart and Circulatory Physiology, 2003. **284**(6): p. H1942-H1948.
27. Cleverly, K. and T.J. Wu, *Is the metalloendopeptidase EC 3.4.24.15 (EP24.15), the enzyme that cleaves luteinizing hormone-releasing hormone (LHRH), an activating enzyme?* Reproduction, 2010. **139**(2): p. 319-330.
28. Lasdun, A., et al., *INHIBITION OF ENDOPEPTIDASE 24.15 SLOWS THE INVIVO DEGRADATION OF LUTEINIZING-HORMONE-RELEASING HORMONE.* Journal of Pharmacology and Experimental Therapeutics, 1989. **251**(2): p. 439-447.
29. Lew, R.A., et al., *EVIDENCE FOR A 2-STEP MECHANISM OF GONADOTROPIN-RELEASING-HORMONE METABOLISM BY PROLYL ENDOPEPTIDASE AND METALLOENDOPEPTIDASE EC-3.4.24.15 IN OVINE HYPOTHALAMIC EXTRACTS.* Journal of Biological Chemistry, 1994. **269**(17): p. 12626-12632.
30. Acker, G.R., C. Molineaux, and M. Orlowski, *SYNAPTOSOMAL MEMBRANE-BOUND FORM OF ENDOPEPTIDASE-24.15 GENERATES LEU-ENKEPHALIN FROM DYNORPHIN1-8, ALPHA-NEUENDORPHIN-BETA-NEOENDORPHIN, AND MET-ENKEPHALIN FROM MET-ENKEPHALIN-ARG6-GLY7-LEU8.* Journal of Neurochemistry, 1987. **48**(1): p. 284-292.
31. Jiracek, J., et al., *Development of the first potent and selective inhibitor of the zinc endopeptidase neurolysin using a systematic approach based on combinatorial*

*chemistry of phosphinic peptides.* Journal of Biological Chemistry, 1996. **271**(32): p. 19606-19611.

32. Shrimpton, C.N. and A.I. Smith, *Soluble neutral metallopeptidases: Physiological regulators of peptide action.* Journal of Peptide Science, 2000. **6**(6): p. 251-263.
33. Stadler, M., et al., *Novel analgesic triglycerides from cultures of Agaricus macrosporus and other basidiomycetes as selective inhibitors of neurolysin.* Journal of Antibiotics, 2005. **58**(12): p. 775-786.
34. Orlowski, M., *THE MULTICATALYTIC PROTEINASE COMPLEX, A MAJOR EXTRALYSOSOMAL PROTEOLYTIC SYSTEM.* Biochemistry, 1990. **29**(45): p. 10289-10297.
35. Rock, K.L., et al., *INHIBITORS OF THE PROTEASOME BLOCK THE DEGRADATION OF MOST CELL-PROTEINS AND THE GENERATION OF PEPTIDES PRESENTED ON MHC CLASS-I MOLECULES.* Cell, 1994. **78**(5): p. 761-771.
36. Batalia, M.A. and E.J. Collins, *Peptide binding by class I and class II MHC molecules.* Biopolymers, 1997. **43**(4): p. 281-302.
37. Zhang, W.G., et al., *CRYSTAL-STRUCTURE OF THE MAJOR HISTOCOMPATIBILITY COMPLEX CLASS-I H-2K(B) MOLECULE CONTAINING A SINGLE VIRAL PEPTIDE - IMPLICATIONS FOR PEPTIDE BINDING AND T-CELL RECEPTOR RECOGNITION.* Proceedings of the National Academy of Sciences of the United States of America, 1992. **89**(17): p. 8403-8407.
38. Matsumura, M., et al., *EMERGING PRINCIPLES FOR THE RECOGNITION OF PEPTIDE ANTIGENS BY MHC CLASS-I MOLECULES.* Science, 1992. **257**(5072): p. 927-934.
39. Madden, D.R., D.N. Garboczi, and D.C. Wiley, *THE ANTIGENIC IDENTITY OF PEPTIDE-MHC COMPLEXES - A COMPARISON OF THE CONFORMATIONS OF 5 VIRAL PEPTIDES PRESENTED BY HLA-A2.* Cell, 1993. **75**(4): p. 693-708.
40. Brown, J.H., et al., *3-DIMENSIONAL STRUCTURE OF THE HUMAN CLASS-II HISTOCOMPATIBILITY ANTIGEN HLA-DR1.* Nature, 1993. **364**(6432): p. 33-39.
41. Stanfield, R.L. and I.A. Wilson, *PROTEIN-PEPTIDE INTERACTIONS.* Current Opinion in Structural Biology, 1995. **5**(1): p. 103-113.
42. Rothbard, J.B. and M.L. Gefter, *INTERACTIONS BETWEEN IMMUNOGENIC PEPTIDES AND MHC PROTEINS.* Annual Review of Immunology, 1991. **9**: p. 527-565.
43. Oliveira, V., et al., *Substrate specificity characterization of recombinant metallo oligo-peptidases thimet oligopeptidase and neurolysin.* Biochemistry, 2001. **40**(14): p. 4417-4425.
44. Knight, C.G., P.M. Dando, and A.J. Barrett, *THIMET OLIGOPEPTIDASE SPECIFICITY - EVIDENCE OF PREFERENTIAL CLEAVAGE NEAR THE C-TERMINUS AND PRODUCT INHIBITION FROM KINETIC-ANALYSIS OF PEPTIDE HYDROLYSIS.* Biochemical Journal, 1995. **308**: p. 145-150.
45. Oliveira, V., et al., *Temperature and salts effects on the peptidase activities of the recombinant metallooligopeptidases neurolysin and thimet oligopeptidase.* European Journal of Biochemistry, 2002. **269**(17): p. 4326-4334.
46. Hooper, N.M., *FAMILIES OF ZINC METALLOPROTEASES.* Febs Letters, 1994. **354**(1): p. 1-6.
47. Weaver, L.H., W.R. Kester, and B.W. Matthews, *CRYSTALLOGRAPHIC STUDY OF COMPLEX OF PHOSPHORAMIDON WITH THERMOLYSIN - MODEL FOR PRESUMED CATALYTIC TRANSITION-STATE AND FOR BINDING OF EXTENDED SUBSTRATES.* Journal of Molecular Biology, 1977. **114**(1): p. 119-132.
48. Matthews, B.W., et al., *3-DIMENSIONAL STRUCTURE OF THERMOLYSIN.* Nature-New Biology, 1972. **238**(80): p. 37-&.

49. Ray, K., et al., *Crystal structure of human thimet oligopeptidase provides insight into substrate recognition, regulation, and localization.* Journal of Biological Chemistry, 2004. **279**(19): p. 20480-20489.
50. Brown, C.K., et al., *Structure of neurolysin reveals a deep channel that limits substrate access.* Proceedings of the National Academy of Sciences of the United States of America, 2001. **98**(6): p. 3127-3132.
51. Comellas-Bigier, M., et al., *Crystal structure of the E-coli dipeptidyl carboxypeptidase Dcp: Further indication of a ligand-dependant hinge movement mechanism.* Journal of Molecular Biology, 2005. **349**(1): p. 99-112.
52. Towler, P., et al., *ACE2 X-ray structures reveal a large hinge-bending motion important for inhibitor binding and catalysis.* Journal of Biological Chemistry, 2004. **279**(17): p. 17996-18007.
53. Eng, C.M., et al., *Safety and efficacy of recombinant human alpha-galactosidase a replacement therapy in Fabry's disease.* New England Journal of Medicine, 2001. **345**(1): p. 9-16.
54. Leader, B., Q.J. Baca, and D.E. Golan, *Protein therapeutics: A summary and pharmacological classification.* Nature Reviews Drug Discovery, 2008. **7**(1): p. 21-39.
55. Trusheim, M., et al., *Characterizing markets for biopharmaceutical innovations : do biologics differ from small molecules?*2010, Cambridge, MA: National Bureau of Economic Research.
56. Barton, N.W., et al., *REPLACEMENT THERAPY FOR INHERITED ENZYME DEFICIENCY - MACROPHAGE-TARGETED GLUCOCEREBROSIDASE FOR GAUCHERS-DISEASE.* New England Journal of Medicine, 1991. **324**(21): p. 1464-1470.
57. Weinreb, N.J., et al., *Effectiveness of enzyme replacement therapy in 1028 patients with type 1 Gaucher disease after 2 to 5 years of treatment: A report from the Gaucher Registry.* American Journal of Medicine, 2002. **113**(2): p. 112-119.
58. Hirano, M., *Recombinant enzyme replacement therapy for infantile-onset Pompe disease.* Current Neurology and Neuroscience Reports, 2008. **8**(1): p. 45-47.
59. Burrow, T.A., et al., *Enzyme reconstitution/replacement therapy for lysosomal storage diseases.* Current Opinion in Pediatrics, 2007. **19**(6): p. 628-635.
60. Hansel, T.T., et al., *The safety and side effects of monoclonal antibodies.* Nature Reviews Drug Discovery, 2010. **9**(4): p. 325-338.
61. Liu, Y., et al., *Circulating neprilysin clears brain amyloid.* Molecular and Cellular Neuroscience, 2010. **45**(2): p. 101-107.
62. Liu, Y.X., et al., *Expression of Neprilysin in Skeletal Muscle Reduces Amyloid Burden in a Transgenic Mouse Model of Alzheimer Disease.* Molecular Therapy, 2009. **17**(8): p. 1381-1386.
63. Young, L.S., et al., *Viral gene therapy strategies: from basic science to clinical application.* Journal of Pathology, 2006. **208**(2): p. 299-318.
64. De Vocht, C., et al., *Assessment of stability, toxicity and immunogenicity of new polymeric nanoreactors for use in enzyme replacement therapy of MNGIE.* Journal of Controlled Release, 2009. **137**(3-4): p. 246-254.
65. Kim, J.B., J.W. Grate, and P. Wang, *Nanobiocatalysis and its potential applications.* Trends in Biotechnology, 2008. **26**(11): p. 639-646.
66. Klibanov, A.M., *Enzyme stabilization by immobilization.* Analytical Biochemistry, 1979. **93**: p. 1-25.
67. Kim, J., J.W. Grate, and P. Wang, *Nanostructures for enzyme stabilization.* Chemical Engineering Science, 2006. **61**(3): p. 1017-1026.

68. Walde, P. and S. Ichikawa, *Enzymes inside lipid vesicles: Preparation, reactivity and applications.* Biomolecular Engineering, 2001. **18**(4): p. 143-177.
69. Hashemifard, N., et al., *Fabrication and kinetic studies of a novel silver nanoparticles-glucose oxidase bioconjugate.* Analytica Chimica Acta, 2010. **675**(2): p. 181-184.
70. Aubin-Tam, M.E. and K. Hamad-Schifferli, *Structure and function of nanoparticle-protein conjugates.* Biomedical Materials, 2008. **3**(3): p. 17.
71. Herdt, A.R., B.S. Kim, and T.A. Taton, *Encapsulated magnetic nanoparticles as supports for proteins and recyclable biocatalysts.* Bioconjugate Chemistry, 2007. **18**(1): p. 183-189.
72. Huang, S.H., M.H. Liao, and D.H. Chen, *Direct binding and characterization of lipase onto magnetic nanoparticles.* Biotechnology Progress, 2003. **19**(3): p. 1095-1100.
73. Medintz, I.L., et al., *Quantum dot bioconjugates for imaging, labelling and sensing.* Nature Materials, 2005. **4**(6): p. 435-446.
74. Gupta, A.K. and M. Gupta, *Synthesis and surface engineering of iron oxide nanoparticles for biomedical applications.* Biomaterials, 2005. **26**(18): p. 3995-4021.
75. Hsu, J., et al., *Enhanced endothelial delivery and biochemical effects of alpha-galactosidase by ICAM-1-targeted nanocarriers for Fabry disease.* Journal of Controlled Release, 2011. **149**(3): p. 323-331.
76. Bale, S.S., et al., *Nanoparticle-Mediated Cytoplasmic Delivery of Proteins To Target Cellular Machinery.* Acs Nano, 2010. **4**(3): p. 1493-1500.
77. Muro, S., *New biotechnological and nanomedicine strategies for treatment of lysosomal storage disorders.* Wiley Interdisciplinary Reviews-Nanomedicine and Nanobiotechnology, 2010. **2**(2): p. 189-204.
78. Ranquin, A., et al., *Therapeutic nanoreactors: Combining chemistry and biology in a novel triblock copolymer drug delivery system.* Nano Letters, 2005. **5**(11): p. 2220-2224.
79. Huysmans, G., et al., *Encapsulation of therapeutic nucleoside hydrolase in functionalised nanocapsules.* Journal of Controlled Release, 2005. **102**(1): p. 171-179.
80. Geng, Y., et al., *Shape effects of filaments versus spherical particles in flow and drug delivery.* Nature Nanotechnology, 2007. **2**(4): p. 249-255.
81. Hillebrenner, H., et al., *Template synthesized nanotubes for biomedical delivery applications.* Nanomedicine, 2006. **1**(1): p. 39-50.
82. Moghimi, S.M., A.C. Hunter, and J.C. Murray, *Long-circulating and target-specific nanoparticles: Theory to practice.* Pharmacological Reviews, 2001. **53**(2): p. 283-318.
83. Perry, J.L., et al., *Fabrication of biodegradable nano test tubes by template synthesis.* Nanomedicine, 2010. **5**(8): p. 1151-1160.
84. Perry, J.L., C.R. Martin, and J.D. Stewart, *Drug-Delivery Strategies by Using Template-Synthesized Nanotubes.* Chemistry-a European Journal, 2011. **17**(23): p. 6296-6302.
85. Son, S.J., et al., *Magnetic nanotubes for magnetic-field-assisted bioseparation, biointeraction, and drug delivery.* Journal of the American Chemical Society, 2005. **127**(20): p. 7316-7317.
86. Masuda, H. and K. Fukuda, *ORDERED METAL NANOHOLE ARRAYS MADE BY A 2-STEP REPLICATION OF HONEYCOMB STRUCTURES OF ANODIC ALUMINA.* Science, 1995. **268**(5216): p. 1466-1468.
87. Gasparac, R., et al., *Template synthesis of nano test tubes.* Nano Letters, 2004. **4**(3): p. 513-516.
88. Grimm, S., et al., *Nondestructive replication of self-ordered nanoporous alumina membranes via cross-linked polyacrylate nanofiber arrays.* Nano Letters, 2008. **8**(7): p. 1954-1959.

89. Choi, M.K., et al., *Simple Fabrication of Asymmetric High-Aspect-Ratio Polymer Nanopillars by Reusable AAO Templates.* Langmuir, 2011. **27**(6): p. 2132-2137.
90. Oliveira, V., et al., *Selective Neurotensin-Derived Internally Quenched Fluorogenic Substrates for Neurolysin (EC 3.4.24.16): Comparison with Thimet Oligopeptidase (EC 3.4.24.15) and Neprilysin (EC 3.4.24.11).* Analytical Biochemistry, 2001. **292**(2): p. 257-265.
91. Peters, K. and F.M. Richards, *CHEMICAL CROSS-LINKING - REAGENTS AND PROBLEMS IN STUDIES OF MEMBRANE STRUCTURE.* Annual Review of Biochemistry, 1977. **46**: p. 523-551.
92. Quiocho, F.A. and F.M. Richards, *INTERMOLECULAR CROSS LINKING OF PROTEIN IN CRYSTALLINE STATE - CARBOXYPEPTIDASE-A.* Proceedings of the National Academy of Sciences of the United States of America, 1964. **52**(3): p. 833-&.
93. Rodgers, D.W., *Practical cryocrystallography.* Macromolecular Crystallography, Pt A, 1997. **276**: p. 183-203.
94. Otwinowski, Z. and W. Minor, *Processing of X-ray diffraction data collected in oscillation mode.* Macromolecular Crystallography, Pt A, 1997. **276**: p. 307-326.
95. McCoy, A.J., et al., *Likelihood-enhanced fast translation functions.* Acta Crystallographica Section D-Biological Crystallography, 2005. **61**: p. 458-464.
96. Storoni, L.C., A.J. McCoy, and R.J. Read, *Likelihood-enhanced fast rotation functions.* Acta Crystallographica Section D-Biological Crystallography, 2004. **60**: p. 432-438.
97. Adams, P.D., et al., *PHENIX: building new software for automated crystallographic structure determination.* Acta Crystallographica Section D-Biological Crystallography, 2002. **58**: p. 1948-1954.
98. Emsley, P. and K. Cowtan, *Coot: model-building tools for molecular graphics.* Acta Crystallographica Section D-Biological Crystallography, 2004. **60**: p. 2126-2132.
99. Wiseman, T., et al., *RAPID MEASUREMENT OF BINDING CONSTANTS AND HEATS OF BINDING USING A NEW TITRATION CALORIMETER.* Analytical Biochemistry, 1989. **179**(1): p. 131-137.
100. Freyer, M.W. and E.A. Lewis, *Isothermal titration calorimetry: Experimental design, data analysis, and probing Macromolecule/Ligand binding and kinetic interactions*, in *Biophysical Tools for Biologists: Vol 1 in Vitro Techniques*2008, Elsevier Academic Press Inc: San Diego. p. 79-113.
101. *ExPASy - ProtParam tool*. 2012; Available from: http://www.expasy.org/tools/protparam.html.
102. Sadasivan, V., et al., *Electrochemical self-assembly of porous alumina templates.* Aiche Journal, 2005. **51**(2): p. 649-655.
103. *Microplate Dimensions Guide*, in *www.gbo.com/bioscience*2007, Greiner.
104. Noinaj, N., *Structural Insights into the Substrate recognition and Catalytic Mechanism of Thimet Oligopeptidase and the Activation and Allosteric Regulation of Insulysin*, in *Molecular and Cellular Biochemistry*2008, University of Kentucky: Lexington. p. 183.
105. Rioli, V., et al., *Neuropeptide specificity and inhibition of recombinant isoforms of the endopeptidase 3.4.24.16 family: Comparison with the related recombinant endopeptidase 3.4.24.15.* Biochemical and Biophysical Research Communications, 1998. **250**(1): p. 5-11.
106. Rodd, D. and L.B. Hersh, *ENDOPEPTIDASE-24.16B - A NEW VARIANT OF ENDOPEPTIDASE-24.16.* Journal of Biological Chemistry, 1995. **270**(17): p. 10056-10061.

107. Lew, R.A., et al., *Evidence for a two-step mechanism of GnRH metabolism by prolyl endopeptidase and metalloendopeptidase EC 3.4.24.15.* Society for Neuroscience Abstracts, 1993. **19**(1-3): p. 1069.
108. Berti, D.A., et al., *Analysis of Intracellular Substrates and Products of Thimet Oligopeptidase in Human Embryonic Kidney 293 Cells.* Journal of Biological Chemistry, 2009. **284**(21): p. 14105-14116.
109. Rioli, V., et al., *Novel natural peptide substrates for endopeptidase 24.15, neurolysin, and angiotensin-converting enzyme.* Journal of Biological Chemistry, 2003. **278**(10): p. 8547-8555.
110. Camargo, A.C.M., et al., *Structural features that make oligopeptides susceptible substrates for hydrolysis by recombinant thimet oligopeptidase.* Biochemical Journal, 1997. **324**: p. 517-522.
111. Lew, R.A., et al., *SUBSTRATE-SPECIFICITY DIFFERENCES BETWEEN RECOMBINANT RAT TESTES ENDOPEPTIDASE EC-3.4.24.15 AND THE NATIVE BRAIN ENZYME.* Biochemical and Biophysical Research Communications, 1995. **209**(3): p. 788-795.
112. Reed, B., et al., *Dynorphin B biotransformation in the striatum of freely-moving rats: Microdialysis and mass spectrometry.* Society for Neuroscience Abstract Viewer and Itinerary Planner, 2003. **2003**: p. Abstract No. 645.17.
113. Kilpatrick, D.L., et al., *CHARACTERIZATION OF RIMORPHIN, A NEW LEU ENKEPHALIN-CONTAINING PEPTIDE FROM BOVINE POSTERIOR PITUITARY-GLANDS.* Life Sciences, 1982. **31**(16-1): p. 1849-1852.
114. Holland, D.R., et al., *STRUCTURAL COMPARISON SUGGESTS THAT THERMOLYSIN AND RELATED NEUTRAL PROTEASES UNDERGO HINGE-BENDING MOTION DURING CATALYSIS.* Biochemistry, 1992. **31**(46).
115. Bruce, L.A., et al., *Hydrogen bond residue positioning in the 599-611 loop of thimet oligopeptidase is required for substrate selection.* Febs Journal, 2008. **275**(22): p. 5607-5617.
116. Machado, M.F.M., et al., *The role of Tyr(605) and Ala(607) of thimet oligopeptidase and Tyr(606) and Gly(608) of neurolysin in substrate hydrolysis and inhibitor binding.* Biochemical Journal, 2007. **404**: p. 279-288.
117. Kawasaki, A., et al., *The Exquisite Structure and Reaction Mechanism of Bacterial Pz-peptidase A toward Collagenous Peptides X-RAY CRYSTALLOGRAPHIC STRUCTURE ANALYSIS OF PZ-PEPTIDASE A REVEALS DIFFERENCES FROM MAMMALIAN THIMET OLIGOPEPTIDASE.* Journal of Biological Chemistry. **285**(45): p. 34972-34980.
118. Schechter, I. and A. Berger, *On the size of the active site in proteases. I. Papain.* Biochem Biophys Res Commun, 1967. **27**(2): p. 157-62.
119. Hines, C.S., *Crystallographic and Functional Studies on the Neuropeptidase Neurolysin*, in *Biochemistry*2003, University of Kentucky: Lexington.
120. Rammensee, H.G., K. Falk, and O. Rotzschke, *PEPTIDES NATURALLY PRESENTED BY MHC CLASS-I MOLECULES.* Annual Review of Immunology, 1993. **11**: p. 213-244.
121. Carroll, M.J., et al., *Evidence for dynamics in proteins as a mechanism for ligand dissociation.* Nature Chemical Biology, 2012. **8**(3): p. 246-252.
122. Kato, A., et al., *CLONING, AMINO-ACID-SEQUENCE AND TISSUE DISTRIBUTION OF PORCINE THIMET OLIGOPEPTIDASE - A COMPARISON WITH SOLUBLE ANGIOTENSIN-BINDING PROTEIN.* European Journal of Biochemistry, 1994. **221**(1): p. 159-165.
123. McKie, N., et al., *THIMET OLIGOPEPTIDASE - SIMILARITY TO SOLUBLE ANGIOTENSIN II-BINDING PROTEIN AND SOME CORRECTIONS TO THE PUBLISHED AMINO-ACID-SEQUENCE OF THE RAT TESTIS ENZYME.* Biochemical Journal, 1993. **295**: p. 57-60.

124. Wangler, N.J., et al., *Identification of Membrane-bound Variant of Metalloendopeptidase Neurolysin (EC 3.4.24.16) as the Non-angiotensin Type 1 (Non-AT1), Non-AT(2) Angiotensin Binding Site.* Journal of Biological Chemistry, 2012. **287**(1): p. 114-122.
125. Orlowski, M., et al., *Endopeptidase 24.15 from rat testes. Isolation of the enzyme and its specificity toward synthetic and natural peptides, including enkephalin-containing peptides.* Biochem. J., 1989. **261**(3): p. 951-958.
126. Goldberg, R.N., N. Kishore, and R.M. Lennen, *Thermodynamic quantities for the ionization reactions of buffers.* Journal of Physical and Chemical Reference Data, 2002. **31**(2): p. 231-370.
127. Li, H., A.D. Robertson, and J.H. Jensen, *Very fast empirical prediction and rationalization of protein pK(a) values.* Proteins-Structure Function and Bioinformatics, 2005. **61**(4): p. 704-721.
128. Ladbury, J.E., *Application of isothermal titration calorirnetry in the biological sciences: Things are heating up!* Biotechniques, 2004. **37**(6): p. 885-887.
129. Vallee, B.L. and D.S. Auld, *ZINC - BIOLOGICAL FUNCTIONS AND COORDINATION MOTIFS.* Accounts of Chemical Research, 1993. **26**(10): p. 543-551.
130. Natesh, R., et al., *Crystal structure of the human angiotensin-converting enzyme-lisinopril complex.* Nature, 2003. **421**(6922): p. 551-554.
131. O'Sullivan, P.L., F.H. Baumann, and G.H. Gilmer, *Simulation of physical vapor deposition into trenches and vias: Validation and comparison with experiment.* Journal of Applied Physics, 2000. **88**(7): p. 4061-4068.
132. Dew, S., T. Smy, and M. Brett, *STEP COVERAGE, UNIFORMITY AND COMPOSITION STUDIES USING INTEGRATED VAPOR TRANSPORT AND FILM-DEPOSITION MODELS.* Japanese Journal of Applied Physics Part 1-Regular Papers Short Notes & Review Papers, 1994. **33**(2): p. 1140-1145.
133. Okuyama, T., et al., *Japan Elaprase (R) Treatment (JET) study: Idursulfase enzyme replacement therapy in adult patients with attenuated Hunter syndrome (Mucopolysaccharidosis II, MPS II).* Molecular Genetics and Metabolism, 2010. **99**(1): p. 18-25.
134. Murphy, C.J., et al., *Gold Nanoparticles in Biology: Beyond Toxicity to Cellular Imaging.* Accounts of Chemical Research, 2008. **41**(12): p. 1721-1730.
135. Hermanson, G., *Bioconjugate Techniques*1996: Academic Press.
136. Czapinska, H. and J. Otlewski, *Structural and energetic determinants of the S-1-site specificity in serine proteases.* European Journal of Biochemistry, 1999. **260**(3): p. 571-595.
137. Lovejoy, B., et al., *Crystal structures of MMP-1 and -13 reveal the structural basis for selectivity of collagenase inhibitors.* Nature Structural Biology, 1999. **6**(3): p. 217-221.
138. Perona, J.J. and C.S. Craik, *Evolutionary divergence of substrate specificity within the chymotrypsin-like serine protease fold.* Journal of Biological Chemistry, 1997. **272**(48): p. 29987-29990.
139. Gomis-Ruth, F.X., *Structure and Mechanism of Metallocarboxypeptidases.* Critical Reviews in Biochemistry and Molecular Biology, 2008. **43**(5): p. 319-345.
140. Ramagopal U.A, T.R., Meyer A.J., Freeman J., Bain K., Rodgers L., Sauder J.M., Burley S.K., Almo S.C., *Crystal structure of oligoendopeptidase-F from Enterococcus faecium.*, 2007.
141. Li, F., et al., *Structure of SARS coronavirus spike receptor-binding domain complexed with receptor.* Science, 2005. **309**(5742): p. 1864-1868.

142. Niemirowicz, G., et al., *The molecular analysis of Trypanosoma cruzi metallocarboxypeptidase 1 provides insight into fold and substrate specificity.* Molecular Microbiology, 2008. **70**(4): p. 853-866.

143. Saric, T., C.I. Graef, and A.L. Goldberg, *Pathway for degradation of peptides generated by proteasomes - A key role for thimet oligopeptidase and other metallopeptidases.* Journal of Biological Chemistry, 2004. **279**(45): p. 46723-46732.

144. Silva, C.L., et al., *Thimet oligopeptidase (EC 3.4.24.15), a novel protein on the route of MHC class I antigen presentation.* Biochemical and Biophysical Research Communications, 1999. **255**(3): p. 591-595.

145. Rock, K.L., I.A. York, and A.L. Goldberg, *Post-proteasomal antigen processing for major histocompatibility complex class I presentation.* Nature Immunology, 2004. **5**(7): p. 670-677.

146. Hagiwara, H., et al., *PURIFICATION AND CHARACTERIZATION OF ANGIOTENSIN-BINDING PROTEIN FROM PORCINE LIVER CYTOSOLIC FRACTION.* European Journal of Biochemistry, 1989. **185**(2): p. 405-410.

147. Pelmenschikov, V., M.R.A. Blomberg, and P.E. Siegbahn, *A theoretical study of the mechanism for peptide hydrolysis by thermolysin.* Journal of Biological Inorganic Chemistry, 2002. **7**(3): p. 284-298.

148. Machado, M.F.M., et al., *Catalytic properties of thimet oligopeptidase H600A mutant.* Biochemical and Biophysical Research Communications. **394**(2): p. 429-433.

149. Muller, R.H., C. Jacobs, and O. Kayser, *Nanosuspensions as particulate drug formulations in therapy Rationale for development and what we can expect for the future.* Advanced Drug Delivery Reviews, 2001. **47**(1): p. 3-19.

150. Stegemann, S., et al., *When poor solubility becomes an issue: From early stage to proof of concept.* European Journal of Pharmaceutical Sciences, 2007. **31**(5): p. 249-261.

# VITA

Jonathan Mark Wagner

DOB 05/08/1983

## EDUCATION

| | | |
|---|---|---|
| B.S.<br>Biochemistry | Southern Adventist University<br>Chemistry Department | 2002 - 2006 |

## PUBLICATIONS

in review:
Wagner, J.M., Jingyuan, Y., Rodgers, D.W, Hinds B.J. "Template synthesis of test tube nanoparticles using non-destructive replication"
in preparation:
Wagner, J.M., Noinaj, N., Rodgers, D.W. "An unusual mechanism for broad substrate recognition found in a peptidase."

## CONFERENCES / WORKSHOPS

| | | |
|---|---|---|
| "X-ray Methods in Structural Biology" | Cold Springs Harbor, NY | 2011 |
| American Society for Biochemistry and Molecular Biology (ASBMB) Annual Meeting | New Orleans, LA | 2009 |

## ORAL PRESENTATIONS

| | | |
|---|---|---|
| "Neuropeptidase substrate recognition and therapeutic enzyme delivery." | Department of Biochemistry Student Seminar | 2011 |
| "Substrate Recognition and Therapeutic Applications of Neuropeptidases." | Department of Biochemistry Spring Retreat | 2011 |

## POSTER PRESENTATIONS

| | | |
|---|---|---|
| "Basis for Substrate Recognition and Therapeutic Delivery of Neuropeptidases." | Biochemistry Department Spring Retreat | 06/2012 |
| "Encapsulation and Structure/Function of Thimet Oligopeptidase." | 38th Annual Naff Symposium | 05/2012 |
| "Substrate Recognition by Thimet Oligopeptidase" | 9th Annual SER-CAT Symposium | 03/2012 |
| "Substrate Recognition and Therapeutic Applications of Neuropeptidases." | Biochemistry Department Spring Retreat | 05/2011 |
| "Encapsulation and Structure/Function of Thimet Oligopeptidase" | NSF Research Experience for Undergraduates (REU) | 06/2010 |
| "Encapsulation and Structure/Function of Thimet Oligopeptidase" | Biochemistry Department Spring Retreat | 05/2010 |
| "Structure and Function of Thimet Oligopeptidase" | Biochemistry Department Spring Retreat | 05/2009 |
| "Structure and Function of Thimet Oligopeptidase" | American Society for Biochemistry and Molecular Biology (ASBMB) Annual Meeting | 04/2009 |

## AWARDS

| | | |
|---|---|---|
| NSF IGERT Fellowship | University of Kentucky | 2009-2011 |
| Daniel R. Reedy Award | University of Kentucky | 2007-2010 |
| STAR Scholarship | Southern Adventist University | 2003-2006 |
| Presidential Scholarship | Southern Adventist University | 2002 |